AN EXPERIMENTAL INVESTIGATION OF VERTICAL COAXIAL FLOWS OF DENSELY LOADED GAS-SOLID STREAMS

by

Yuming Shang

A dissertation submitted to the Graduate Faculty in Chemical Engineering in partial fulfillment of the requirements for the degree of Doctor of Philosophy, The City University of New York

2006

UMI Number: 3204997

UMI Microform 3204997

ProQuest Information and Learning Company
300 North Zeeb Road
P.O. Box 1346
Ann Arbor, MI 48106-1346

This manuscript has been read and accepted for the Graduate Faculty in Engineering in satisfaction of the dissertation requirement for the degree of Doctor of Philosophy.

_____	_____
Date	Professor Herbert Weinstein Chair of Examining Committee
_____	_____
Date	Dean Mumtaz K. Kassir Executive Officer

Professor Gabriel Tardos
Department Of Chemical Engineering, CCNY
_____

Professor Leslie L. Isaacs
Department Of Chemical Engineering, CCNY
_____

Professor Jae W. Lee
Department Of Chemical Engineering, CCNY
_____

Professor Yiannis Andreopoulus
Department Of Mechanical Engineering, CCNY
_____

Supervision Committee

THE CITY UNIVERSITY OF NEW YORK

Abstract

AN EXPERIMENTAL INVESTIGATION OF VERTICAL COAXIAL FLOWS OF DENSELY LOADED GAS-SOLID STREAMS

By

Yuming Shang

Adviser: Professor Herbert Weinstein

Circulating fluidized-bed catalytic reactor designs have become more complex over time in a continuous effort to improve yields and productivity. The next generation of designs may include staging the introduction of fresh catalyst for very fast multistep reactions. Such a staged catalyst design would most likely provide a zone in the reactor where coaxial streams of catalyst-laden gas merge and mix. This two-phase fluid dynamics problem has seen essentially no treatment in the literature.

Ducted coaxial flows of homogeneous gas streams exhibit interesting recirculation patterns when the inner-to-outer stream velocity ratio is either large enough or small enough. The existence of these recirculation patterns became evident during the development of ducted fan jet engines and other aerospace devices. It is very interesting to determine if similar reciculation patterns exist in ducted gas-catalyst two-phase coaxial flows. Significant recirculation patterns in such a reactor system would be detrimental to the design objectives by causing catalyst and gas backmixing and excessive catalyst holdup.

In this investigation, the City College Fast Fluidized Bed Facility was modified to provide ducted coaxial flow of gas-catalyst streams. Two catalyst streams from a single standpipe are separated and treated independently before merging into a single riser flow. Each of the separated streams can be controlled independently to some extent by controlling the acceleration gas to each stream. In this equipment, the inner-to-outer velocity ratio can be controlled in the range from 0.7 to 3.0.

There is no direct method to date to provide a visual observation of the gas-catalyst two-phase flow inside a high-density fluidized bed. Therefore, a

number of instrumental methods were used in these measurements to provide a picture of the flow structures of this ducted two-phase coaxial flow. The experimental results show consistently that recirculation patterns containing solids occur in these flows in a manner very similar to the patterns found in the homogeneous flows. The recirculation is above the mouth of the inner tube when the inner-to-outer velocity ratio is 0.7 and is against the wall at a higher elevation when the inner-to-outer velocity ratio is 3.

Acknowledgements

First of all, my sincerest thanks are addressed to my supervisor, Professor Herbert Weinstein for his invaluable support, encouragement and guidance throughout my research and write-up.

I gratefully acknowledge the support given by Mr. Zhenrong Xu and Mr. Andrew Eng, technical staff of Chemical Engineering Department at the City College of New York.

My PhD work would not have been possible without the support of my family, especially my wife.

TABLE OF CONTENTS

LIST OF TABLES

LIST OF FIGURES

I. INTRODUCTION

Circulating fluidized bed catalytic reactors are the heart of the fluid catalytic cracking process. Their designs have become more complex over time in a continuous effort to improve yields and productivity. Designs that essentially stage the introduction of fresh catalyst are now under consideration. Such a staged catalyst design would most likely provide a zone in the reactor where coaxial streams of catalyst laden gas merge and mix. This two-phase fluid dynamics problem has seen essentially no treatment in the literature.

The mixing of coaxial streams of single-phase miscible fluids has, however, received a great deal of attention in the literature. The most important example of such a flow in a commercial application is the ducted fan jet engine that powers essentially all commercial airplanes today. The complex recirculation patterns that have been observed for very large and very small velocity ratios of the coaxial streams can be attributed to Biot-Savart-like induction across the shear layer separating the streams.

It is very interesting to examine whether or not there is an equivalent induction across a shear layer wherein almost all of the momentum flux is in non-continuous particulate phases. This applies to the concept of vorticity in such a phase. However, there is no direct method to provide a visual observation or detailed local properties of the gas-solid two-phase flow inside a high-density fluidized bed. Indirect methods are employed in this work to determine if such recirculation patterns develop and, if so, to characterize the recirculation patterns developed in the initial mixing region of the coaxial flowing gas-solid streams in a riser flow.

For this investigation, a new entrance section was constructed in the City College Fast Fluidized Bed Facility to provide the coaxial gas-solid flow under various conditions, such as different outer to inner velocity ratio and solid circulating rate.

A set of measurements was carried out at selected elevations in the initial mixing region of the coaxial flow for different velocity ratio cases. The axial and radial pressure profiles were measured. Using an X-ray absorption technique, the solid fraction radial profiles before and after the coaxial streams merge were measured. The local solid flux across the riser diameter

at selected elevations were obtained with a traversing non-isokinetic sampling probe. Gas mixing behavior was studied using a gas tracing technique. Finally, measurements were also carried out for the coaxial mixing of flows with different temperatures to assess the interstream particle mixing.

The focus of this work is the characterization of the flow structures developed in the initial mixing region of coaxially flowing gas-solid two-phase streams with different velocity ratios and to determine if recirculation patterns can exist. Additionally, in the comparison of these data for coaxial flow with that of a typical riser flow, a better understanding of the whole flow structure and mixing behavior of any riser flow in the developing region is obtained. This understanding is very useful for improving riser reactor design and developing gas-solid two-phase flow models.

II. LITERATURE REVIEW

2.1 Single-phase Coaxial Flow

As a background for the gas-solid two-phase coaxial flow problem, a short review of single-phase or homogeneous coaxial flow is presented. This review illustrates the type of recirculation patterns that may also exist in two-phase, gas-solid systems.

The coaxial flow is usually divided into three regions: an initial region and the main downstream region with a transition region in between. In the initial mixing region of confined coaxial streams, because of the interaction of two streams in the confinement of the duct, very different flow structure (recirculation patterns) can form depending on the velocity ratio and the system geometry.

2.1.1 For High Inner to Outer Velocity Ratio Case ($\lambda=U_i/U_o>1$)

Earlier studies (Kuethe (1935) and Hinze et al. (1949)) of coaxial flow are mainly of unconfined coaxial flow with a high-velocity air jet issuing into a

lower velocity, surrounding air stream. The flow pattern was described as an iso-velocity potential core bounded by an annular mixing region. Acharya (1954) seems to be the first who studied the influence of velocity ratio on confined coaxial flowing jets. He pointed out that the velocity difference between the two streams has considerable influence on the momentum transfer and therefore the mixing process of the two streams. Becker et al. (1962) introduced the Craya-Curtet number, Ct, as a universal parameter for confined turbulent jet systems.

$$Ct = \frac{U_m}{[(U_1^2 - U_2^2)a^2 + 0.5(U_2^2 - U_m^2)]^{\frac{1}{2}}} \qquad (2.1.1)$$

Where $a=r_j/R$ is the radius ratio, $U_m=(U_1-U_2)a^2+U_2$ is the mean velocity in the mixing tube. They suggested that the appearance of recirculation is limited to Ct <0.85. Barchilon and Curtet (1964) made more detailed measurements of recirculation patterns by using a visualization method of the instantaneous flow patterns. Water-water jets were used for visualization purposes. Because of duct confinement and inadequate axial momentum flow in the co-flowing stream, the entrainment demands of the central jet

cannot be met at very high inner to outer velocity ratio (low Craya-Curtet number) and a recirculation eddy may develop, as shown in Figure 2.1.1.1.

Choi et al. (1986) studied coaxial air-air turbulent jets mixing in both constant and variable area ducts at velocity and area ratios where no recirculation patterns exist. Figure 2.1.1.2 is a mean velocity contour map for both cases. The wall boundary layer grows initially until it interacts and merges with the mixing layer. For the constant area mixing case, the flow near the confining wall is first decelerated locally before axial positions x/D =4.25, and then accelerated between x/D =4.25 and 11.0, as observed from the axial mean velocity profiles in Figure 2.1.1.3(a).

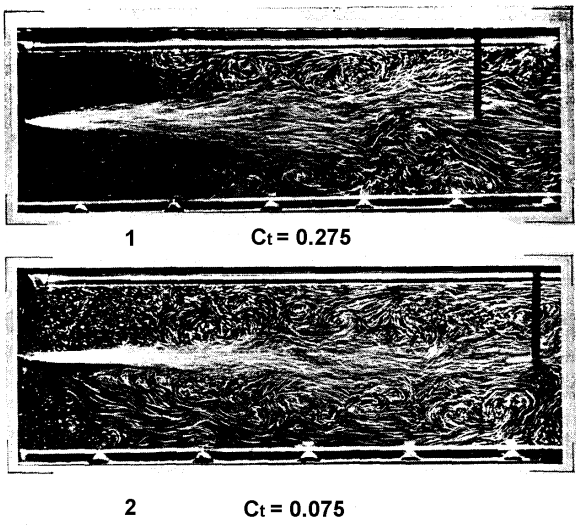

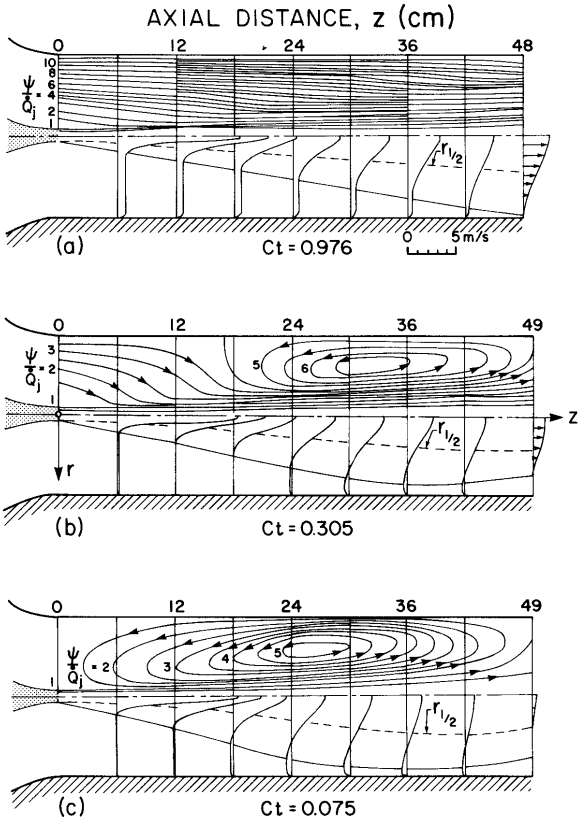

Figure 2.1.1.1 Experimentally Observed Streamline Pattern and Axial Velocity Profiles for Turbulent Mixing of Co-flowing Streams (Barchilon and Curtet 1964)

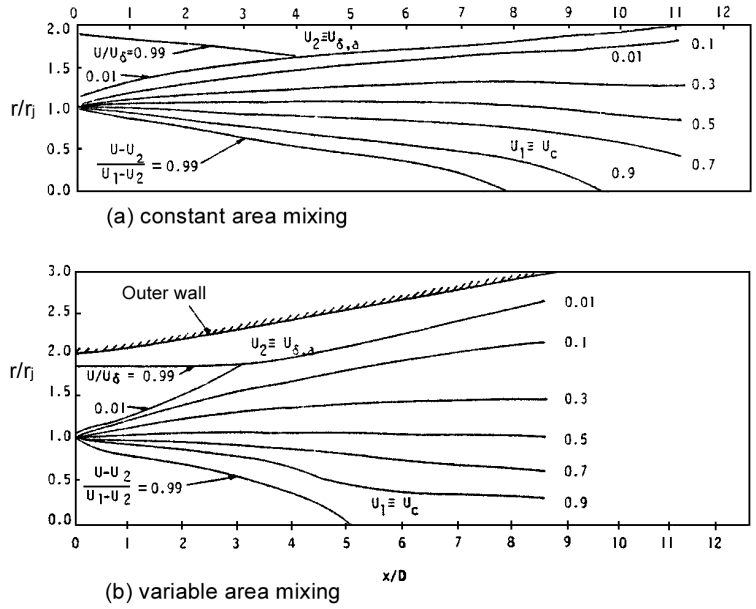

Figure 2.1.1.2 Axial Mean Velocity Contour Maps (Choi et al. 1986)

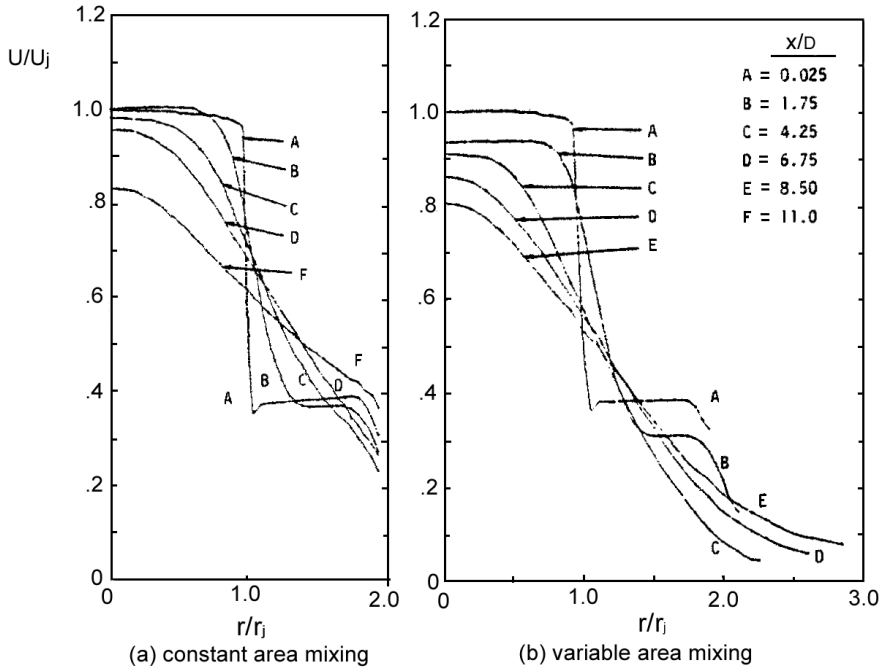

Figure 2.1.1.3 Axial Mean Velocity Profiles (Choi et al. 1986)

Khodadadi and Vlachos (1989) studied confined coaxial air-air turbulent jets with inlet conditions that result in flow separation followed by a recirculation cell (velocity of the central primary jet is much higher than that of the secondary jet), as shown in Figure 2.1.1.4. Two plexiglas mixing tubes were used with radius ratio (R/r_j) of 8.5 and 13, respectively. A laser Doppler anemometer was used to measure the axial mean velocities.

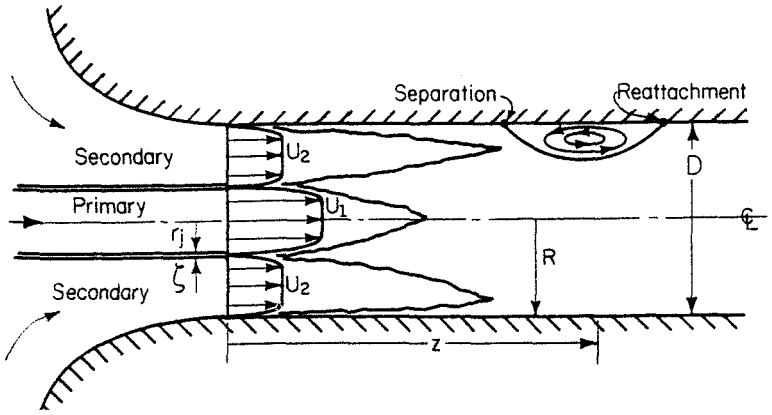

Figure 2.1.1.4 Confined Coaxial Turbulent Jet Flow (Khodadadi and Vlachos 1989)

2.1.2 For Low Inner to Outer Velocity Ratio Case ($\lambda=U_i/U_o<1$)

Zawacki and Weinstein (1968) and Johnson (1968) studied coaxial jets with faster moving outer stream. In this case, the wake behind the inner duct formed by the outer stream interacts with the issuing inner flow, flow reversal of the inner jet may occur at very low inner to outer velocity ratio. Shavit and Lavan (1973) investigated the mixing process in the initial region of confined air-air and air-argon coaxial laminar jets. Their experiment was conducted in coaxial tubes with diameter ratio of 0.25 and mixing length of 30 in, as shown in Figure 2.1.2.1. Hot-wire anemometry was used for velocity measurements. Concentration measurements were made with an aspirating probe. The maximum value of $R_{ej}(\rho_j/\rho_o)$ for which the flow remains laminar was found to be approximately 1060 for both air-air and air-argon cases. The laminar region of the air-argon system is shown in Figure 2.1.2.2. The laminar flow region for the homogeneous case was found much larger than that of the heterogeneous case. When the inner jet momentum is much smaller than the momentum of the outer jet, a recirculating cell may form, as shown in Figure 2.1.2.3. The cell grows upstream as velocity ratio increases, while its downstream end hardly moves.

Rozenman and Weinstein (1972) carried out measurements of this type of coaxial jet system for both air-air and air-Freon jets, but limited to the low-speed incompressible cases. They found that the potential core disappeared as the outer/inner velocity ratio (U_o/U_i) increased, and a backflow vortex may be formed at even higher outer/inner velocity ratios, as shown in Figure 2.1.2.4. In their particular apparatus, the potential core disappears at U_o/U_i of 3.5 for air/air jets and at 14 for a heavy Freon central jet case. A backflow region is formed at U_o/U_i of 13 for the air-air case and 26 for the heavy Freon-air case.

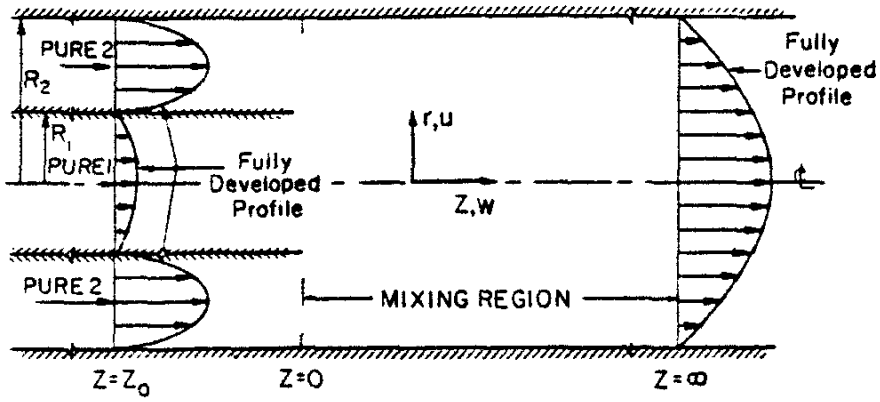

Figure 2.1.2.1 Confined Coaxial Laminar Jet Mixing (Shavit and Lavan 1973)

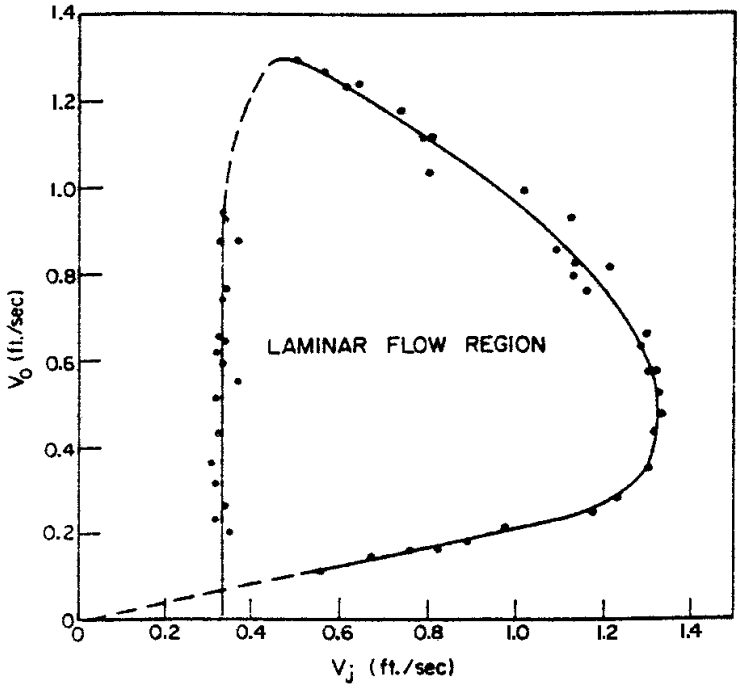

Figure 2.1.2.2 Laminar Region for Air-argon System (Shavit and Lavan 1973)

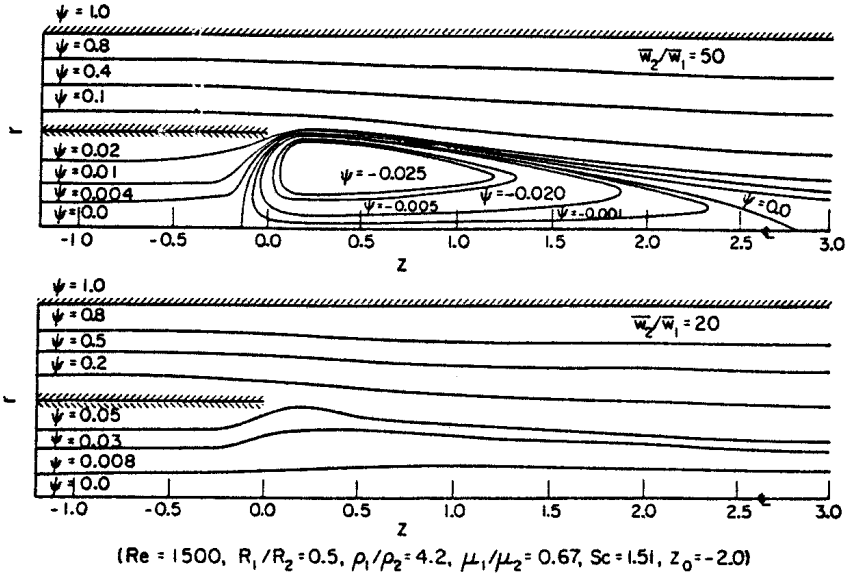

Figure 2.1.2.3 Streamline Contours, Variable Velocity (Shavit and Lavan 1973)

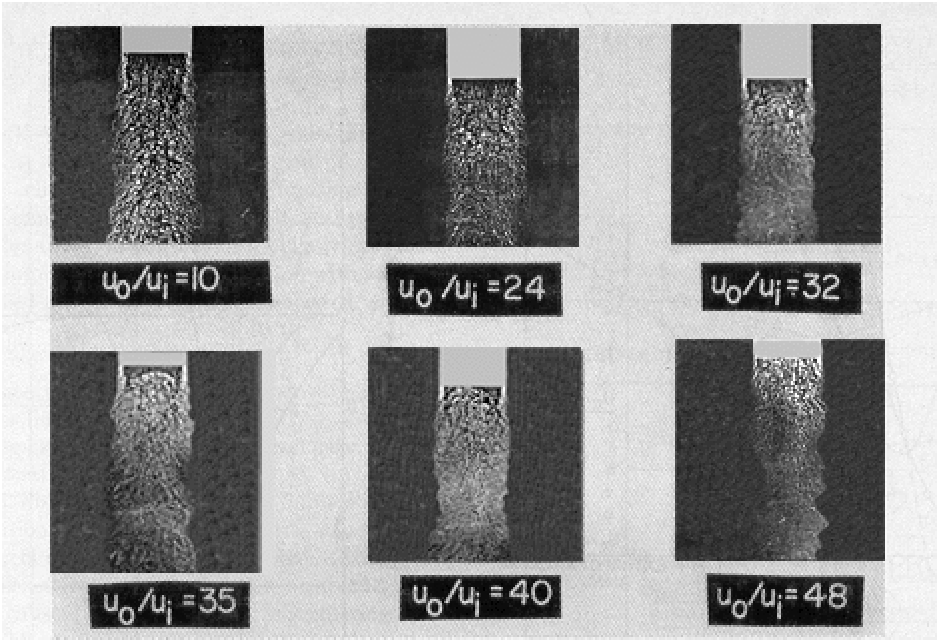

Figure 2.1.2.4 Initial Region of Freon Jet into Moving Airstream (Rozenman and Weinstein 1972)

2.2 Two-phase Coaxial Flow

Many chemical processes involve the mixing of gas and particulate phases, such as pulverized coal combustion, fluidized catalytic systems and power generators etc. Although many efforts have been made in characterizing the mixing behavior of single-phase coaxial flow, relatively little data of gas-solid coaxial flow is available in the literature.

Hedman and Smoot (1975) investigated the particle-gas dispersion effects with a particle-laden central primary jet and a gas only coaxial secondary jet, as shown in Figure 2.2.1. The diameters of primary(inner) and secondary(outer) jets are 2.54 cm and 12.7 cm, respectively. Gas and particle samples were taken with an isokinetic collection probe. They have shown that a logarithmic line is a good representation of the decay rate for extensive number of free and confined jets test.

$$\ln Y = A + B \ln (z/r_1) \qquad (2.2.1)$$

Where

Y is normalized mass flux, velocity,

or helium composition

A and B are correlative constants.

The influence of the 6- and 30-μm particles on the helium centerline decay is presented in Figure 2.2.2. In general, the effect of particles on the gas velocity and composition mixing rates is small, since there is only 20% by weight of particles in the primary stream, corresponding to a much less than 0.1% solid fraction. There are no solids in the secondary stream.

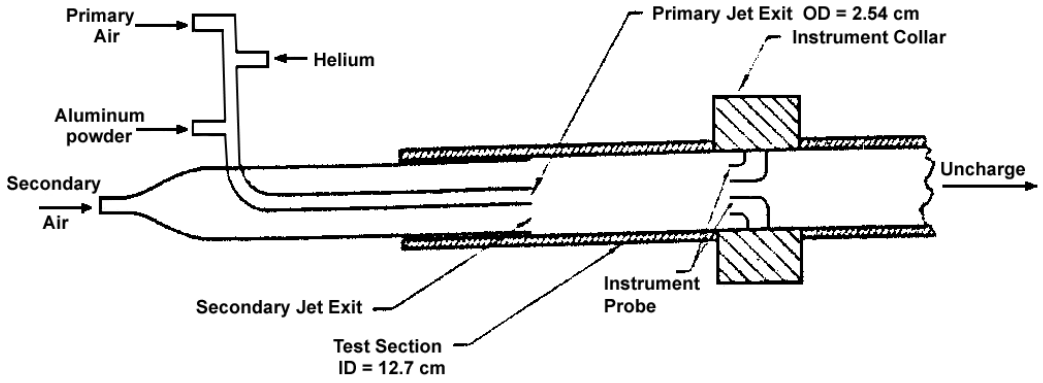

Figure 2.2.1 Schematic Diagram of Coaxial Jet Facility Test Section (Hedman and Smoot 1975)

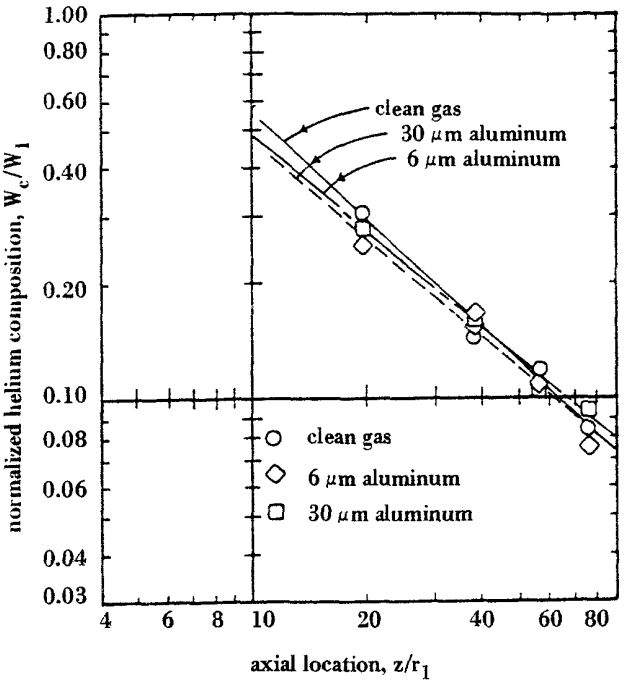

Figure 2.2.2 Effect of Powder on Helium Composition Centerline Decay (Hedman and Smoot 1975)

2.3 Theoretical Analysis and Models

Considerable effort has been expended to develop theoretical models for predicting the mixing behavior of single-phase coaxial flowing streams. Due to the complexity of the flow characteristics, almost all existing methods are based on some extent of assumptions and simplifications of the flow model and governing equations, and may be good only for special cases.

Craya and Curtet (1955) developed an "approximate confined jet theory" based on Reynolds and the continuity equations. Weinstein and Todd (1963) developed a solution of the mixing problem of unconfined laminar coaxial flow of different densities based on boundary-layer assumptions. Shavit and Lavan (1973) studied the laminar mixing of confined heterogeneous jets. The secondary jet is faster than the primary jet, and both have fully - developed velocity profiles as shown in Figure 2.1.2.1. The Navier-Stokes equations were solved numerically using vorticity, stream function, and concentration with variable properties. In their analyses it is assumed that there are no distributed sources of mass and energy, and no body forces; mixing is isothermal; and the mixture is ideal and incompressible. Razinsky and Brighton (1971, 1972) presented a theoretical model for turbulent

mixing with high-velocity primary stream, low velocity secondary stream, and nonseparating conditions. In their approach, the complete set of the equations of motion was simplified to axisymmetric boundary layer equations and integrated in the radial direction for a preselected form of velocity profile. The near similarity of the velocity profile is found in the initial region under their conditions. Their analytical forms of f(η) was also used to by Choi et al. (1986). Khodadadi and Vlachos (1989) also studied confined coaxial turbulent jets but with inlet conditions that result in flow separation. In their case, the SIMPLE procedure and the k-∈ turbulent model were used. The time-averaged governing equations were written as

$$\frac{\partial}{\partial z}(\rho U\phi)+\frac{1}{r}\frac{\partial}{\partial r}(\rho Vr\phi)=\frac{\partial}{\partial z}(\Gamma_\phi\frac{\partial\phi}{\partial z})+\frac{1}{r}\frac{\partial}{\partial r}(\Gamma_\phi r\frac{\partial\phi}{\partial r})+S^\phi \qquad (2.3.1)$$

Where U and V are time-averaged velocities in the axial and radial directions, respectively. ϕ represents various time-averaged quantities, such as mean velocities, etc. The transport equations and constants of the the k-∈ turbulent model are summarized in Table 2.3.1.

Table 2.3.1 Transport Equations and Turbulent Model Constants (Khodadadi and Vlachos 1989)

	ϕ	Γ_ϕ	S^ϕ
Continuity	1	0	0
Axial momentum	U	μ_{eff}	$\frac{\partial}{\partial z}\left(\mu_{eff}\frac{\partial U}{\partial z}\right)+\frac{1}{r}\frac{\partial}{\partial r}\left(r\mu_{eff}\frac{\partial V}{\partial z}\right)-\frac{\partial P}{\partial z}$
Radial momentum	V	μ_{eff}	$\frac{\partial}{\partial z}\left(\mu_{eff}\frac{\partial U}{\partial r}\right)+\frac{1}{r}\frac{\partial}{\partial r}\left(r\mu_{eff}\frac{\partial V}{\partial r}\right)-\frac{\partial P}{\partial r}-2\mu_{eff}\frac{V}{r^2}$
Kinetic energy	k	$\frac{\mu_{eff}}{\sigma_k}$	$G-\rho\epsilon$
Dissipation rate	ϵ	$\frac{\mu_{eff}}{\sigma_\epsilon}$	$\frac{\epsilon}{k}(C_1G-C_2\rho\epsilon)$

$$G=\mu_{eff}\left\{2\left[\left(\frac{\partial U}{\partial z}\right)^2+\left(\frac{\partial V}{\partial r}\right)^2+\left(\frac{V}{r}\right)^2\right]+\left(\frac{\partial U}{\partial r}+\frac{\partial V}{\partial z}\right)^2\right\}$$

$$\mu_{eff}=\mu+\mu_t,\qquad \mu_t=C_\mu\rho k^2/\epsilon$$

$$C_\mu=0.09,\quad C_1=1.44,\quad C_2=1.92,\quad \sigma_k=1.0,\quad \sigma_\epsilon=1.22$$

A nonunform grid was used with finer spacing in the regions of large spatial gradients, i.e., the initial mixing region in the tube. Using their model, the separation point is predicted well, but not the reattachment point. It is predicted to move further downstream than the experiment results show, Figure 2.3.1.

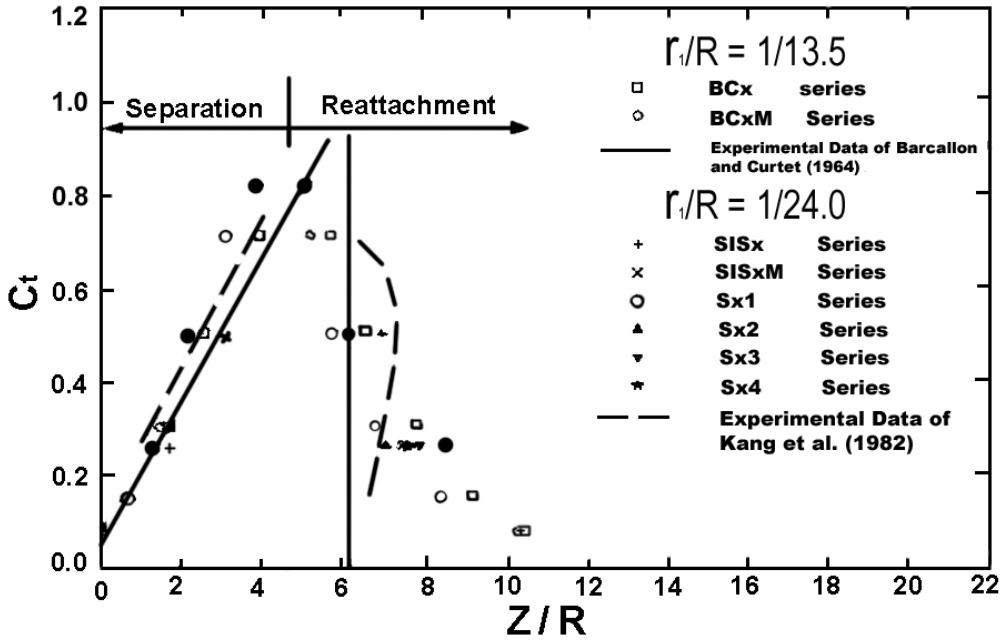

Figure 2.3.1 Locations of Separation and Reattachment Points (Khodadadi and Vlachos 1989)

Hedman and Smoot (1975) developed a numerical model for confined coaxial particle-laden jets as presented in Figure 2.2.1. Their major assumptions are summarized in Table 2.3.2. The simplified conservation equations are summarized in axisymmetric coordinates in Table 2.3.3. To solve these partial differential equations, the ideal gas law and several other auxiliary equations, which define the aerodynamic drag forces, and the eddy diffusivity of gas and powder phase, are also required. The configuration of this confined jet mixing model is shown in Figure 2.3.2. The comparison between the theoretical model and their experiment results is presented in

Figure 2.3.3. The predicted radial profiles are in relatively good agreement with the observed experiments. However, this model was examined only for very dilute gas-solid coaxial flow with particle-laden primary stream and a clean gas secondary stream.

Table 2.3.2 Coaxial Jet Model Assumptions (Hedman and Smoot 1975)

- ***Steady state, boundary layer assumptions valid.***
- ***Axisymmetric geometry, no wall boundary layer effects.***
- ***Nonreactive, two-component, ideal gas phase.***
- ***Constant pressure, molecular and thermal diffusion neglected.***
- ***Single, uniform, spherical particle base treated as continuous medium.***
- ***Particle volume negligible, no particle-particle interaction.***
- ***Gravity effects neglected.***
- ***Turbulent mixing of primary and secondary streams.***
- ***Thermal and dynamic nonequilibrium exists between particles and gas.***
- ***Smoot and Purcell (1967) gas-phase eddy viscosith model.***
- ***Stowell and Smoot (1973) gas-phasse turbulent mixing coefficient.***
- ***Longwell and Weiss (1953) particle-phase eddy viscosity relationship.***

Table 2.3.3 Summary of Partial Differential Equations (Hedman and Smoot 1975)

(a) Gas Phase Equations

Continuity: $$\partial(\rho u)/\partial z+(1/r)\partial(r\rho\upsilon)/\partial r=0 \quad (1)$$

z-motion: $$\rho u\partial u/\partial z+\rho\upsilon\partial u/\partial r=(1/r)\partial[(\mu r\partial u/\partial r)/\partial r]+F_{zk} \quad (2)$$

Primary gas specie: $$\rho u\partial W/\partial r+\rho\upsilon\partial W/\partial r=(1/r)\partial[(\mu r/Sc)\partial W/\partial r]/\partial r \quad (3)$$

Energy: $$\rho u\partial H/\partial z+\rho\upsilon\partial H/\partial r=(1/r)\partial[(\mu r/\mathrm{Pr})\partial H/\partial r]/\partial r+u_k F_{zk}+Q_k \quad (4)$$
$$+(1/r)(1-1/\mathrm{Pr})\partial[(\mu r\partial(u^2/2)/\partial r]/\partial r$$

(b) Particle Phase Equations

Continuity: $$\partial(\rho_k u_k)/\partial z+(1/r)\partial(r\rho_k u_k)/\partial r=(1/r)\partial[(r\mu_k/\rho_k)\partial\rho_k/\partial r]/\partial r \quad (5)$$

z-motion: $$\rho_k u_k\partial u_k/\partial z+\rho_k\upsilon_k\partial u_k/\partial r=(1/r)\partial(\mu_k r\partial u_k/\partial r)/\partial r-F_{zk} \quad (6)$$

r-motion: $$\rho_k u_k\partial\upsilon_k/\partial z+\rho_k\upsilon_k\partial\upsilon_k/\partial r=\partial[(\mu_k/r)\partial(r\upsilon_k)/\partial r]/\partial r-F_{rk} \quad (7)$$

Energy: $$\rho_k u_k\partial H_k/\partial z+\rho_k\upsilon_k\partial H_k/\partial r=(1/r)\partial(\mu_k r\partial H_k/\partial r)/\partial r-u_k F_{zk}-Q_k \quad (8)$$

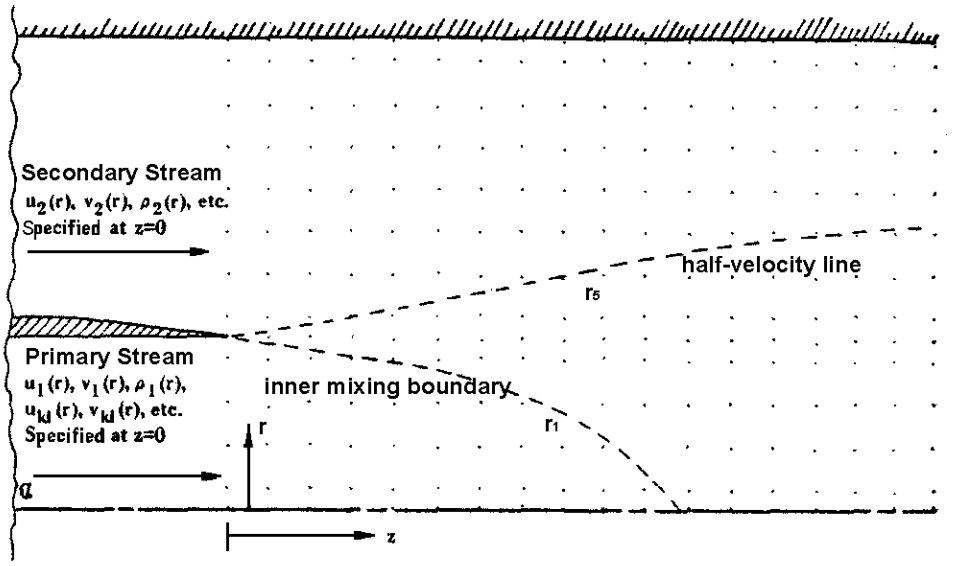

Figure 2.3.2 Configuration of Parallel Flow Confined Jet Mixing Model (Hedman and Smoot 1975)

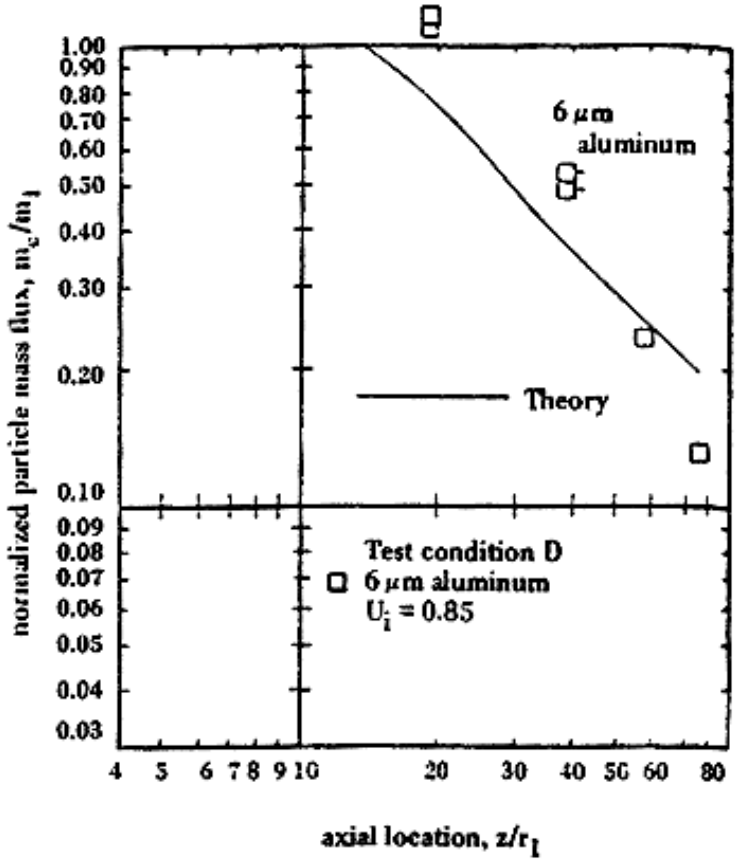

Figure 2.3.3 Comparison of Predicted Centerline Particle Mass Flux Decay with Experiment-test Conditions. (Hedman and Smoot 1975)

2.4 Flow Structure of Typical Riser Flow

2.4.1 Fluidization Regimes

Processes involving both a gas and solid phase are very common in industry. Heat/mass transfer and chemical reaction in such processes strongly depend on the interaction of the two phases within the reactor. Gas-solid two-phase

reactors are usually classified by several different gas-solid contacting regimes as shown in Figure 2.4.1.1.

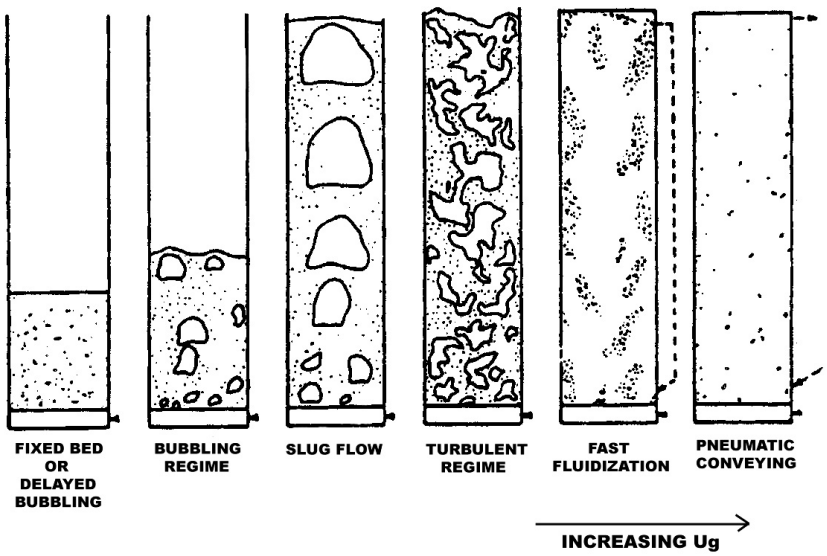

Figure 2.4.1.1 Different Contacting Regimes (Grace, 1986)

At relatively low gas velocity, processes are performed in packed, smooth fluidized or slugging beds (for small diameter riser) with limited carry-over. As gas velocity increases, entrainment becomes appreciable, and instead of bubbling, the heterogeneous two-phase character of the fluidized bed is replaced by a turbulent motion of solid clusters and voids of gas of various size and shapes. This is the so-called 'turbulent' fluidized bed regime. At even higher gas velocity, entrainment becomes so large that the bed can no

longer be maintained in the column. Fluidized beds in which solids are transported upward by a gas stream and then recycled to the bottom with an external recycling system are referred to as 'Circulating Fluidized Beds' (CFB). Most commercial CFB consists mainly of two parts: the riser, serving as the reactor, where particles are transported upwards, and the downcomer, serving as the recycle part of the loop, which conveys the particles back to the bottom of the riser. The CFB riser normally operates in the so-called 'fast fluidization' regime, situated between the dilute and dense pneumatic transport regimes.

2.4.2 Axial Solid Holdup in a Typical Riser

It is well accepted that fast fluidization riser flow is a flow regime where a denser phase transport region in the lower part coexists with a more dilute phase transport region in the upper part of the riser. This axial variation of solid holdup in the riser from dense to dilute was first studied by Li et al. (1980) and also observed by others (Weinstein, et al. (1983), Kato et al. (1989), Rhodes et al. (1989) etc.). As a result of the coexistence of the dense and dilute-phase transport regions, the fast beds often exhibit a characteristic 'S-shaped' axial profile of suspension density, as shown in Figure 2.4.2.1.

There is a transition region between the dense phase region at the bottom and the dilute phase region at the top of the riser.

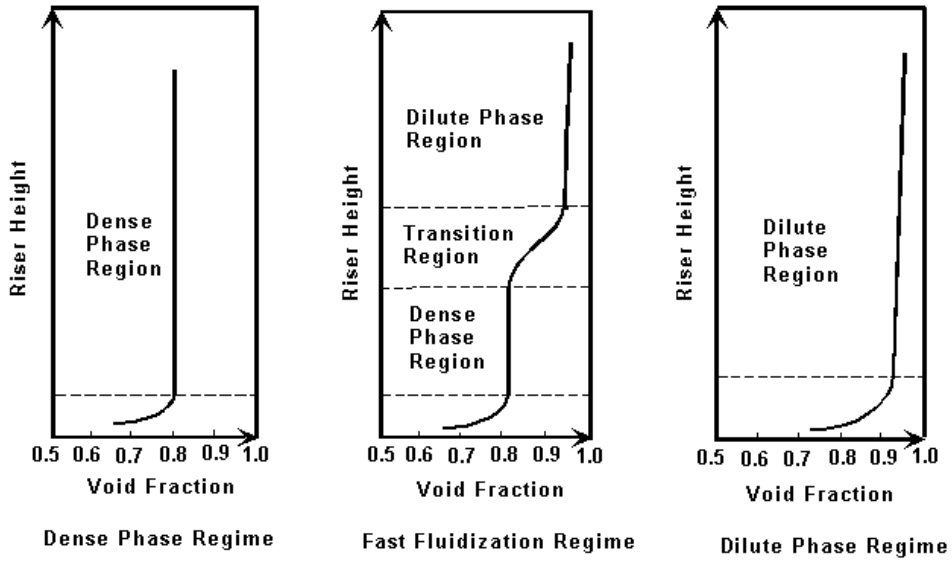

Figure 2.4.2.1 Axial Void Fraction Profiles for Different Regimes

The position of the transition region is dependent not only on the superficial gas velocity, but also on other operating conditions, such as the solid circulation rate, a key parameter in characterizing the gas-solid flow in riser. Weinstein et al. (1983) found that the transition region moves upward as the solid circulation rate increases for a given gas velocity. Since the pressure drop in the downcomer usually affects the pressure difference across the riser, the solids inventory level also has influence on the axial solid holdup profile in the riser. Increasing inventory imposes a greater pressure drop on the riser and thus moves the location of the transition region upward, as

shown in Figure 2.4.2.2. On the other hand, increasing the gas superficial velocity for a given solid circulation rate, the transition region moves downward and eventually disappears, leaving the entire bed in the dilute transport regime. The solid fraction is about 0.15 to 0.20 in the dense phase region and only about 0.04 or less in the dilute phase region, which is independent of the solid inventory level but dependent on solids circulation rate and gas velocity.

It should be mentioned that the apparent solid holdup, calculated from the pressure gradient measurements according to equation (2.4.2.1), is usually used to characterize a riser flow.

$$(1-\varepsilon_{apparent})\rho_s g = -\frac{dP}{dx} \qquad (2.4.2.1)$$

According to the one-dimensional momentum equation (2.4.2.2), the true solid fraction is equal to the apparent solid fraction only when the contributions of acceleration and wall friction are both negligible.

$$-\frac{dP}{dx} = \rho_s(1-\varepsilon_{true})g + \frac{d}{dx}\left[\rho_s(1-\varepsilon_{true})U_s^2 + \rho_g\varepsilon_{true}U_g^2\right] + \frac{dP_f}{dx} \qquad (2.4.2.2)$$

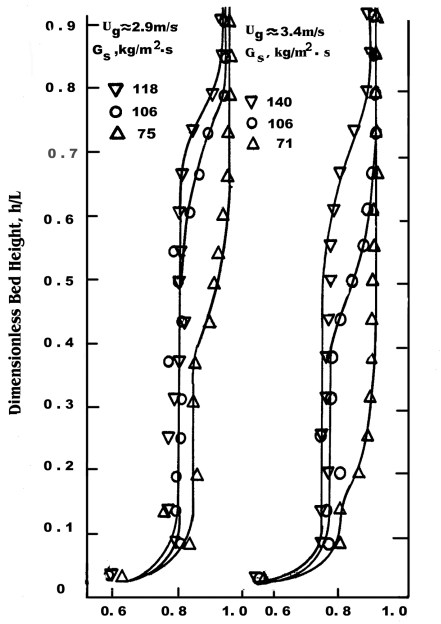

Void Faction, ε

A. For a Solids Inventory of 2.5m

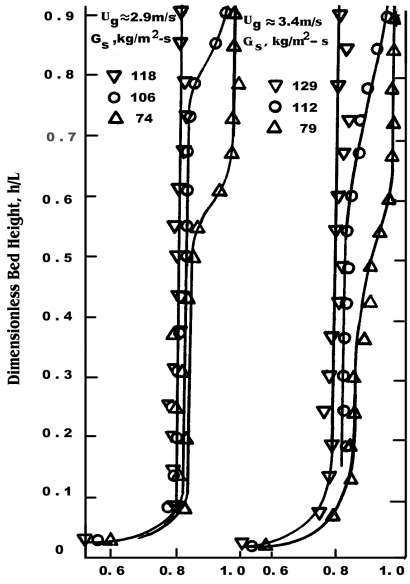

Void Fraction, ε

B. For a Solids Inventory of 4.1m

Figure 2.4.2.2 Axial Profiles of Void Fraction in CCNY Riser (Weinstein et al. 1983)

Kostazos (1997) found that the apparent solid holdup is usually in good agreement with the true solid holdup. Some results are shown in Figure 2.4.2.3. For a riser of this and larger diameters, the friction term is usually small and negligible compared to the others. The gas momentum term can be neglected since $\rho_g << \rho_s$. His explanation of this phenomenon is that the readjustment of the solid velocity and solid fraction profiles in a typical plug like riser flow gives

$$\frac{d}{dx}\int_0^R (1-\varepsilon_{true})U_s^2 r dr \approx 0$$

or

$$-\int_0^R U_s^2 \frac{d(1-\varepsilon_{true})}{dx} r dr \approx 2\int_0^R U_s (1-\varepsilon_{true})\frac{dU_s}{dx} r dr \qquad (2.4.2.3)$$

This equation indicates that as the result of flow readjustment in a typical riser flow, solid velocity increases strongly as solid fraction decreases strongly in the transition region and therefore the apparent solid fraction profile is about the same as the true solid fraction profile.

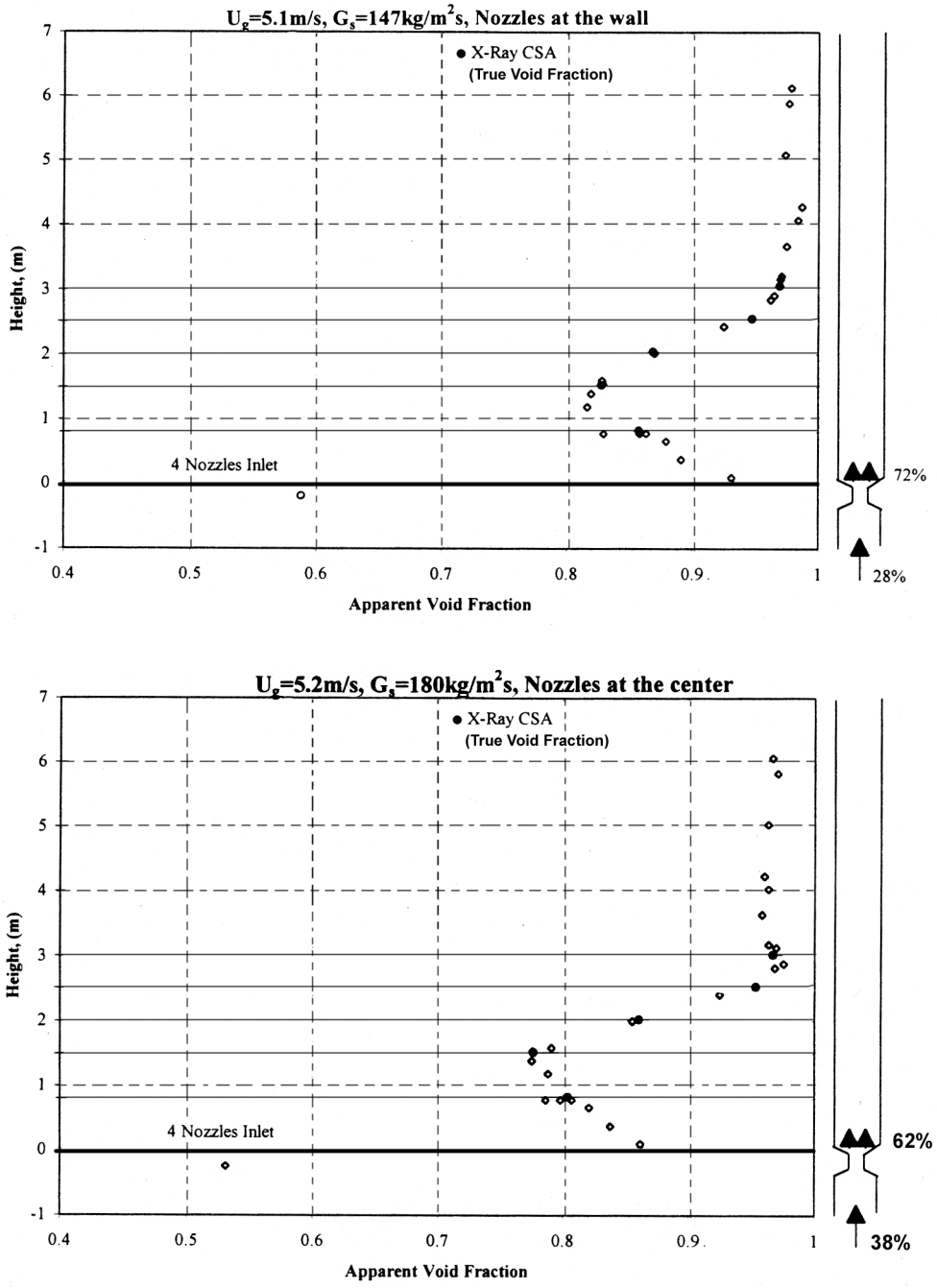

Figure 2.4.2.3 Apparent Void Fraction (Kostazos, 1997)

2.4.3 Radial Solid Fraction in a Typical Riser

Numerous investigations have been conducted to characterize the structure of the dilute-phase transport region at the top of a riser. It is generally agreed that this region has a core-annulus structure, characterized by a dilute rapidly rising core surrounded by a denser slowly-falling region adjacent to the riser wall. Li et al. (1980) measured the radial voidage for FCC catalyst in a riser using an optical fiber probe. Their results are shown in Figure 2.4.3.1. When gas velocity is less than the minimum velocity for fast fluidization (1.25m/s for that case), the radial voidage profile is relative flat; when gas velocity increases further, this profile becomes steeper; higher in center and lower near the wall. As gas velocity increases, pneumatic transport of solid takes place. The radial particle concentration in this case is flat and very dilute in the core while most of the particles aggregate in the vicinity of the wall. Feindt (1990) found a similar core-annulus flow structure in dilute phase riser flow, as shown in Figure 2.4.3.2. The radial solid fraction decreases with height, especially in the wall region.

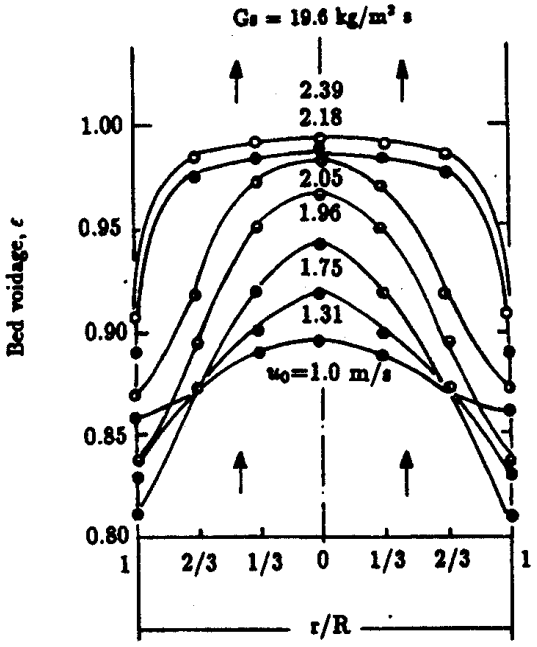

Figure 2.4.3.1 Radial Voidage for Fast Fluidized Beds (Li et al., 1985)

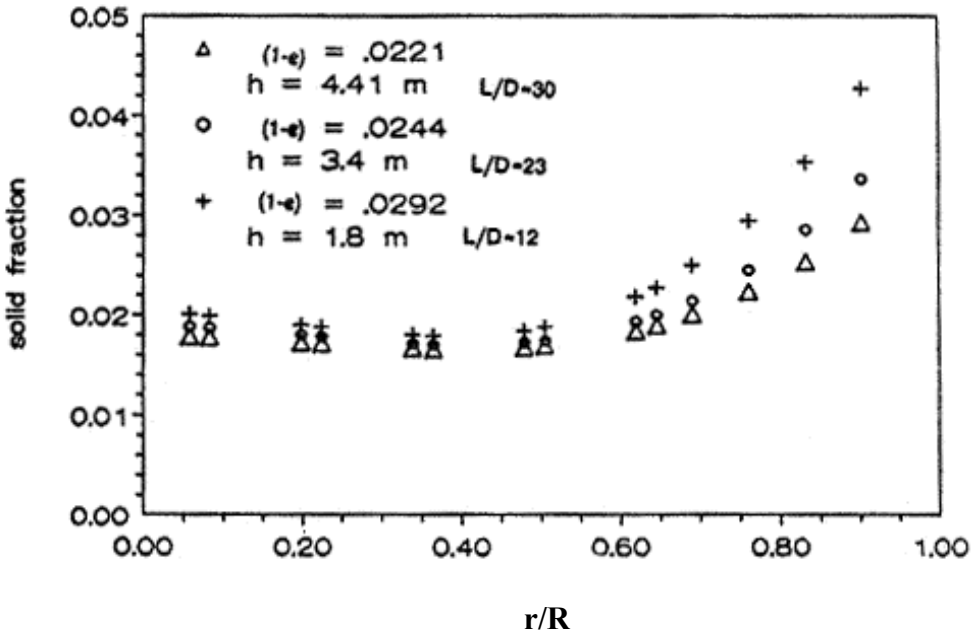

Figure 2.4.3.2 Radial Solid Density Profiles for Dilute Phase Riser Flow (Feindt, 1990)

The structure of the dense-phase transport region, on the other hand, is not as clear as the upper dilute region. Some researchers consider this region to be a turbulent bed (Brereton et al. 1993) while others treat it as a bubbling bed (Svensson et al. 1996). Due to differences in the dimensions and geometries of equipment employed by the different researchers, it is often difficult to compare the experimental results reported.

Using an X-ray absorption technique, Feindt (1990) measured the radial solid fraction profile of a 0.152m I.D. and 8.50m H. riser operating in dense phase. The core-annulus structure was also found in the dense phase region as shown in Figure 2.4.3.3. Unlike in the dilute phase, the radial density remains the same for the three different elevations.

Using capacitance tomography, Rhodes and Sollaart et al. (1998) conducted solid concentration measurements in a 0.09m I.D. and 7.2m H. riser at a solid circulation rate of 150kg/m^{2}s. The contours of constant solids volume fraction at different levels of the riser are presented in Figure 2.4.3.4. The results suggest that, under the axial pressure profile conditions typical of fast fluidization, the core-annulus flow persists over the whole length of the riser. In the core region, the suspension density is relatively low and the solids

flow is mainly in the upward direction. In the dense annulus region near the wall, the net flow of solids is predominantly downward in the upper dilute-phase region and upward in the lower dense-phase transport region. There is a transition region between the upper dilute-phase region and the lower dense-phase region, where the down-flowing solids in the annulus of the upper dilute-phase transport region meet the up-flowing particles in the annulus of the lower dense-phase transport region and where they undergo a redirection towards the core region of the riser.

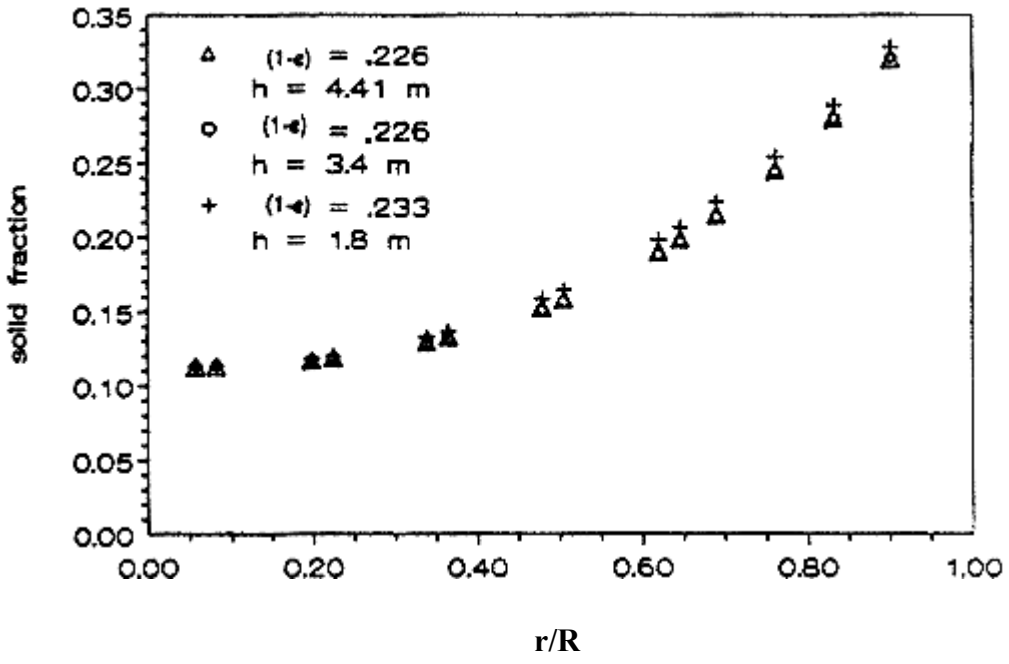

Figure 2.4.3.3 Radial Solid Density Profiles for Dense Phase Riser Flow (Feindt, 1990)

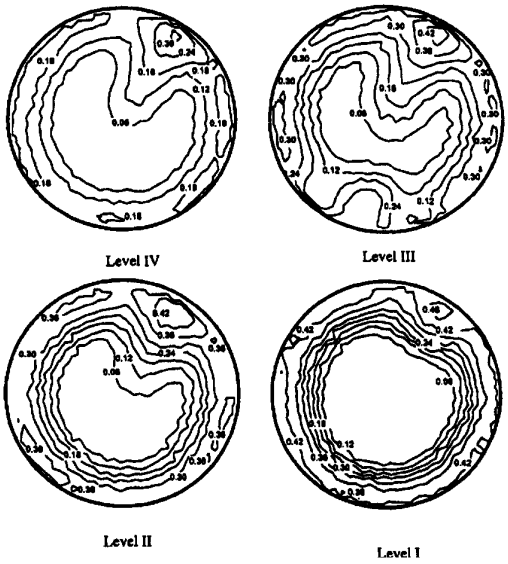

Figure 2.4.3.4 Contours of Solids Volume Fraction Measured by Tomographic Image at Different Levels of the Riser with Superficial Gas Velocity of 4m/s and Solids Circulation Rate of 150kg/m^{2}s (Rhodes et al. 1998)

2.4.4 Solid Flux in a Typical Riser

Solid flux influences heat transfer rates, particle residence time and thus reaction rates. The solid flux distribution is therefore very important part of the description of the solid flow behavior in CFBs. A simple suction probe is usually used to measure the time-averaged solid flux. Van Breugal et al. (1970) used an isokinetic sampling probe in the dense-phase region of riser and reported a parabolic solid flux profile. Monceaux et al. (1986) used non-isokinetic sampling to obtain local solid flux in the fully-developed region of

a 0.15m I.D. riser and found the existence of ‘similar’ solid flux profiles. Rhodes et al. (1992) and Herb et al. (1992) confirmed similar solid flux profiles and suggested using a non-isokinetic probe to measure the net solid flux.

Kostazos (1997) measured the net solid flux in a 15.2cm I.D., 8m H. riser with a non-isokinetic sampling probe using different aspirating velocities. As shown in Figure 2.4.4.1, the net solid flux is not affected significantly by the aspirating velocity. Especially in the near wall region, the net flux values are almost independent of the aspirating velocity. The solid flux profile has an almost parabolic shape with high flux at the riser axis and negative value close to the riser wall. The total solid circulation rates calculated from these data are very close to the independently measured circulation rate. Combining the solid flux profile with the solid fraction profile, the flow structure of a typical riser can be characterized as a core-annular flow with a rapidly upflowing dilute core surrounded by a slowly falling denser annular region adjacent to wall.

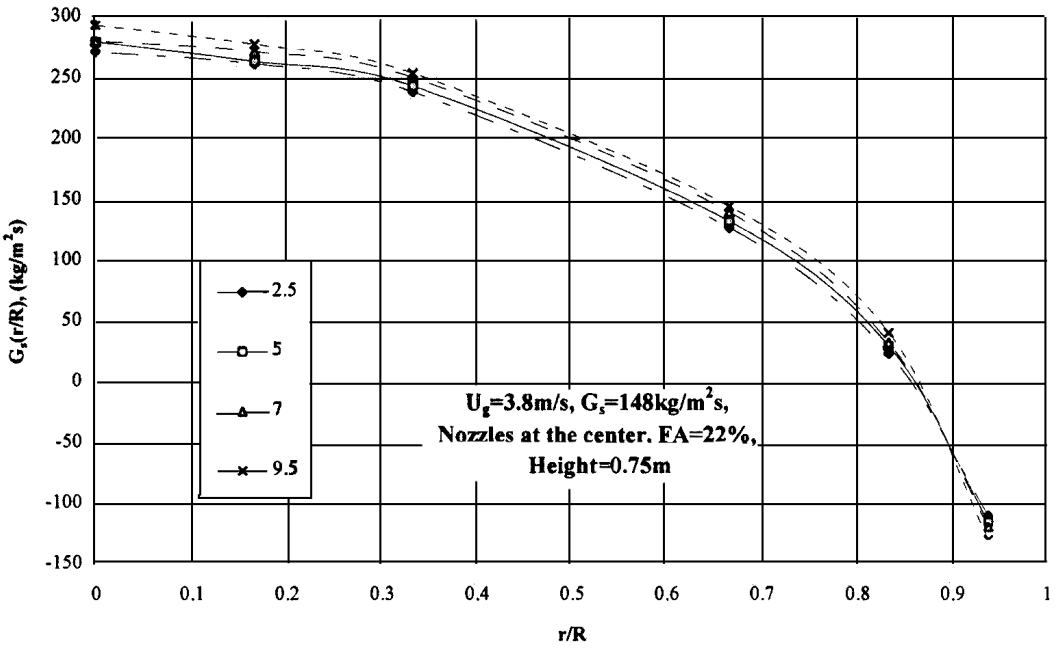

Figure 2.4.4.1 Radial Profile of the Axial Net Solid Flux as a Function of Aspirating Velocity (Kostazos 1997)

2.4.5 Influence of the Gas Velocity Profile

The inlet configuration of a riser has a significant effect on the gas velocity profile and therefore on the overall structure of the riser flow. Understanding the influence of gas velocity profile in a typical riser flow is very helpful in explaining the results of coaxial riser flow.

Kostazos (1997) studied the effect of the inlet gas velocity profile on the solid flux and the solid fraction profiles. Different inlet gas velocity profiles

were achieved by moving four inlet gas nozzles along radii of the riser, as shown in Figure 2.4.5.1. It can be observed in Figure 2.4.5.2 that the radial solid profile is strongly dependent on the inlet gas velocity profile. The radial solid profile is much flatter when the nozzles are located closer to the riser wall. There is, however, only a small effect of the inlet gas velocity profile on the radial solid flux profile, as observed in Figure 2.4.5.3. These results indicate that the solid velocity profile rearranges its shape corresponding to the solid fraction profile. Moving the nozzles to the wall increases the solid velocity as the solid fraction decreases in the annular region close to the wall. This kind of flow readjustment also happens in the transition region of a typical riser flow as mentioned above in section 2.4.2.

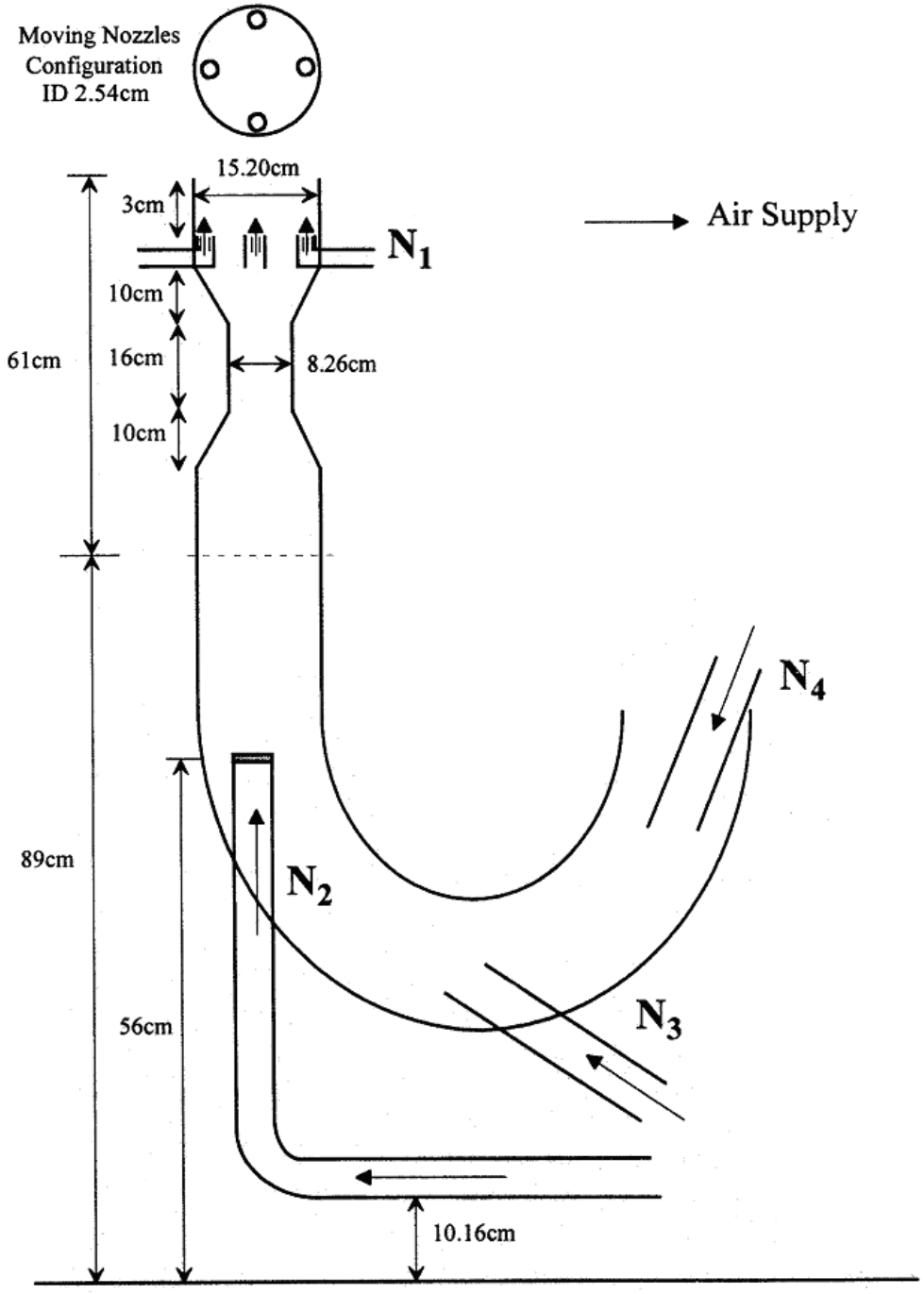

Figure 2.4.5.1 Inlet Nozzle Configuration (Kostazos 1997)

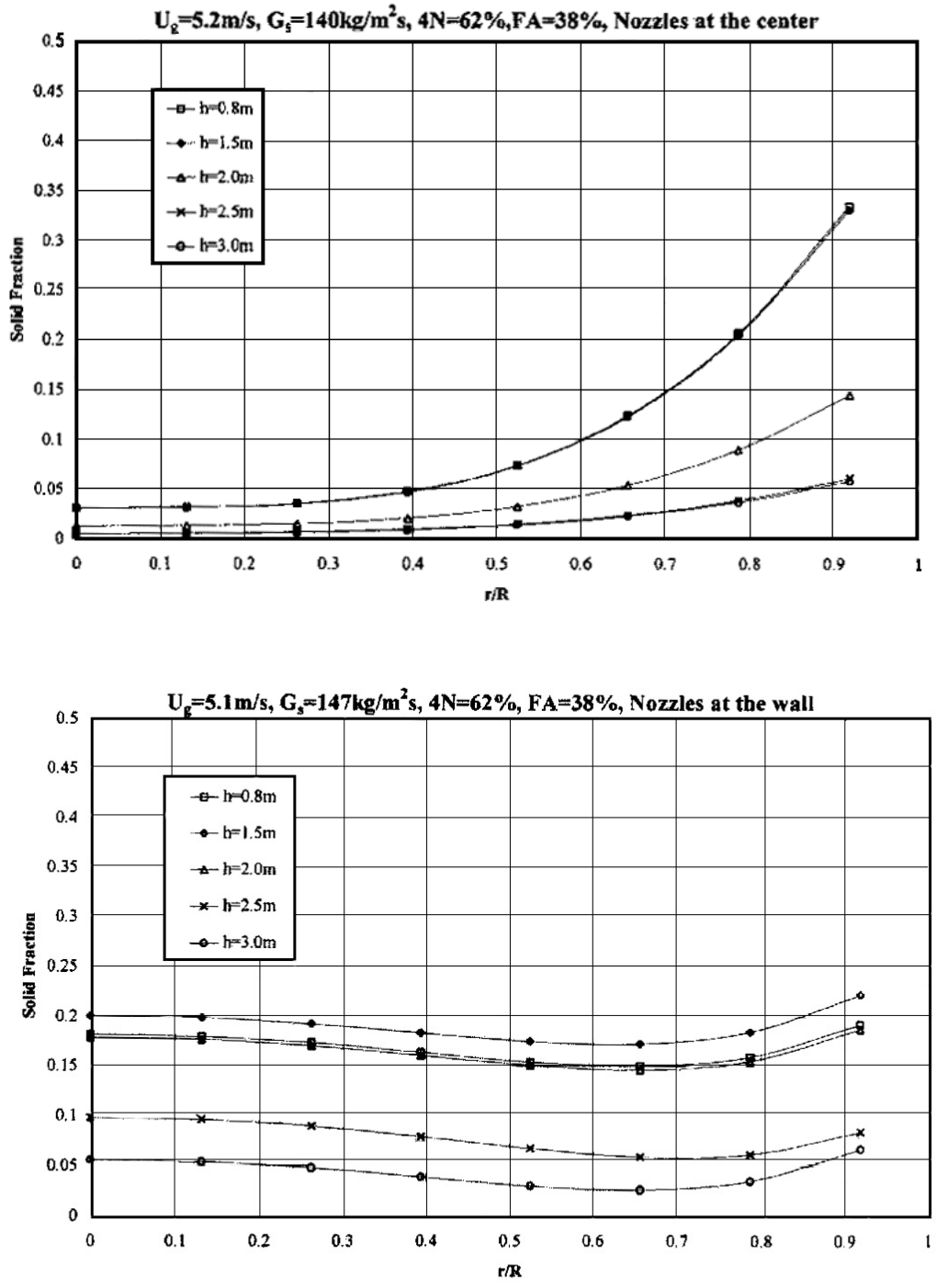

Figure 2.4.5.2 Radial Solid Fraction Profiles (Kostazos 1997)

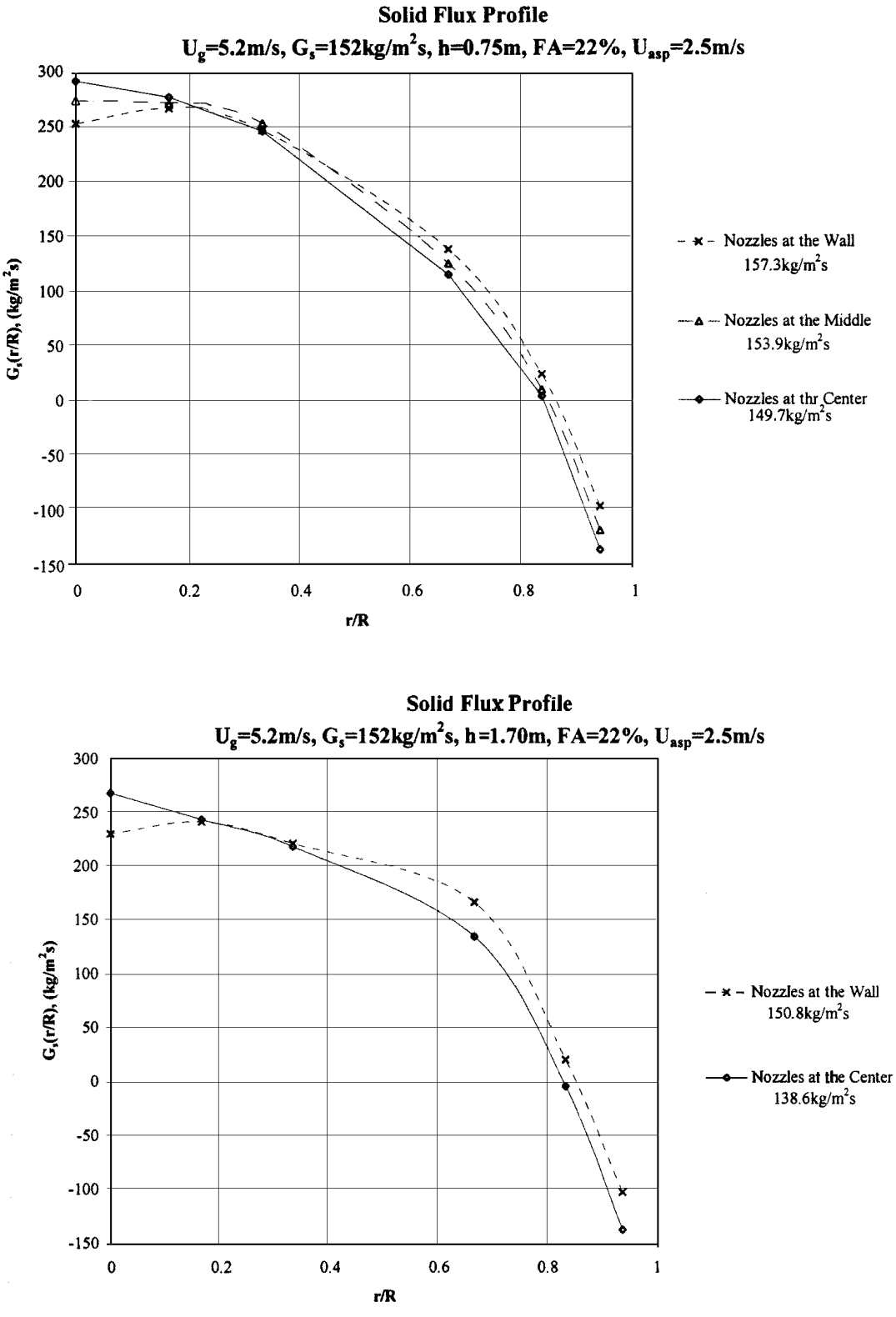

Figure 2.4.5.3 Radial Solid Flux Profiles (Kostazos 1997)

III. EXPERIMENTAL FACILITY

3.1 The Coaxial Flow Riser

The City College fast fluidization unit was modified for this investigation. A schematic of the new system is shown in Figure 3.1.1. This unit mainly consists of a tube serving as riser, a two-stage gas-solids separation system, a standpipe or "downcomer " to recirculate the solids and an entrance section to bring the gas and solid together.

The unit modification consisted of a new entrance section designed to provide the coaxial flow and is shown in Figure 3.1.2. The riser is made of Plexiglas with a total height of 8.50 m and a I.D. of 15.20cm. A coaxially mounted Plexiglas tube of length 1.83m, 9.53cm O.D. and 8.89cm I.D. serves as the Inner primary jet. In order to control the outer to inner flow rate ratio, accelerating gas for the catalyst flow is fed separately to both the inner tube and the annular section. In the annular flow region, four nozzles, 2.54cm ID each, are mounted just above the bottom of the inner separating duct with their axes parallel to the riser axis. Their flow rates were separately controlled by four rotameters.

The riser terminates in an elbow which carries gas and solids to a two-stage cyclone separation system. The first cyclone stage is incorporated directly into the top of the 34.30cm ID standpipe. The standpipe holds solids in a fluidized state with solids downflow. The 6 m high standpipe terminates 2 m off the floor into a 15.20cm U-tube which also forms the bottom of the riser. A solids flow control valve sits in this U-tube right under the standpipe. The U-tube section is equipped with four nozzles which, with the solid control butterfly valve, provide control of the solid circulation rate. The air flow from the four nozzles carries the catalyst in dense flow up above the elevation of the bottom of the inner duct. The air from the nozzles above the bottom of the inner duct accelerate catalyst powder along both paths.

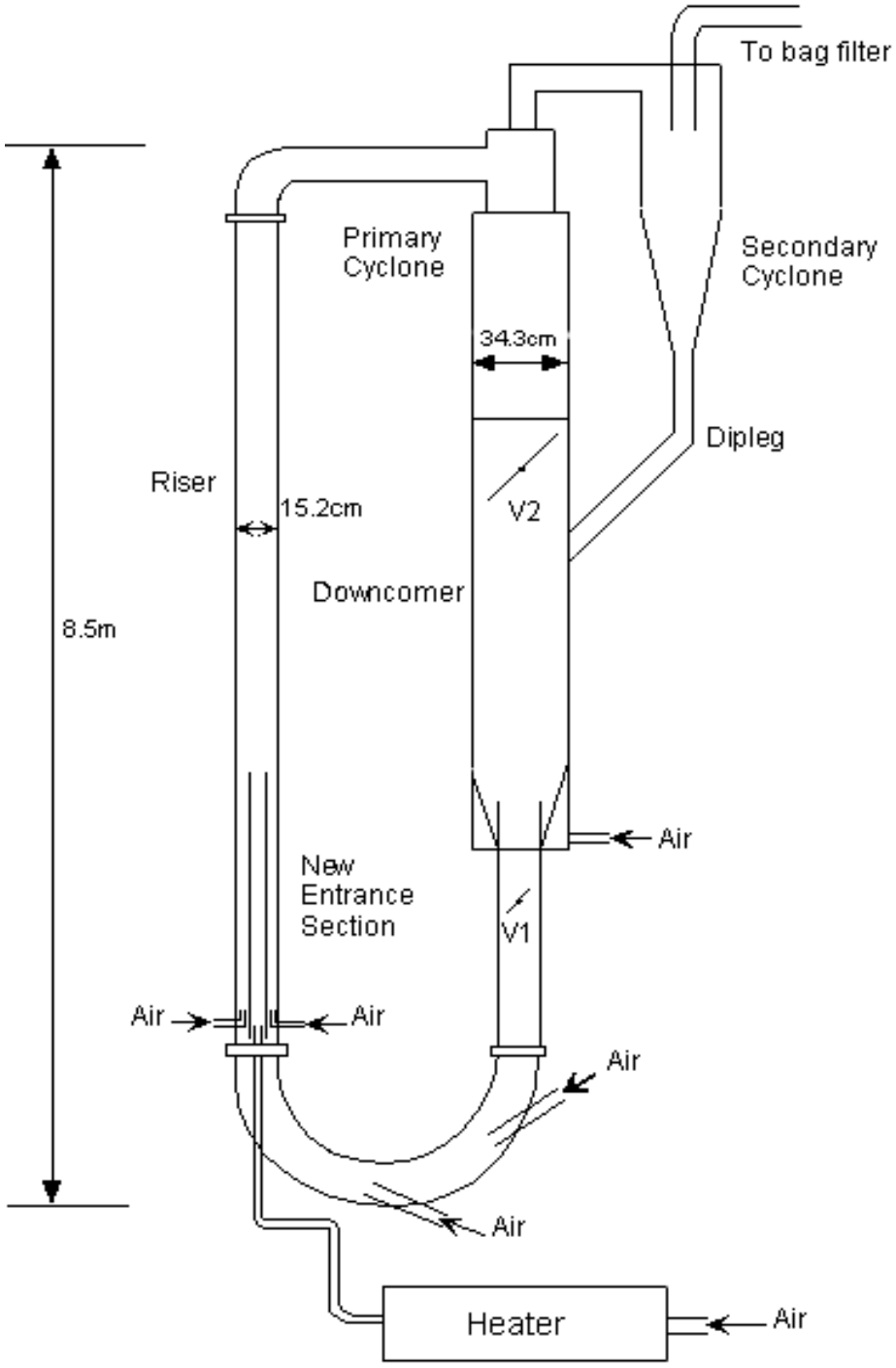

Figure 3.1.1 The Modified City College Fast Fluidization Facility

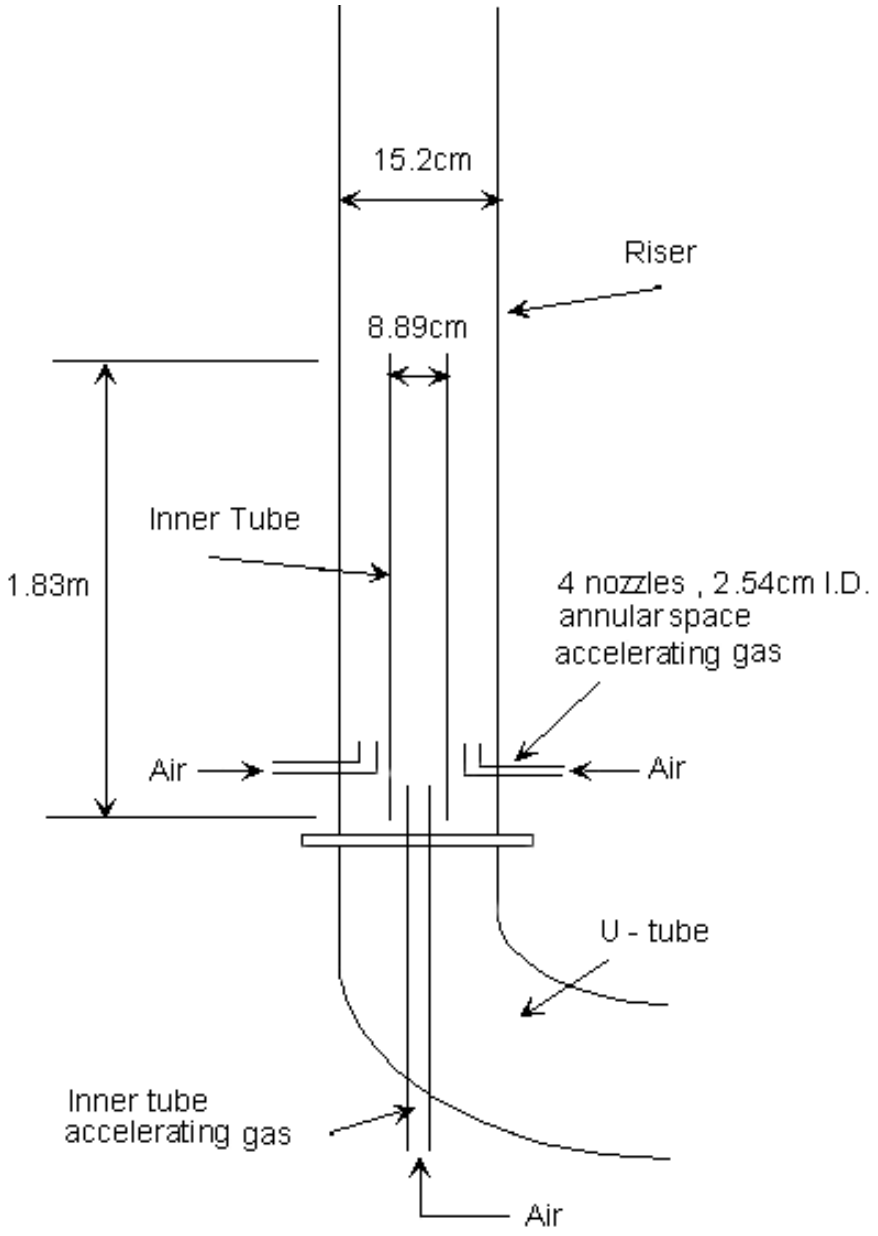

Figure 3.1.2 New Entrance Section of the Coaxial Flow Riser

3.2 Heating System

To study the coaxial gas-solid flow with different stream temperature, a heating system was used in this investigation. Prior to entering the bed, the acceleration gas to the inner tube can be heated up to a temperature as high as 200^{o}F by passing it through this heating system. As shown in Figure 3.2.1, the heating system consists of 10 individual finned strip heaters placed inside a cylindrical, 30 cm ID, 3 m long insulated tube which provide the air with a maximum of 7 KW of heat. Heaters are placed perpendicular to the air flow, along the axis of the tube, 25 cm apart from one another. Each heater is surrounded by a circular 30 cm diameter metal sheet with an opening slightly bigger than the size of the heater to conduct the air flow through the fins. To further enhance the efficiency of heat transfer to the air, each subsequent heater is rotated at 90° with respect to the preceding one.

The air temperature is controlled in three separate steps, by means of three proportional single-output temperature and process controllers, Omega CN 8500 series, coupled with three Copper-Constantan ungrounded thermocouples which read the air temperature at two different positions

along the heater and at the air inlet to the fluidized bed. The temperature control diagram is shown in Figure 3.2.2.

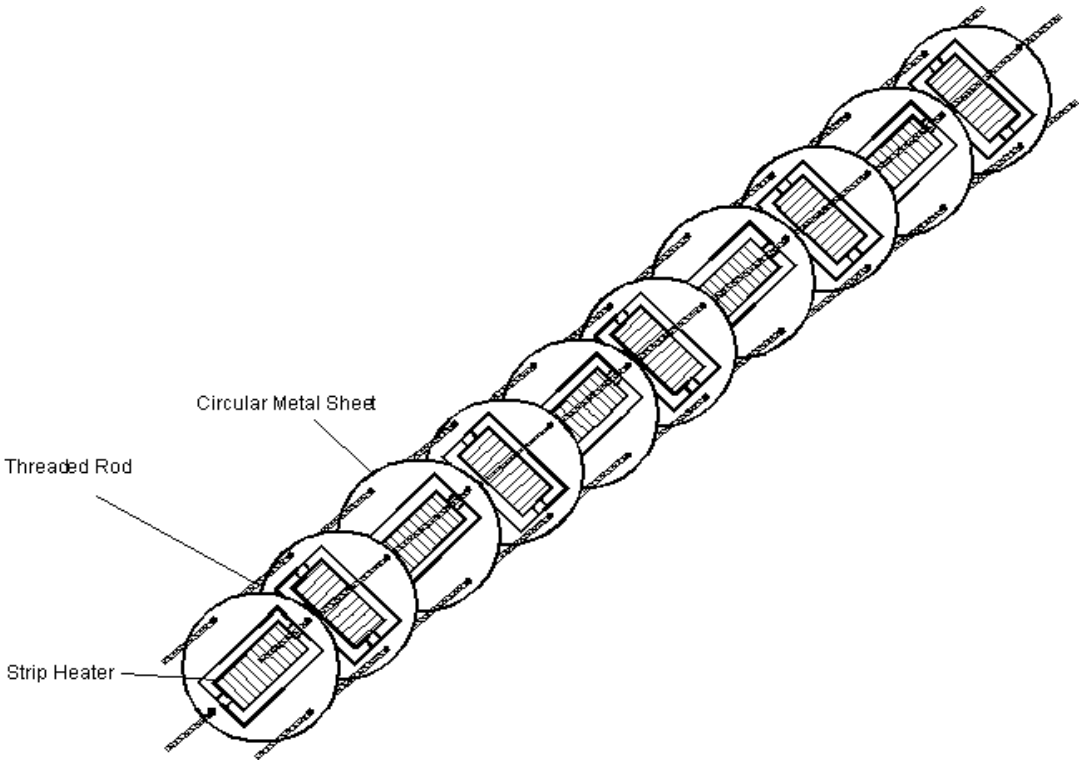

Figure 3.2.1 Internal Parts of the Heater

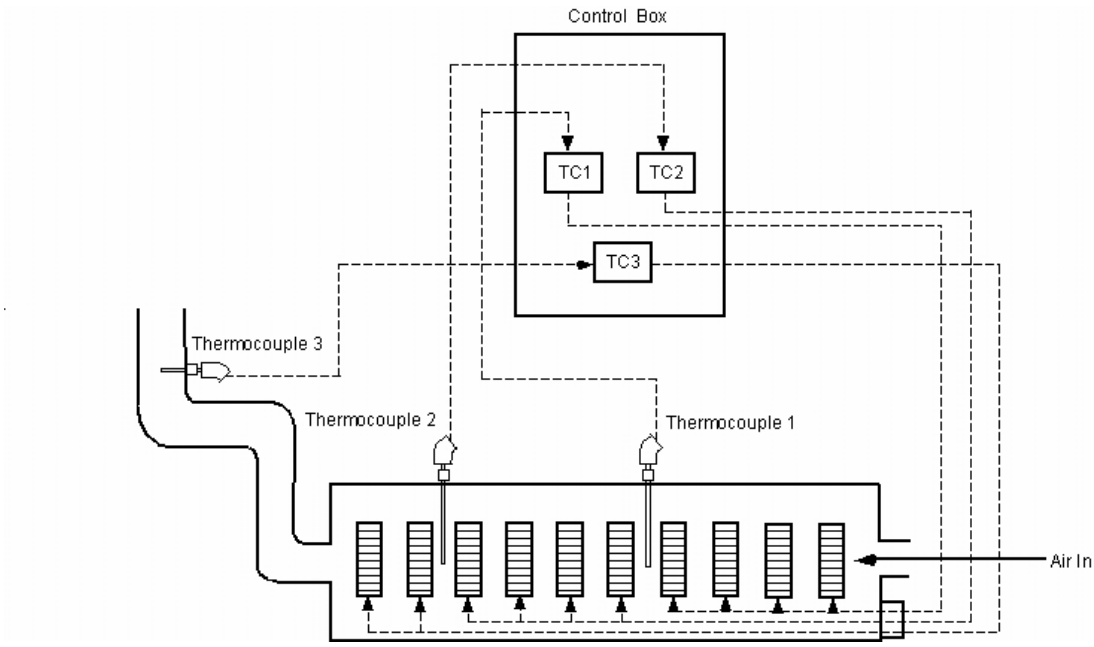

Figure 3.2.2 The Control System of the Heater

IV. EXPERIMENTAL METHODS

To characterize the coaxial gas-solid flow in the riser, the axial and radial pressure profiles, the radial profiles of solid volume fraction and local solid flux, the gas dispersion and temperature distribution were measured in this investigation. The measurement locations are shown in Figure 4.0.1. Table 4.01 is a list of the types of data measured and the instrumentation used to make the measurements.

Table 4.0.1 List of the Types of Data Measured and the Instrumentation Used

Types of the Data Measured	Instrumentation Used
Axial pressure profiles, P(z)	Pressure transducers
Radial Pressure Profiles, P(r)	Pressure transducers, Traversing
Total Solid Circulation Rate, G_s	Pressure transducers / Porous butterfly value
Local Solid Flux, $G_s(r)$	Suction probe, Traversing
Solid Volume Fraction, $1-\varepsilon$ (r)	X-ray system
Tracer Concentration, C(r)	GOWMAC thermal conductivity analyzer, Traversing
Temperature Distribution, T(r)	Thermocouple, Traversing

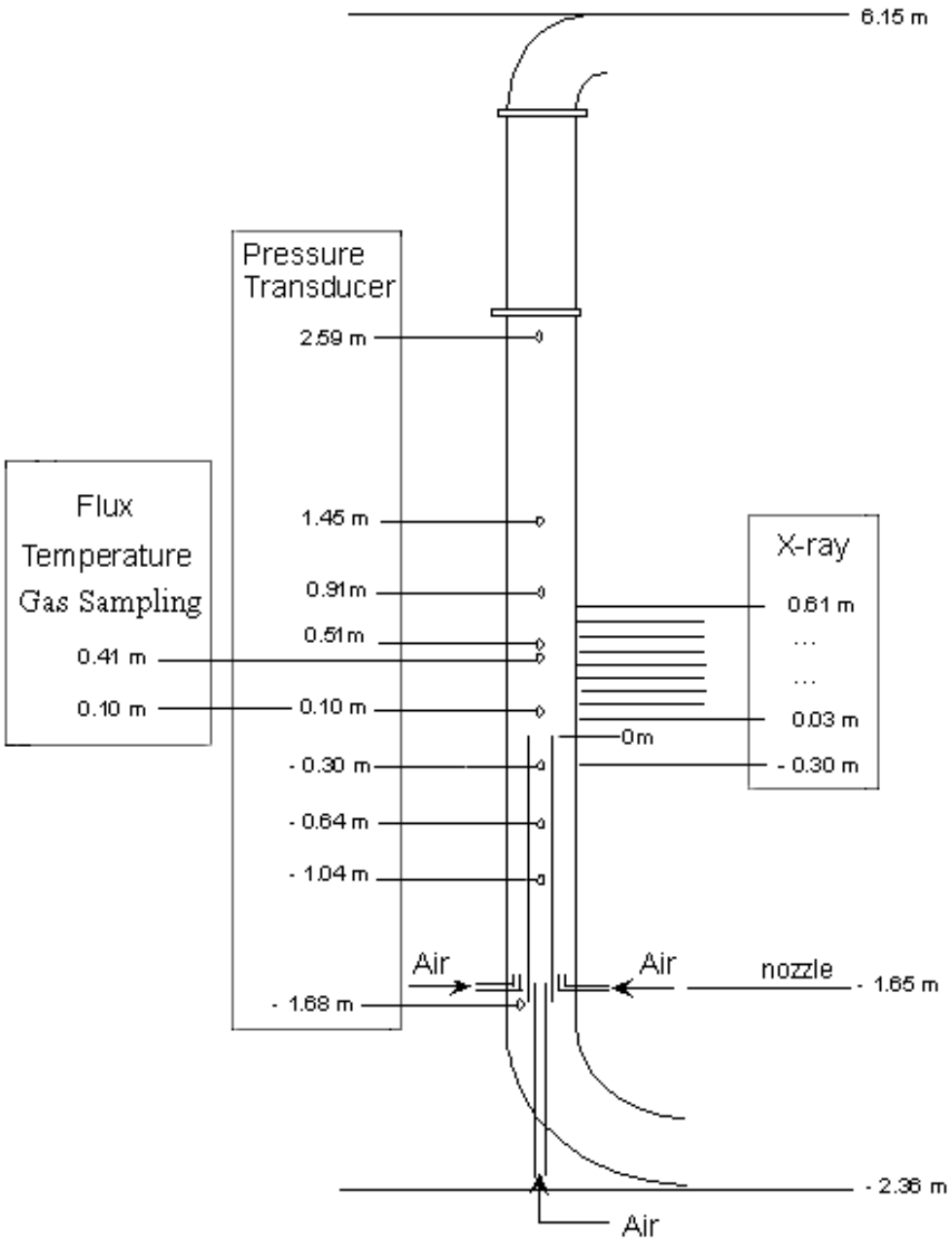

Figure 4.0.1 Coaxial Flow Riser with Measurement Locations

4.1 Pressure Measurements

The circulating system has 28 fixed wall pressure taps for pressure measurements. In this investigation, 10 of them were used to measure the axial pressure profile of the riser. The pressure probes are copper tubes with I.D. of 3.175mm. When measuring the axial pressure profiles, the probes are inserted into the column terminating flush with the inside column wall. To prevent powder from entering the probe, purge gas is used in each pressure tap supplied by a separate compressor. The purge gas velocities are all maintained at the same value. The difference in the backpressures of the purge gas in the two probes going to each transducer is measured as shown in Figure 4.1.1. Each pair of pressure probes is connected across a Honneywell Microswitch piezo-resistive pressure transducer hardwired to a Keithley Metrabyte DAS-20, 12bit A/D board mounted in the computer system. The proper purge gas velocity in the probes is determined by experiment and calibration. Kostazos (1997) found that the air velocity should be above 0.35 m/s to prevent powder from entering the probe and to minimize distortion of the pressure fluctuation signal.

To measure the radial pressure profiles, two types of pressure probes were used as shown in Figure 4.1.2. During the measurement, one probe was placed at an arbitrary location as a reference, the other traversed the bed along a diameter.

The output signal range of the transducers is 0 to 6 volts. Their frequency response is 1 to 10 KHz. To reduce the damping of the pressure signal, the tubing which connects the transducers and probes was arranged as short as possible. A sensitive DWYER micromanometer was used to calibrate each individual transducer. Typical calibration curves are shown in Figure 4.1.3.

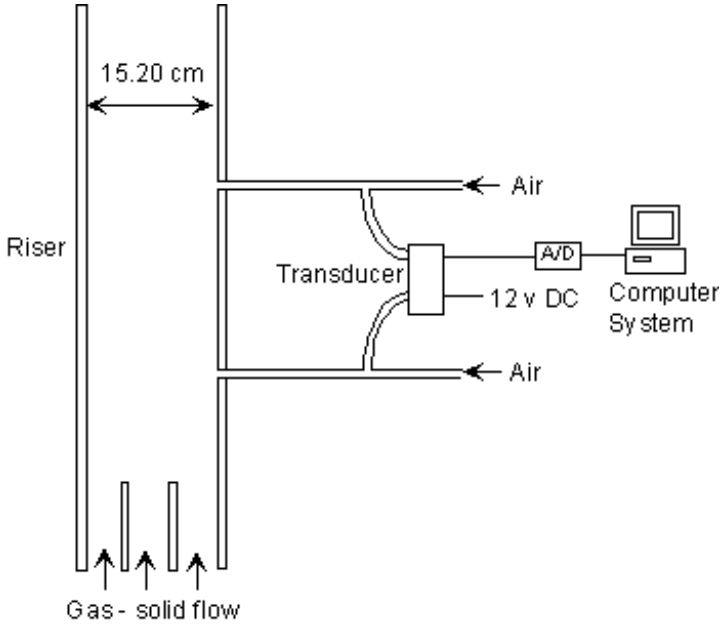

Figure 4.1.1 Wall Axial Pressure Measurement Setup

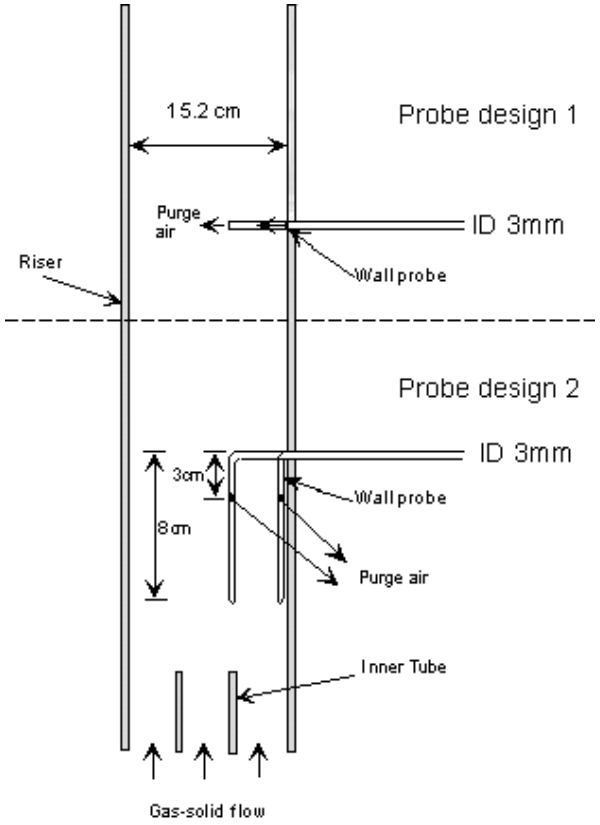

Figure 4.1.2 Radial Pressure Measurement Setup

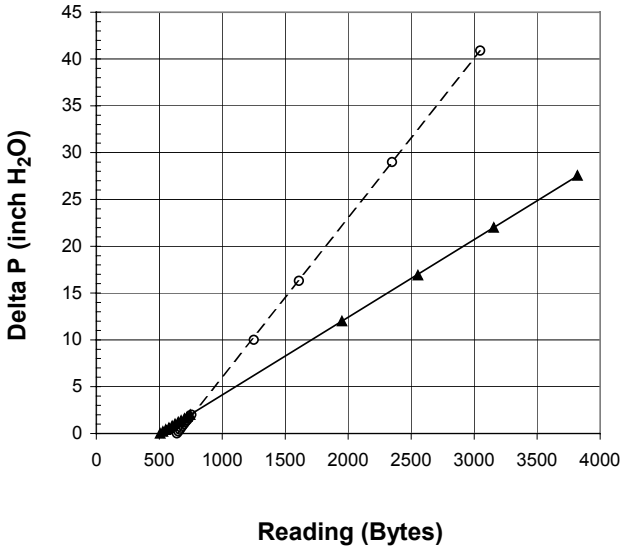

Figure 4.1.3 Calibration Curves for Two Pressure Transducers with Different Ranges

Data from the transducers are recorded at 100Hz. The measuring time or record length is also a very important parameter. Previous work (Kostazos, 1997) has shown that for record lengths of 60s or longer, the variation of mean pressure difference is typically less than 2%. In this investigation, record lengths of data were taken of at least 80s.

4.2 Total Solid Circulation Rate Measurement

The downcomer is kept in a steady fluidized condition with downflow during the run. When the porous plate butterfly valve in the middle of the downcomer is closed, the circulated solids are then held and fluidized above the valve, and the bed below the valve is carried away. This valve has negligible influence on the pressure balance of the circulating system because of the negligible pressure drop through its sintered plate. The total solid circulation rate can be calculated from the pressure drop in the section below this valve as a function of time. Figure 4.2.1 shows a typical pressure signal for the solid circulation rate measurement. The pressure difference decreased linearly when the valve was closed and returned to normal running conditions after the valve was reopened. The decreasing rate of the pressure drop is proportional to the mass flow rate of the fluidized solid

between these two taps. The slope of the signal is calculated by applying linear regression. The solid circulation rate can be evaluated by:

$$G_s = \frac{A_{downcomer}}{A_{riser}} \frac{1}{g} \frac{d(\Delta P)}{dt} \qquad (4.2.1)$$

Where : G_s is the total solid circulation rate, kg/m ^{2}s

$A_{downcomer}$ is the cross-sectional area of the downcomer

A_{riser} is the cross-sectional area of the riser

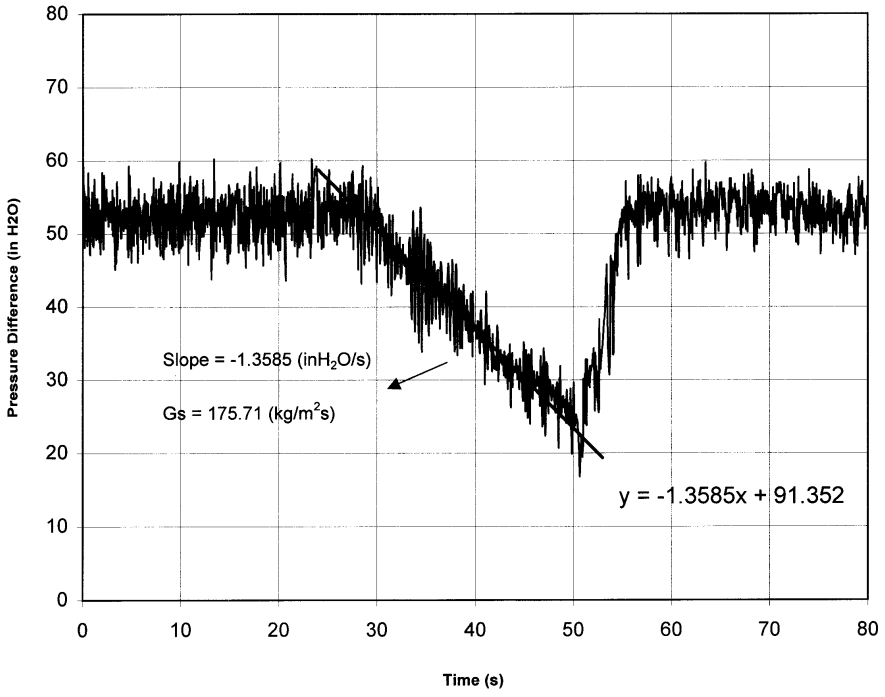

Figure 4.2.1 Time Series of the Pressure Signal for Solid Circulation Rate Measurement

Schnitzlein and Weinstein (1988) have reported that when using this method, the error range of the detected solid recirculation rate is less than 5%.

4.3 Local Solid Flux Measurements

A simple suction probe is usually used to measure the time-averaged solid flux in the fluidized bed. The principle is actually quite simple. The solid is withdrawn through a probe at about the same velocity as the gas superficial velocity, then the solid and gas are separated. The local solid flux is calculated from the weight of solid collected over a period time. Since the complexity of the gas-solid flow is high, the isokinetic sampling condition can hardly be satisfied in the circulating fluidized bed, where both the quantity and the direction of gas and solids flows may fluctuate. A suction probe can, however, be operated in the circulating fluidized bed in the non-isokinetic suction mode. It has been shown by previous workers (Monceaux et al., 1986; Herb et al., 1992, Wei et al., 1997) that using a non-isokinetic sampling probe, it is possible to make accurate and reproducible measurements of the net local solid flux, defined as the difference between upward and downward flux.

$$G_s^{net}(r) = G_s^{up}(r) - G_s^{down}(r) \qquad (4.3.1)$$

Previous research (Kostazos, 1997) has shown that the net solid flux is independent of the aspirating velocity under a wide range of operating conditions. Furthermore, the integral over the cross-section of the measured flux always agreed very well with the independently measured total circulation rate in his work.

In this investigation, the probe measurement device developed by Kostazos (1997) was installed at the City College fast fluidized bed. The schematic of the sampling device is shown in Figure 4.3.1. The sampling probe is stainless steel of I.D. 7.54 mm and O.D. 9.54 mm. To eliminate static effects, the probe is properly grounded. The solids in the riser are aspirated with vacuum through the sampling probe into a 1.22m tall and 7.62 cm ID fluidized bed which is maintained at minimum fluidization. The top of this sampling bed is a sintered plate to separate the solids and gas. Two pressure taps are installed along the bed to measure the increase of the pressure difference with time due to filling of the solids aspirated from the riser. Typical signals of pressure difference during the local flux measurements are presented in Figure 4.3.2. The local solid flux can be then calculated from the rate of increase of the pressure difference.

$$G_s(r) = \frac{A_{samplingbe\ d}}{A_{probe}} \frac{1}{g} \frac{d(\Delta P)}{dt} \tag{4.3.2}$$

where $G_s(r)$ is the local solid flux (kg/m^2s)

$A_{samplingbed}$ is the cross sectional area of the sampling bed

A_{probe} is the cross sectional area of the sampling probe

In order to be able to vary the aspirating velocity at the probe tip without the risk of particle sedimentation in and clogging of the horizontal conveying line, a secondary flow of gas is fed into the probe line just after it leaves the bed which allows low gas velocities at the probe tip and sufficiently high conveying velocities after the secondary air injection. The aspirating velocity at the probe tip is kept close to the gas velocity in the riser to minimize the probe disturbance to the gas-solid flow and to insure smooth suction flow. The probe is traversable along the diameter of the bed. Rotating the probe 180 degrees to make the probe face upwards did not change the elevation of the probe location in the bed due to the configuration of the probe. Two similar measurements, one downward and one upward, are made at the same location to obtain the net solid flux.

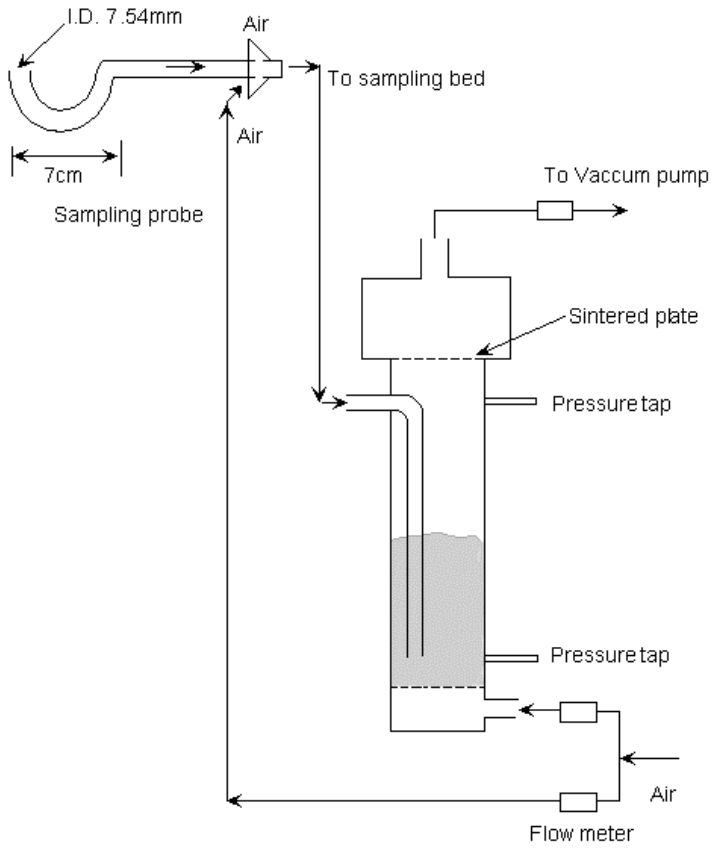

Figure 4.3.1 Local Solid Flux Measurement Device

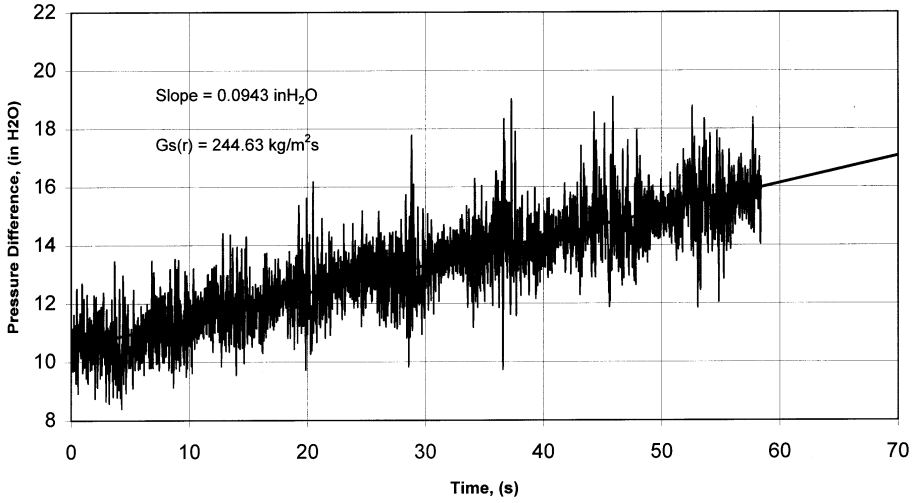

Figure 4.3.2 Typical Pressure Difference Signal of Local Solid Flux Measurement

4.4 Solid Fraction Measurement

4.4.1 X-ray System

The solids volume concentration in fluidized bed systems is generally too high to permit a visual observation of processes inside the bed from outside. Thus, significant difficulties are encountered in studying the flow structure and local fluid properties. Laser Doppler Anemometry is one of the most widely used methods in studying gas-solid flow. It is, however, only suitable for low solids concentrations, such as the upper freeboard of a bubbling fluidized bed (Berkelmann and Renz, 1991). Using an X-ray absorption technique, Weinstein et al. (1984) appear to have presented the first radial voidage profiles in the dense region of a CBF riser. In this investigation, their industrial X-ray system is used for radial solid fraction measurements. A schematic representation of the X-ray system is shown in Figure 4.4.1.1.

The X-ray source is a Norelco MG 150/300 generator which provides high intensity, constant x-ray output. X-rays are first filtered through an aluminum shield to cut off the low frequencies. The filtered beam is considered to be monochromatic. The intensity of the x-ray beam can be controlled by adjusting the operating voltage and current at the control

console. In this work a 150 kV X-ray head is used with a maximum level of 30 mA at 100 kV and 20 mA at 150 kV. The X-ray tube is a fixed anode type with two focal points of 15 and 40 mm. The focal point is chosen to be 40 mm because it provides a wider angle of the X-rays.

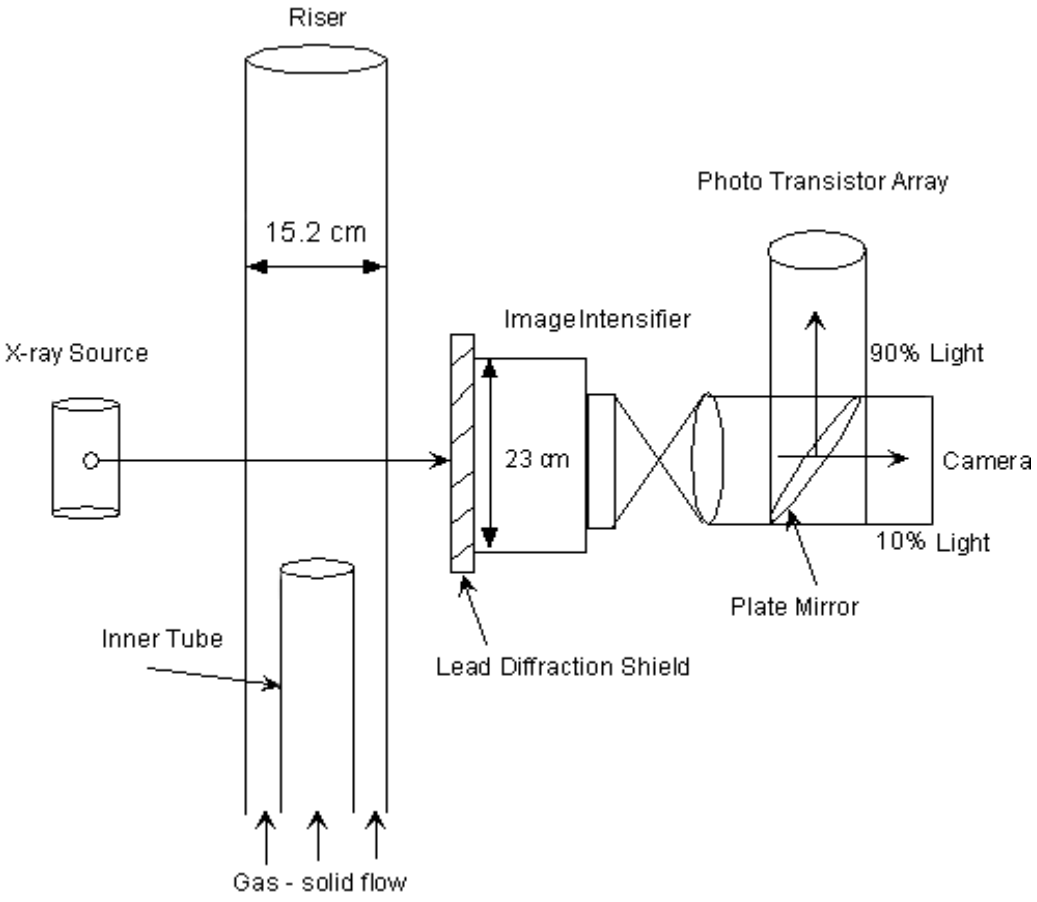

Figure 4.4.1.1 Schematic Representation of the X-Ray System

In order to eliminate the effect of scattered radiation, a lead scatter shield is used before the image intensifier. The shield is made of 2.54cm wide lead

strips which are mounted parallel to the path of the x-ray beams. The X-ray image of the bed is projected onto a 23-cm Phillips image intensifier screen which converts the X-ray into visible light and projects it onto a 7.5 cm output screen. A mirror box is mounted behind the intensifier, with the mirror mounted at an angle of 45° to the beam. Of the projected light, 10% passes through the mirror and is monitored by a closed circuit T.V. camera connected to a monitor in the control room, and 90% is projected onto a curved 15 cm plexiglas screen by means of a focal lens. The plexiglas screen is equipped with 48 SKN 042 NPN silicon phototransistors arranged in an array of three rows, all at equal distance from the image intensifier screen. In this measurement, one row is used to scan the projected image of the bed at 1.4 cm intervals. The response frequency of the phototransistors is 1MHz. To provide a low noise/signal ratio the outputs of the phototransistors are connected to a dual JFET operational amplifiers. The output range is between 0 and 10 volts. The final output is then converted into digital bytes by means of a Metra-Byte DAS20 Analogue-to-Digital board in a real time computer system with a sampling frequency of 100 Hz. The circuit diagram of each sensor element is presented in Figure 4.4.1.2.

The whole X-ray system is mounted on a platform which can be moved vertically up and down to a desired measurement location by means of a

winch. The winch is controlled from the control room and is monitored by a video camera.

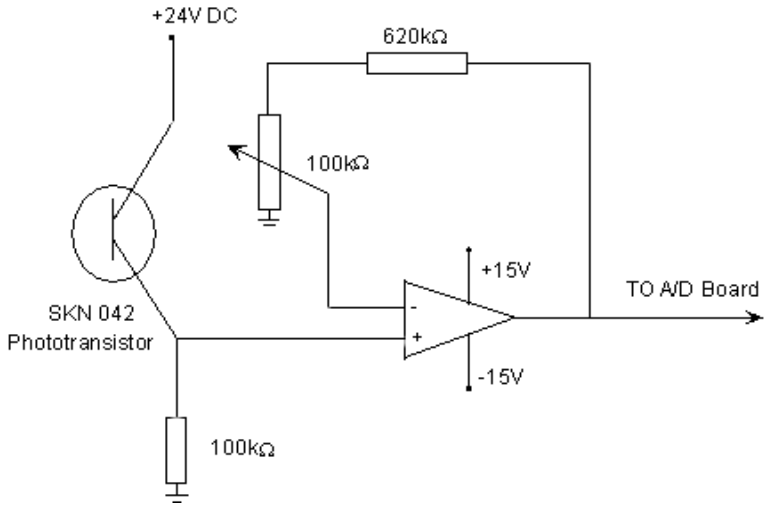

Figure 4.4.1.2 Circuit Diagram of Sensor Elements

4.4.2 Radial Solid Fraction Measurement Principle

Filtered by an aluminum plate, the final x-ray beam has a narrow frequency distribution and behaves similarly to a monochromatic beam. According to the Beer-Lambert law, the decrease in intensity of a monochromatic beam is proportional to the thickness of the absorbing material it passes through and can be described as:

$$I = I_0 . e^{-\mu . x} \qquad (4.4.2.1)$$

where: Io is the initial intensity of the x-ray beam

x is the traveled length of the beam in the absorbing medium

μ is the attenuation coefficient

Furthermore, for mono-energetic beams, the amount of radiation absorbed by a medium is proportional to the density of the medium:

$$\mu = k . \rho \qquad (4.4.2.2)$$

Where k is the mass attenuation coefficient and ρ is the density of the medium, averaged over the traveled length of the beam.

When an x-ray beam travels through an absorbing material, it loses its energy due to absorption and scattering phenomena. Scattering is the effect wherein the beam changes its direction and does not reach a receiver placed along the original beam path. As mentioned before, the effect of the scattering is minimized by the scatter shield described above.

Two sets of X-ray data are taken at each measurement location, one during the run and one before the run with an empty bed. Applying the Beer-

Lambert law, the intensity of a beam passing through the running bed can be described as:

$$\ln \frac{I_{w+s}}{I_0} = -(k.\rho)_w x_w - (k.\rho)_s x_s \qquad (4.4.2.3)$$

When X-rays pass through the empty bed, the Beer-Lambert law gives:

$$\ln \frac{I_w}{I_0} = -(k.\rho)_w x_w \qquad (4.4.2.4)$$

In above equations:

I_{W+S} is the intensity of the beam after passing through the running bed

I_W is the intensity of the beam after passing through the empty riser

I_0 is the initial intensity of the beam

x_S is the travel distance inside the riser

x_W is the travel distance in the wall of the riser

Combining equations (4.4.2.3) and (4.4.2.4) will eliminate the attenuation contributed by the wall and thus gives the detected beam intensity as a function of the solid bulk density:

$$\ln \frac{I_w}{I_{w+s}} = -(k.\rho)_s x_s \qquad (4.4.2.5)$$

Rewriting the equation in terms of the solid fraction of the absorbing medium, we get:

$$\ln \frac{I_w}{I_{w+s}} = k_s . \rho_p (1-\varepsilon) x_s \qquad (4.4.2.6)$$

Where ρ_p and ε are the particle density and bed void fraction, respectively.

4.4.3 Calibration

In order to calculate solid fractions in the coaxial flow, a calibration of the X-ray system to find the mass attenuation coefficient, $k_{s,}$ must be made. Two Plexiglas boxes of widths 2.54cm and 5.08 cm were used for the calibration measurements. The intensities of beams were detected after passing through first the empty boxes and then after passing through the boxes holding packed beds of the fluidized powder. Knowing the bed density and the travel distance, the mass attenuation coefficient can be determined according to equation (4.4.2.5). Figure 4.4.3.1 presents the calibration curve for the FCC catalyst used in this investigation.

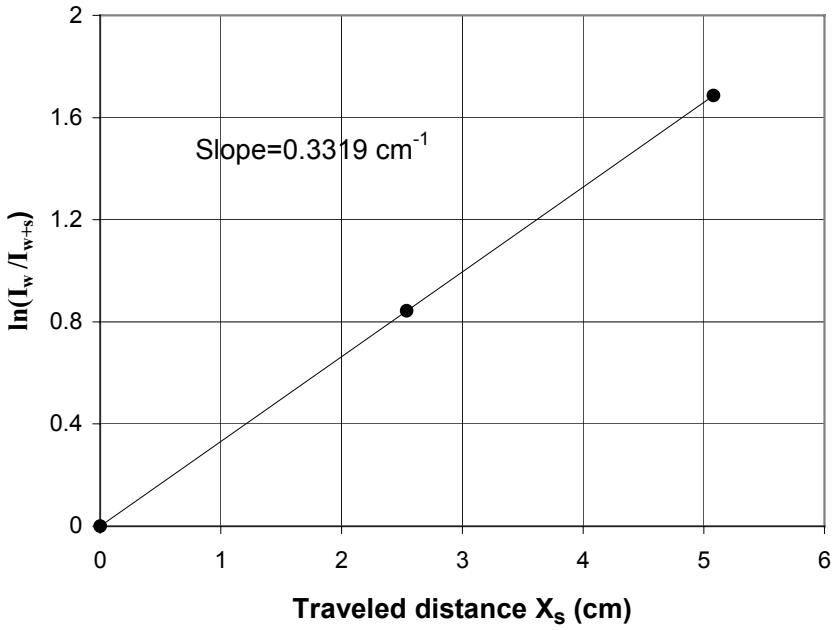

Figure 4.4.3.1 X-ray Calibration Curve of FCC Catalyst

4.4.4 Method of Image Reconstruction

When the X-ray beam passes through a non-homogeneous suspension, the detected attenuation should be the integral of the local attenuation along the beam path AB as presented in Figure 4.4.4.1. The equation (4.4.2.6) then becomes

$$\ln \frac{I_w}{I_{w+s}} = \int_A^B k_s \cdot \rho_P \cdot \left(1 - \varepsilon(x, y)\right) \cdot ds \qquad (4.4.4.1)$$

Assuming axial symmetry, the movable coordinates x and y are related to r simply by $r = \sqrt{x^2 + y^2}$. The solid density distribution can be expressed as a function of r in a polynomial form.

$$1 - \varepsilon(r) = a_o + a_1 r + a_2 \cdot r^2 + \cdots\cdots + a_n \cdot r^n \qquad (4.4.4.2)$$

The axial symmetry assumption gives the boundary condition

$$\frac{\partial \rho(r)}{\partial r}\Big|_{r=0} = 0 \qquad (4.4.4.3)$$

The coefficient a_1 becomes zero. The equation (4.4.4.1) can be written as

$$\ln \frac{I_w}{I_{w+s}} = \int_A^B k_s \rho_P \cdot \left(a_o + a_2 \cdot r^2 + \cdots + a_n \cdot r^n\right) \cdot ds \qquad (4.4.4.4)$$

From the geometrical relations shown in Figure 4.4.4.1,

$$dx = ds \qquad y = D \sin\theta \qquad (4.4.4.5)$$

$$r = \sqrt{x^2 + y^2} = \sqrt{x^2 + D^2 \sin^2\theta}$$

$$X_s = AB = 2\sqrt{R^2 - D^2 \sin^2\theta}$$

The equation (4.4.4.4) can thus be rewritten as

$$(\frac{1}{k_s \rho_P}) \ln \frac{I_w}{I_{w+s}} = 2\int_0^{\frac{X_s}{2}} \left(a_o + a_2 \cdot r^2 + \cdots + a_n \cdot r^n\right) \cdot dx$$

$$= 2(a_o \cdot P_o + a_2 \cdot P_2 + \cdots + a_n \cdot P_n) \qquad (4.4.4.6)$$

Where

$$P_o = \frac{X_s}{2} = \sqrt{R^2 - D^2 \sin^2 \theta} \qquad (4.4.4.7)$$

$$P_2 = \int_0^{\frac{X_s}{2}} (x^2 + D^2 \sin^2 \theta)\ dx = \frac{1}{24} {X_s}^3 + \frac{X_s}{2} D^2 \sin^2 \theta$$

……

$$P_n = \int_0^{\frac{X_s}{2}} (x^2 + D^2 \sin^2 \theta)^{\frac{n}{2}} dx$$

The left hand side of the equation is known from the measured signals. The right hand side is a polynomial of nth order. Since ten photodiodes are used in this investigation, the set of equations can be solved by linear regression and optimization for n less than ten. Previous research (Feindt, 1990) has shown that the polynomial order should not be higher than four in order to prevent a sinusoidal profile result.

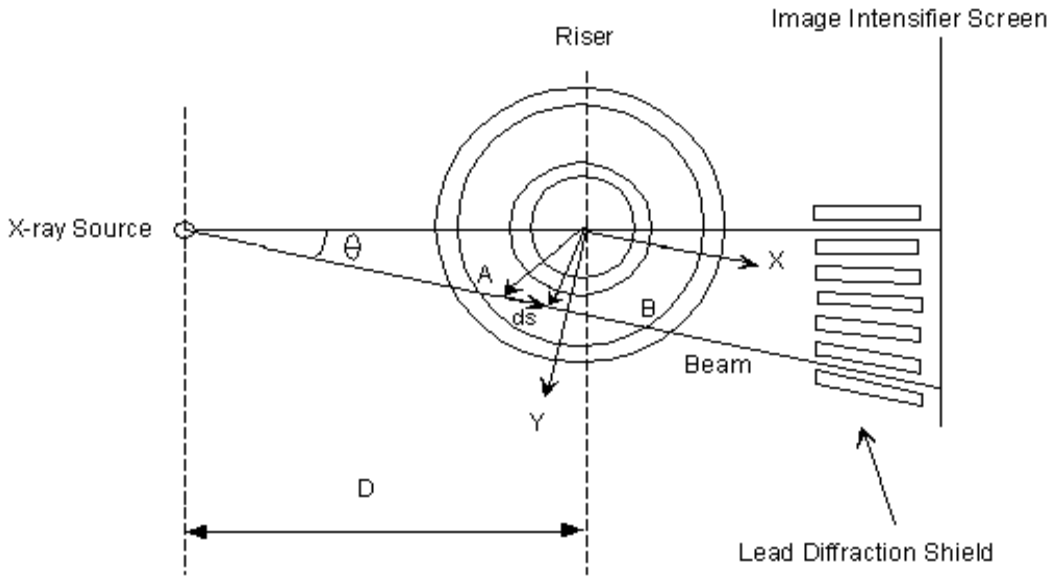

Figure 4.4.4.1 The Geometry for Reconstruction of Solid Fraction Distribution

4.5 Gas Dispersion Measurement

Axial gas flow patterns in a fluidized bed are usually evaluated indirectly by measuring the extent of gas back-mixing using a tracer technique (Cankurt and Yerushalmi (1978), Helmrich et al. (1986), Li and Weinstein (1989)). In this investigation, a gas tracing technique developed by Li and Weinstein (1989) was used to provide a picture of the gas mixing in the initial mixing region of the coaxial flow. Helium was used as the tracer.

The complete set up of the measurement is shown in Figure 4.5.1. A steady stream of tracer gas is continuously injected into the inner tube acceleration gas far enough before the tube end, so that the mixing is complete and the composition of tracer gas in the inner tube is initially uniform before the merge. Samples are taken at three elevations, 0.10m and 0.41m downstream and above the merge plane and 0.3m upstream below the merge plane in the middle of the annular space. The reference gas was taken from 1.04m below the merge at the annular tube. The sample gas and the reference air were drawn into an on-line GOWMAC thermal conductivity analyzer connected to a data acquisition system. The fluctuations in the signal from GOWMAC conductivity analyzer are smoothed by averaging 4096 readings at 100Hz, to provide a recording length long enough to give a reproducible data.

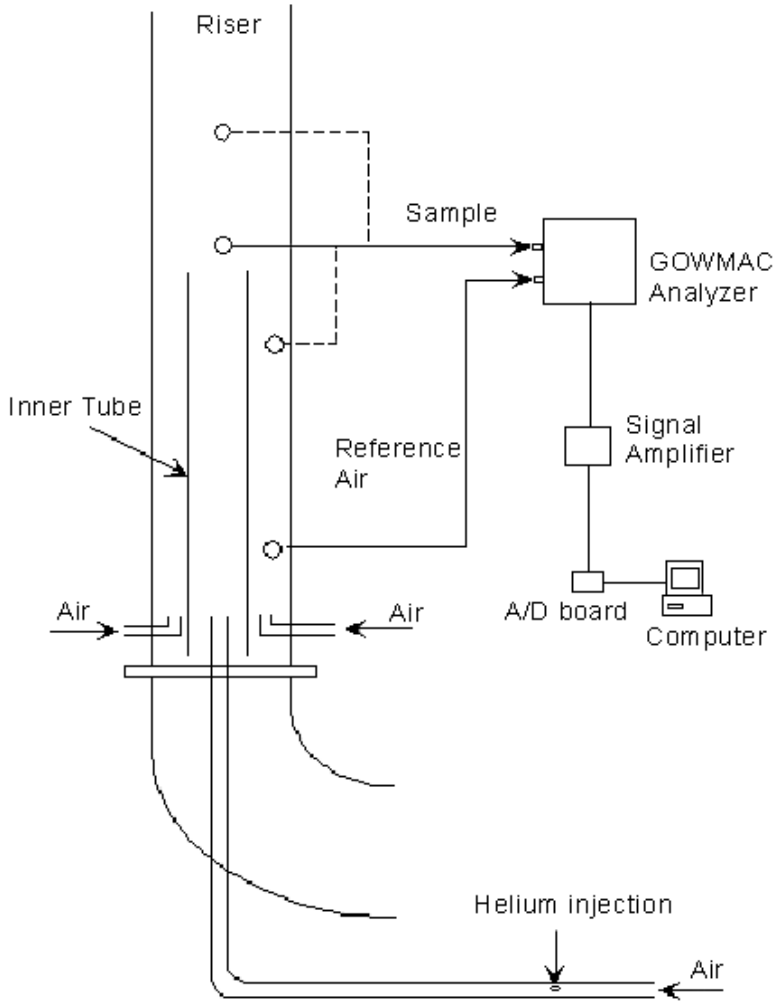

Figure 4.5.1 Gas Dispersion Measurement with Helium Tracing Technique

4.6 Temperature Distribution Measurement

The mixing of the coaxial flow with different stream temperatures is also studied in the investigation. The acceleration gas for the inner tube is heated

up to a selected temperature (75^{o}C) by the heating system as described above. The traversing thermocouple is very well grounded to reduce the electrostatics. The temperature is measured every half inch across the riser. At each point, the thermocouple is held for one minute in order for the temperature reading to stabilize. The entire bed solid inventory is heated up during a run, and a reference measurement is necessary to eliminate this unsteady temperature effect. A thermocouple is installed in the U-tube right below the downcomer to monitor the temperature of the bed solid inventory. The measured temperature is then adjusted as follow

$$T(r) = T_{measured}(r,t) - \Delta T_{bed}(t) \qquad (4.6.1)$$

Where $T(r)$ is the radial temperature distribution

$T_{measured}(r,t)$ is the measured temperature distribution

$\Delta T_{bed}(t) = T_{bed}(t) - T_{bad}(t=0)$ is the temperature change of the bed solid inventory

V. EXPERIMENTAL RESULTS

It is expected that the gas velocity ratio would be just as important a parameter in the mixing of coaxial-flowing gas-solid streams in a riser as it is in the mixing of coaxial-flowing homogeneous streams. To understand the characteristics of the mixing of coaxial flowing gas-solid streams in a riser, the effects of velocity ratio on their mixing behavior must be illustrated. Three coaxial flow cases, with inner to outer stream gas superficial velocity ratio, $U_i/U_o = \lambda$, of less than 1, 1, and greater than 1, were studied. For comparison purposes, the superficial gas velocity above the merge in the riser was kept the same for all three cases. The total solid circulation rate, a key parameter characterizing the gas-solid flow in riser, was also maintained approximately constant for the three runs.

In an initial study, the operating conditions were determined, over which reasonable solid flow rates through the central and annular regions could be maintained. Three sets of conditions were chosen, which covered the largest possible range of the operating space of this unit. These conditions are listed in Table 5.1. As noted above, the individual solid rates upstream of the mixing region were neither controlled nor measured.

Table 5.0.1 Operating Conditions

Run	U_g	U_i	U_o	$\lambda=U_i/U_o$	G_s
1	5.2 m/s	4.3 m/s	6.1 m/s	0.7	~150 kg/m^{2}s
2	5.2 m/s	5.4 m/s	5.4 m/s	1	~150 kg/m^{2}s
3	5.2 m/s	9.5 m/s	3.2 m/s	3	~150 kg/m^{2}s

5.1. Axial Pressure Profile and Apparent Solid Fraction

The axial pressure profile is often used to provide a description of the variation of the solid holdup and thus the characteristics of the gas-solid flow in a riser. In this investigation, axial pressure was measured with pressure probes terminating flush with the inside wall of the riser all along the riser length. The axial locations of these pressure taps are given relative to the top of the center tube in all the figures of the results. The pressures measured between locations –1.6 and 0 m are actually the annular-flow pressures. No pressure measurements were made inside the central tube. Above the top of the central tube, the two streams merge and the wall

pressure tap readings are considered to give the riser pressures at the tap elevations.

In Figure 5.1.1, the three axial pressure profiles along the riser are presented for the three cases, λ=0.7,1 and 3. The pressure profile for the equal velocity case (λ=1) is a relatively smooth curve with a constantly decreasing slope, dP/dx, typical of a riser flow. The pressure gradient falls off almost continuously from the bottom to the top as it approaches a constant value. This behavior is close to that of riser flow where the pressure gradient monotonically approaches a constant value and indicates that the cross-sectional average solid fraction is also almost always decreasing as elevation is increasing. This profile is indicative of a relatively smooth merging of the inner and outer streams. The profile for the case of λ=0.7 is also a relatively smooth curve. For this case also, the axial pressure profile indicates that the two streams merge relatively smoothly.

The axial pressure profile for the λ=3 case, however, does not have a continuously decreasing slope. In Figure 5.1.1, there is a faster decrease in the slope beginning just before the merge than there is in the other two cases and then there is an increasing slope following the merge. Because the axial

pressure profile gives the sum of the effects of both solid holdup and solid acceleration, this profile is indicative of a slowing down of solids in the annulus prior to the merge and then a sharp acceleration and possibly increased holdup following. When this type of profile is observed, it usually means that a zone of solid backmixing is formed in the region of non-uniformly changing slope.

The magnitude of the fluctuations of the differential axial pressure also gives some insight into the dynamics of this gas-solid flow. The standard deviation of the instantaneous axial pressure difference over approximately 0.5 meter of elevation normalized by the mean pressure difference is plotted for each run in Figures 5.1.2 to 5.1.4. It can be seen that a peak in normalized standard deviation, NSD, exists in the 0 to 1m section for all three runs. This peak is an indicator of the high degree of turbulent mixing of the coaxial flow generated by the shear layer in the initial mixing zone.

For the case of λ=0.7, Figure 5.1.2, the peak appears early in the 0 to 0.4m region. The NSD of axial pressure difference decreases to 60% in the 0.4 to 0.9m section, and finally falls to 40% and stays about constant above 0.9m. For the λ=1 case, Figure 5.1.3, the peak is located in the 0.4 to 0.9m section.

In this case, the intensive mixing of two streams appears to take place at a higher elevation than in the λ=0.7 case. For both the λ=0.7 and the λ=1

Figure 5.1.1 Axial Pressure Profiles of the Riser

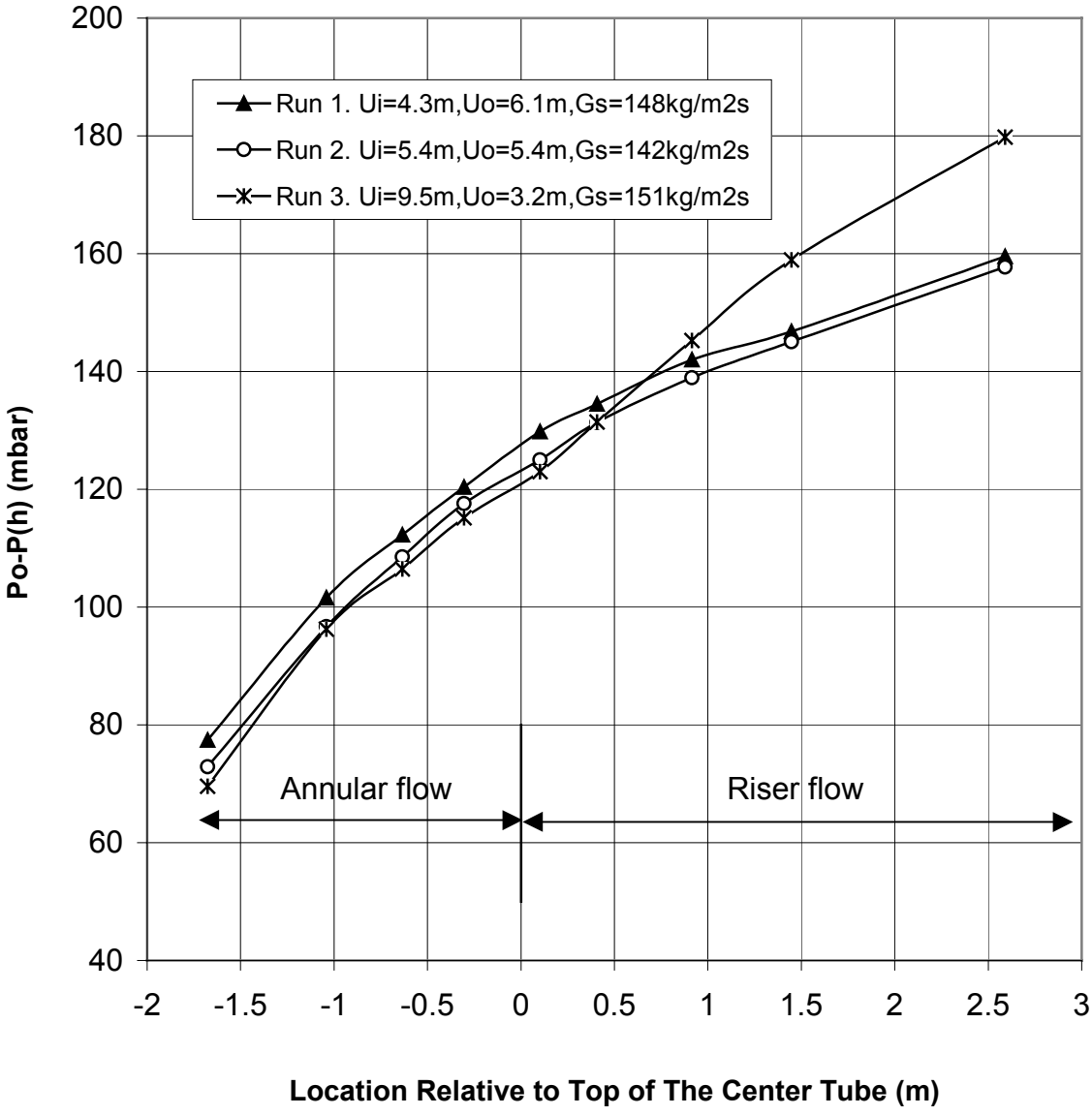

cases, the peaks are narrow, which indicates that merging of the two streams takes place rapidly. Above 0.9m, the flow is approaching typical riser flow and the NSD is almost constant up to the top of riser. This is consistent with the pressure profile, where the pressure gradient is also roughly constant above this elevation.

For the high velocity ratio case (λ=3), Figure 5.1.4, the peak is wider. The mixing extends to higher elevation but appears to be much less intense than other cases. At the 0.9m level, the two streams still do not appear to be fully merged and the flow is still far from typical riser flow. This is also indicated by the axial pressure profile. The magnitude of the NSD of axial pressure differences is smaller compared to the other two cases, because the solid holdup and mean pressure difference are larger in this case.

Figure 5.1.2 Normalized Standard Deviation of Axial Pressure

Run 1. U_g=5.2 m/s, U_i=4.3 m/s, U_o=6.1 m/s, Gs=148 kg/m^{2}s

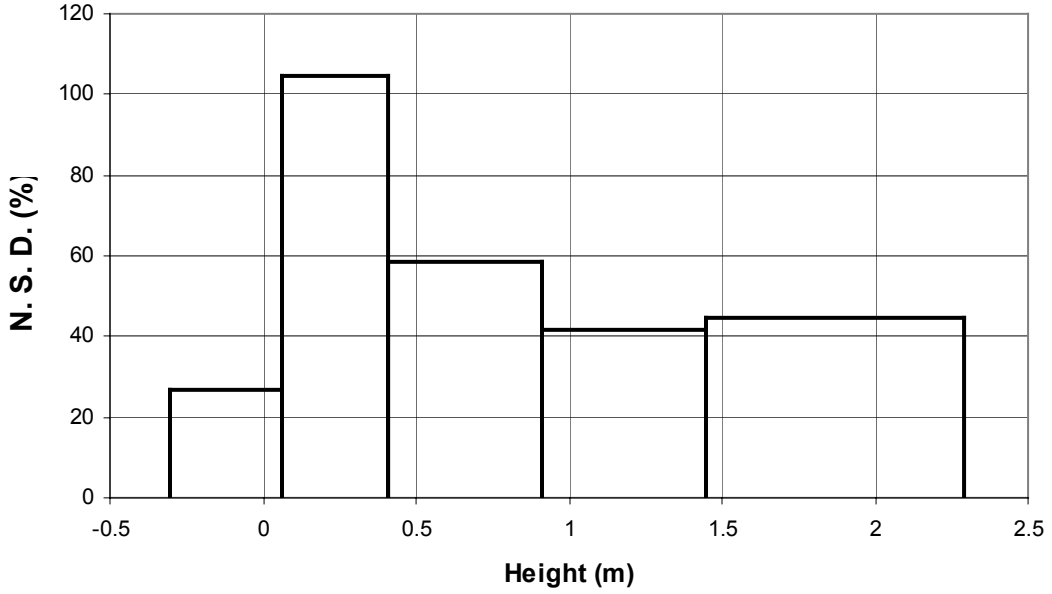

Figure 5.1.3 Normalized Standard Deviation of Axial Pressure

Run 2. U_g=5.2 m/s, U_i=5.4 m/s, U_o=5.4 m/s, Gs=148 kg/m^{2}s

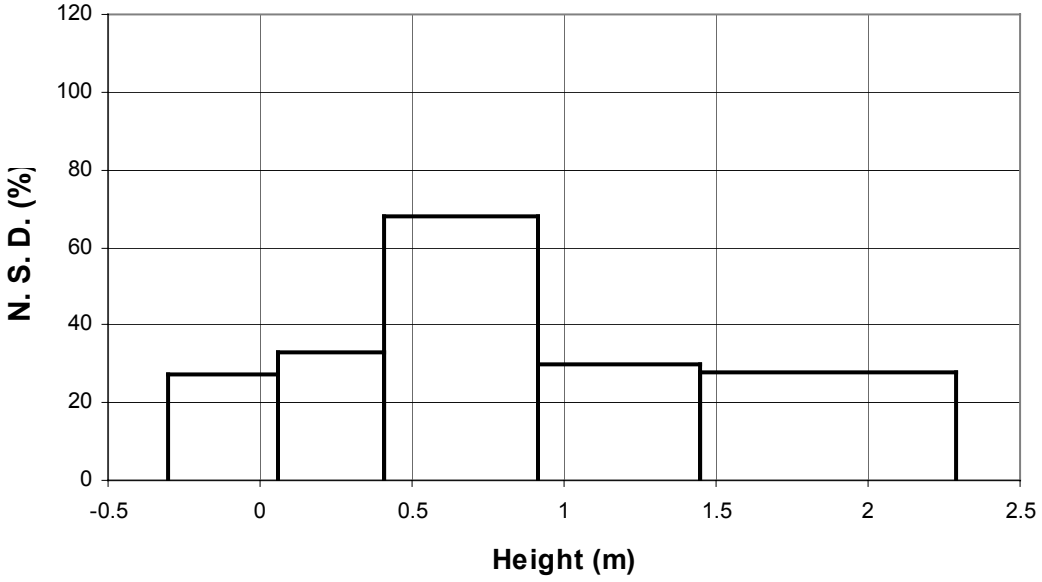

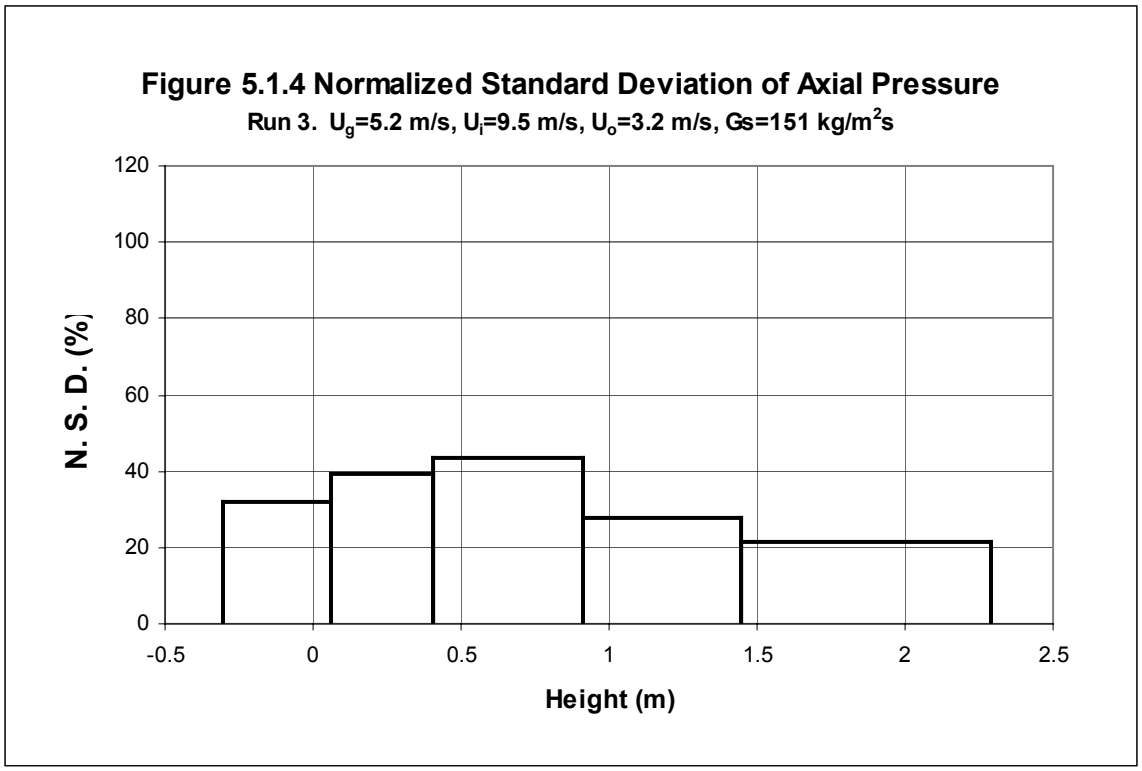

In gas-solid circulating bed fluidization and pneumatic transport, axial pressure profiles are often used to calculate the cross-sectional average solid concentration. This calculated solid fraction is actually an apparent solid fraction, and is an average value over the bed volume within the pressure tap spacing.

$$-\frac{\Delta P_L(r/R=1)}{L} = \rho_s(1-\varepsilon_{apparent})g \qquad (5.1.1)$$

The axial profiles of apparent solid fraction (which is essentially representative of –dP/dx) for the three cases of λ=0.7, 1 and 3, are presented

in Figure 5.1.5. In this figure, the curve lines “connecting” the points of the ~0.5 m average tap spacings have the same areas beneath them as those of a bar graph of the average values. It can be observed that the solids are first accelerated from downflow in the downcomer to upflow in the riser by the air nozzles installed in the U-tube section, resulting in a very high apparent solid holdup. At the entrance of the riser, the solids are further accelerated by the annular nozzles placed just above the bottom of the inner tube, and then reach a near-constant density section before the merge. For all three cases, there is a feedback below the merge of the effects of the merging flows. This is expected in subsonic flows and points out that flow modeling for this complex flow must be elliptic in nature rather than parabolic.

The apparent solid fraction profile for the λ=0.7 case appears to have a high value at the top of the inner tube and decreases right after merge. This is consistent with additional solid holdup right at the merge. Furthermore, in this case the apparent solid fraction eventually approaches a relatively constant value in the upper dilute section, above 1m.

The profile for the λ=1 case decreases at the merge but has a small rise right after the merge. This is probably due to the acceleration of the wake solids

just above the merge. In this case, the apparent solid fraction does not change much before and after the merge, indicates a relatively smooth merge of the two streams. The apparent solid fraction also approaches a relatively constant value above 1 m in the upper dilute section.

The apparent solid holdup for λ=3 case decreases just below the merge and then increases to a value even higher than the value in the annular section. This profile indicates that the solids accelerate after the merge and then

Figure 5.1.5 Apparent Solid Fraction

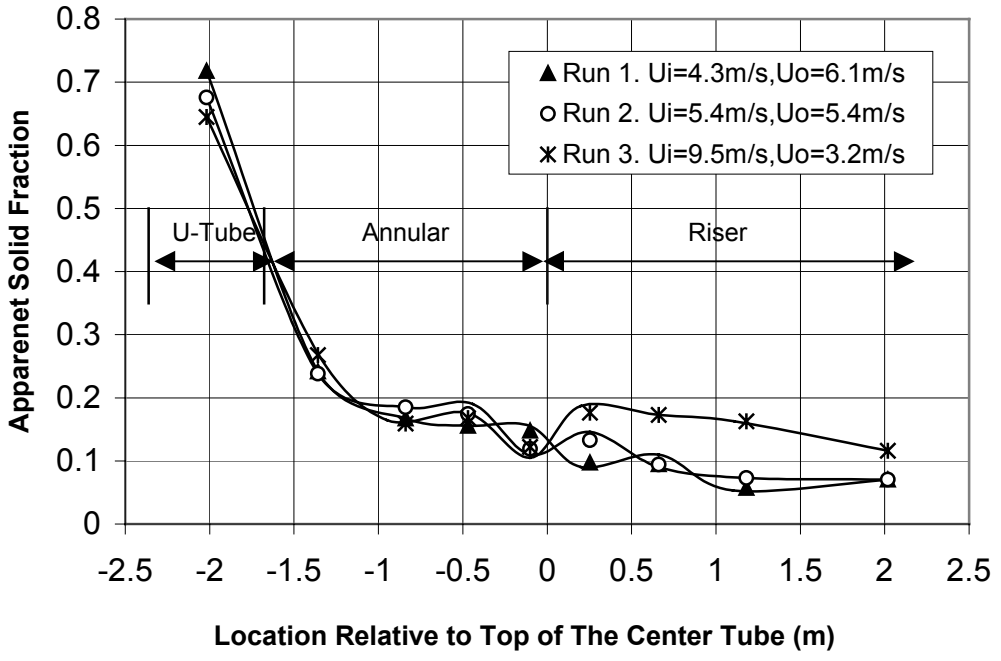

decelerate a little further downstream with an increase in solid fraction. The apparent solid holdup value starts to fall off above 1.4 m but does not reach the relatively flat value of the other two cases by 2 m.

5.2 Comparison between the True and Apparent Solid Fractions

To interpret axial static pressure measurements with the one-dimensional momentum equation, the cross-sectional averaging of any interesting hydrodynamic property Φ is defined as

$$\bar{\Phi} = \frac{1}{\pi R^2}\int_0^R \Phi(r) 2\pi r dr \qquad (5.2.1)$$

The one-dimensional momentum equation (5.2.2) is widely used in studying gas-solid riser flow.

$$-\frac{d\bar{P}}{dx} = \rho_s(1-\overline{\varepsilon_{true}})g + \frac{d}{dx}\left[\rho_s\overline{(1-\varepsilon_{true})U_s^2} + \rho_g\overline{\varepsilon_{true}U_g^2}\right] + \frac{d\overline{P_f}}{dx} \qquad (5.2.2)$$

The right-hand side of equation (5.2.2) has three terms, representing the gravitational effects, the solid acceleration and the frictional effects, respectively. The gas momentum term can be neglected since $\rho_g << \rho_s$. The

friction term, $d\overline{P_f}/dx$, is usually small and negligible compared to the others in beds of this and larger diameters. With these assumptions, equation (5.2.2) becomes:

$$-\frac{d\overline{P}}{dx} = \rho_s(1-\overline{\varepsilon_{true}})g + \frac{d}{dx}\left[\rho_s\overline{(1-\varepsilon_{true})U_s^2}\right] \tag{5.2.3}$$

Equation (5.2.3) can be expressed with differential pressure readings across the pressure tap spacing as:

$$-\frac{\Delta\overline{P_L}}{L} = \rho_s(1-\overline{\overline{\varepsilon_{true}}})g + \frac{\Delta\left[\rho_s\overline{(1-\varepsilon_{true})U_s^2}\right]}{L} \tag{5.2.4}$$

where $\overline{\overline{\varepsilon_{true}}}$ is the cross-sectional average true holdup averaged over L, $\Delta\overline{P_L}$ is the pressure drop measured between two pressure taps, and L is the tap spacing.

To validate the use of the wall pressure/tap pressure drop in equation (5.2.4), radial profiles of pressure were measured at 0.1 nad 0.4 m downstream of the merge. The cross-sectional average pressure drop was calculated and compared to the tap spacing pressure drop for all three runs. In Table 5.2.1, it is seen that the error for all three runs is small.

Table 5.2.1 Pressure Drop Comparison

Run	ΔP(mbar)	Error(mbar)	Error (%)
1	4.7	0.3	6.3
2	8.4	0.09	1.07
3	6.4	0.23	3.59

On the right-hand side of equation (5.2.4), the true solid fraction can be evaluated by cross-sectional averaging of the radial solid fraction data measured with the x-ray system.

Considering that

$$\rho_s(1-\varepsilon_{apparent})g = -\frac{\Delta P_L(r/R=1)}{L} \cong -\frac{\Delta \overline{P_L}}{L} \tag{5.2.5}$$

The one-dimensional momentum equation thus can be written as

$$\rho_s(1-\varepsilon_{apparent})g = \rho_s(1-\overline{\overline{\varepsilon_{true}}})g + \frac{\Delta\left[\rho_s\overline{(1-\varepsilon_{true})U_s^2)}\right]}{L} \tag{5.2.6}$$

According to this one-dimensional momentum equation, when acceleration of solid takes place, the cross-sectional average apparent solid fraction is

greater than the true solid fraction because of the contribution of solid acceleration to the measured pressure gradient. For the same reason, the apparent solid fraction is less than the true solid fraction as deceleration of solid occurs.

The one-dimensional solid continuity equation gives that the net solid flux is not a function of height.

$$\frac{d}{dx}\int_0^R (1-\varepsilon_{true})U_s r dr = 0$$

or

$$G_s = \rho_s \overline{(1-\varepsilon_{true})U_s} = \text{constant} \tag{5.2.7}$$

For a plug like riser flow, generally (Kostazos, 1997)

$$\overline{(1-\varepsilon_{true})U_s} \cong (1-\overline{\varepsilon_{true}})\overline{U_s} \tag{5.2.8}$$

For a plug like riser flow, the solid continuity equation (5.2.7) thus can be written as

$$G_s = \rho_s (1-\overline{\varepsilon_{true}})\overline{U_s} = \text{constant} \tag{5.2.9}$$

Equation (5.2.9) implies that for a typical plug like riser flow, when true acceleration of solids takes place, $(1-\overline{\varepsilon_{true}})$ must be decreasing in the direction of the flow, while when true deceleration takes place, $(1-\overline{\varepsilon_{true}})$ must be increasing in the direction of the flow.

The equality assumed in equation (5.2.9) does not, however, hold when there is a significant flow transition taking place. According to equation (5.2.6) and (5.2.9), the apparent solid fraction is only expected to be equal to the true solid fraction in a typical riser flow where there is essentially no acceleration of solids. However, there are examples of circulating fluidized beds in which the true solid fraction is changing rapidly and yet the true solid fraction and apparent solid fraction are very near equal, as show by Kostazos (1997).

It has been argued that the circulating fluidized bed loop pressure balance usually forces the dense lower region in a riser that thins out to a much more dilute flow above to form the typical S-shaped curve for the solid fraction. A transition region exists between the dense lower region and the dilute upper region, where the dilute core expands rapidly in diameter as shown in Figure 5.2.1. Because the solid fraction $(1-\overline{\varepsilon_{true}})$ is decreasing rapidly with height

in this region, the one-dimensional continuity equation (5.2.9) implies a strongly increasing $\overline{U_s}$, leading to a large value for $\partial\overline{U_s}/\partial$x. The previous study by Kostazos (1997), however, has shown that in this transition zone the data obtained from the pressure gradient, (1- $\varepsilon_{\text{apparent}}$), and the data obtained from the X-ray system, (1-$\overline{\varepsilon_{true}}$), fall on top of each other. When these data are analyzed with the one-dimensional momentum equation (5.2.6) the conclusion must be that

$$\frac{d}{dx}\int_0^R (1-\varepsilon_{true})U_s^2 r dr \cong 0$$

or

$$\frac{d}{dx}[\overline{(1-\varepsilon_{true})U_s^2}] \cong 0 \qquad (5.2.10)$$

Equation (5.2.10) indicates that some solids must be decelerating to balance the accelerating solids that flow through the dense region on their way to higher velocity flow in the dilute riser section. The thinning process in this region masks the acceleration effects by decelerating some of the solids which flow back down along the wall and are reaccelerated at the bottom of the dense region. The disagreement with the solid continuity equation of a plug like riser flow provides clues on the nature of the coaxial flow mixing,

which involve the recirculation patterns that are seen in homogeneous coaxial flow mixing.

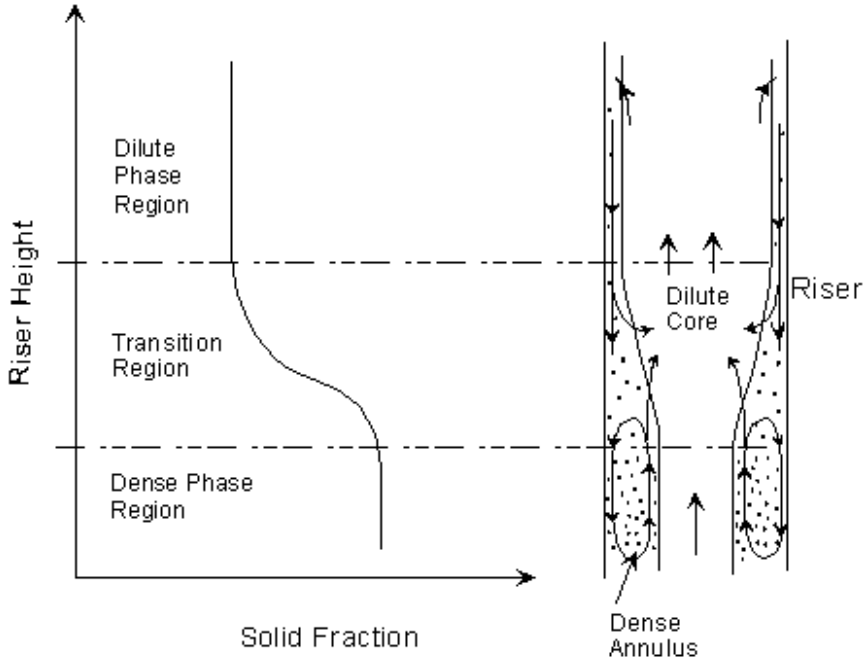

Figure 5.2.1 Transition Region of Riser

In Figure 5.2.2 to 5.2.4, the true solid fractions from x-ray measurements and the apparent solid fractions between each pair of pressure probes are plotted for the three runs. Again, the curve fit of the points of the ΔP measurements (at the centers of the tap spacing) has the same area underneath as that of a bar graph of the point values. The pressure tap arrangement only permits the evaluation of three average apparent solid

fractions between the elevations of -0.3m and +0.9m. These sections are x = -0.3 to +0.1, 0.1 to 0.4 and 0.4 to 0.9 m. Because the X-ray data are only available from x=0.01 to 0.61m in the mixing region, the comparison can only quantitatively be made between the true solid fraction and the apparent solid fraction in the middle 0.1 to 0.4m section. However, both the lower and upper section comparisons provide additional insight.

It can be seen that the apparent solid fraction is lower than the true solid fraction over the elevations between 0 and 0.6m when the inner to outer velocity ratio λ, is 0.7 (Figure 5.2.2). When the ratio λ is equal to or larger than 1 (Figure 5.2.3 and 5.2.4), the apparent solid fraction is higher than the true solid fraction. According to the one-dimensional momentum equation described above, net cross-sectional average acceleration of solids occurs in this section when $\lambda \geq 1$, while cross-sectional average deceleration of solid takes place when $\lambda = 0.7$.

A close look at the true solid fraction profile shows, however, that the true solid fraction decreases over the interval x=0.01 to 0.61m for $\lambda \leq 1$ cases, but increases for the $\lambda = 3$ case. The cross-sectional average solid fraction decreases with cross-sectional average acceleration for the $\lambda = 1$ case as is

expected for a typical riser flow. However, the cross-sectional average solid fraction decreases with cross-sectional average deceleration in the low velocity ratio case of λ=0.7, and the cross-sectional average solid fraction increases with cross-sectional average acceleration in the high velocity ratio case of λ=3. As mentioned above, these disagreements which are signs of strong radial gradient can only be explained with at least a multistepped pluglike riser flow, indicating that a strong flow pattern readjustment or recirculation pattern is taking place.

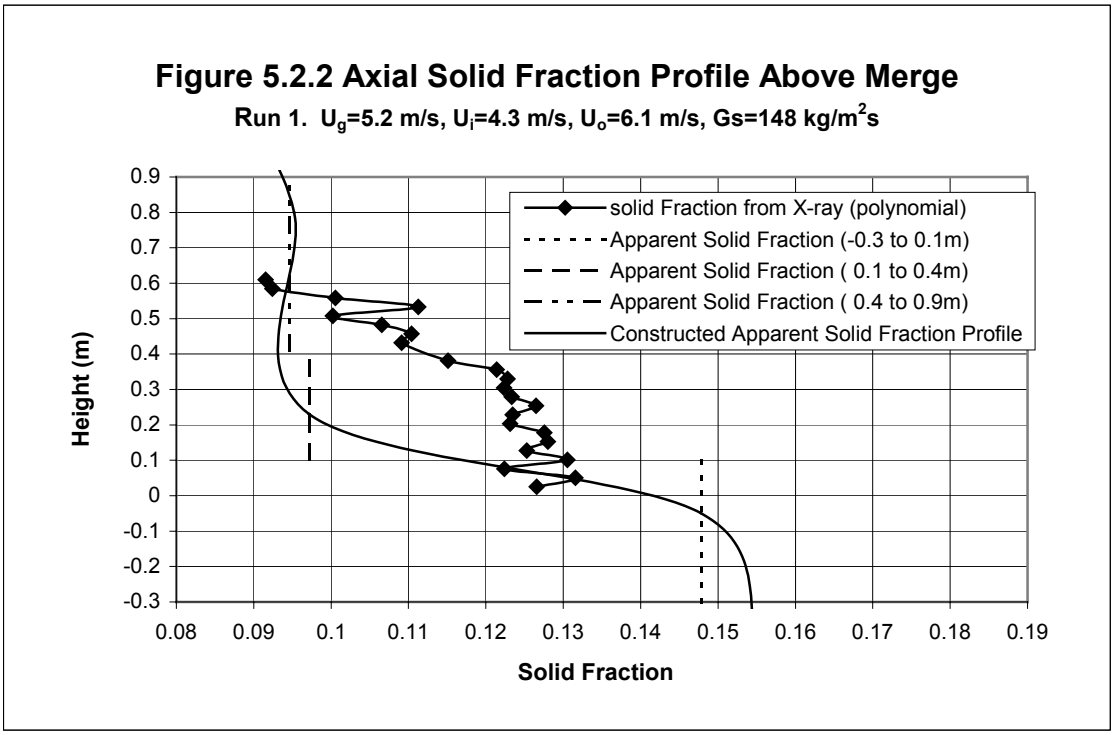

Figure 5.2.3 Axial Solid Fraction Profile Above Merge

Run 2. U_g=5.2m/s, U_i=5.4m/s, U_o=5.4m/s, Gs=142kg/m^{2}s

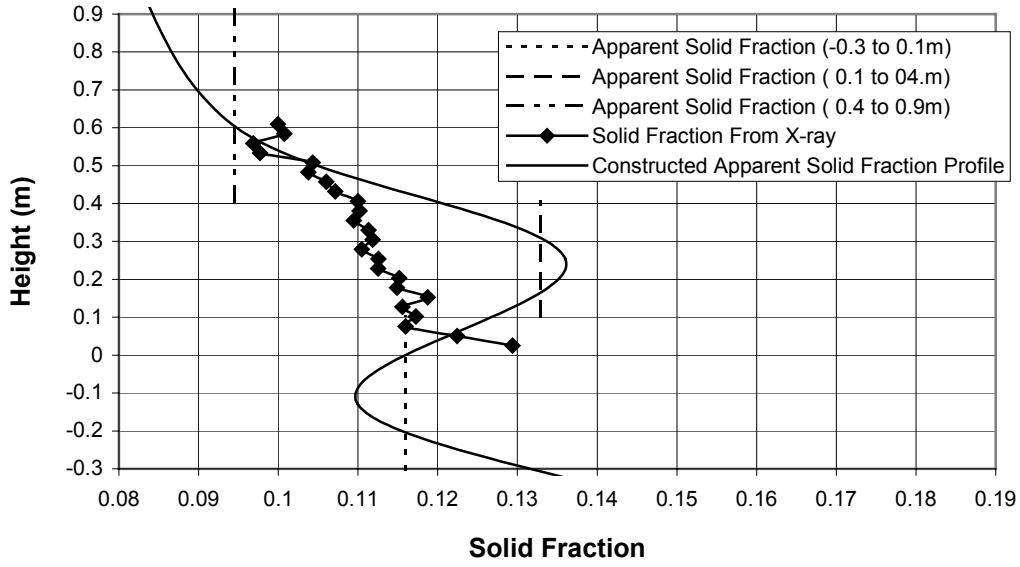

Figure 5.2.4 Axial Solid Fraction Profile Above Merge

Run 3. U_g=5.2m/s, U_i=9.5m/s, U_o=3.2m/s, Gs=151kg/m^{2}s

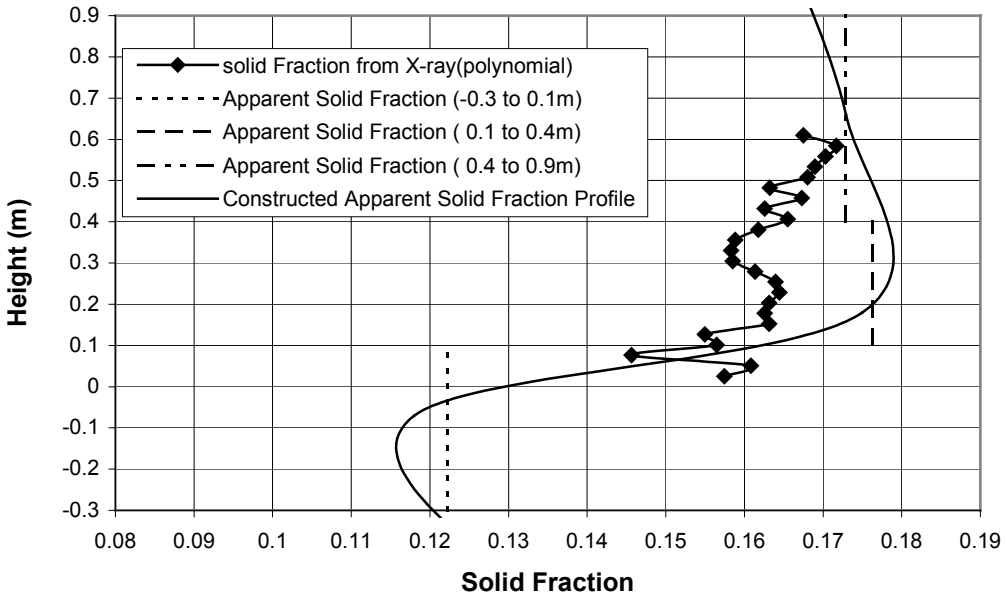

No methods are available to provide a detailed visual observation or the local properties of the gas-solid two-phase flow inside a high-density fluidized bed. The X-ray measurements can provide the time-averaged solid fraction but not much information about solid recirculation patterns. Although there is no literature reported on the subject to date, it is reasonable to expect that a recirculation pattern or a backflow vortex similar to that of single-phase coaxial flow could also be formed in the mixing region of gas-solid coaxial flowing streams. The two kinds of recirculation patterns that are found in homogeneous coaxial flows are illustrated in Figure 5.2.5. In Figure 5.2.5a, for a velocity ratio $\lambda < 1$, a wake vortex or "bubble" in the mouth of the inner tube can be formed by the outer stream entraining the issuing inner flow causing its "streamlines" to bend outward from the axis. As seen in Figure 5.2.5c, when the inner stream velocity is much higher than the outer stream velocity the outer stream is entrained, bending its "streamlines" inward toward the axis, and a recirculation region can be formed near the outer wall well above the end of the inner tube. The existence as well as the position of the recirculation region depends on both the velocity ratio and the diameter ratio of inner and outer tubes. The recirculation cell that develops for $\lambda<1$ cases is usually very close above the

mouth of the inner tube, while the recirculation region in the λ>1 cases is usually at a higher elevation and pressed against the outside wall, as described in Figure 5.2.5. It can be seen in the following sections that these flow structure assumptions explain the pressure measurement results and are in good agreement with the other measurement results as well.

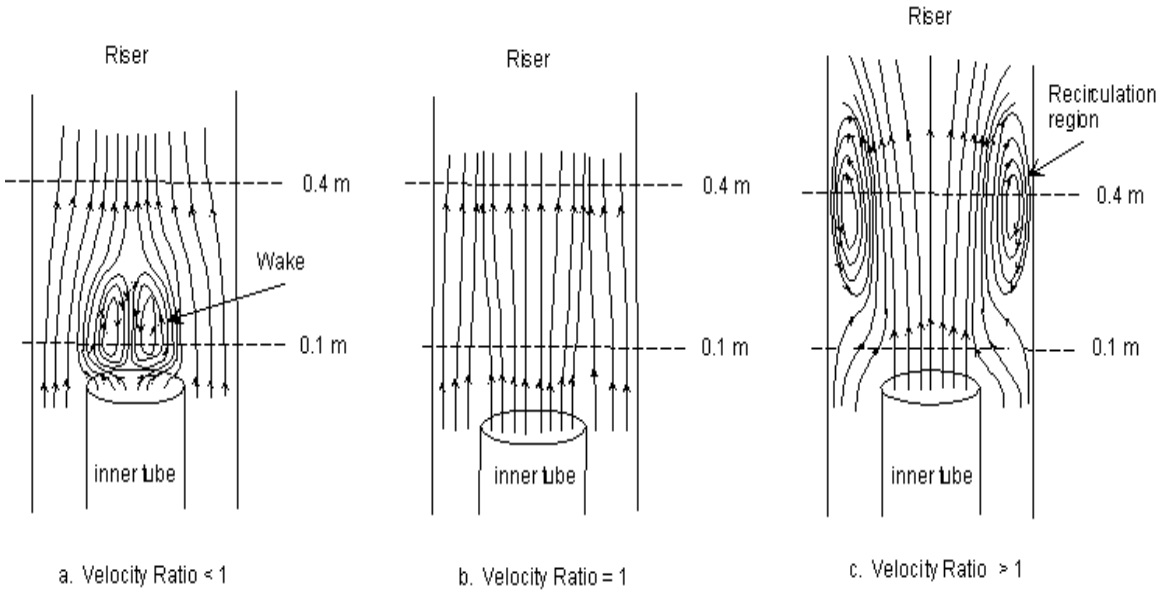

Figure 5.2.5 Recirculation Patterns of Coaxial Flowing Gas-solid Streams

Illustrations based on a multistep profile in the one-dimensional momentum equation help to explain how the acceleration term and the solid holdup term interact to provide these phenomena. For demonstration purposes, the flow structures for the λ<1 and the λ>1 cases are simplified, as shown in Figure

5.2.6. The solids are assumed just circulating inside the recirculation region and the net solid velocity U_3 is simply set to zero. Uniform solid fractions and plug flow velocity profiles are assumed in each region or step. Therefore, the mean value $\overline{(1-\varepsilon)U_s}$ equals to $(1-\varepsilon)U_s$ in each region.

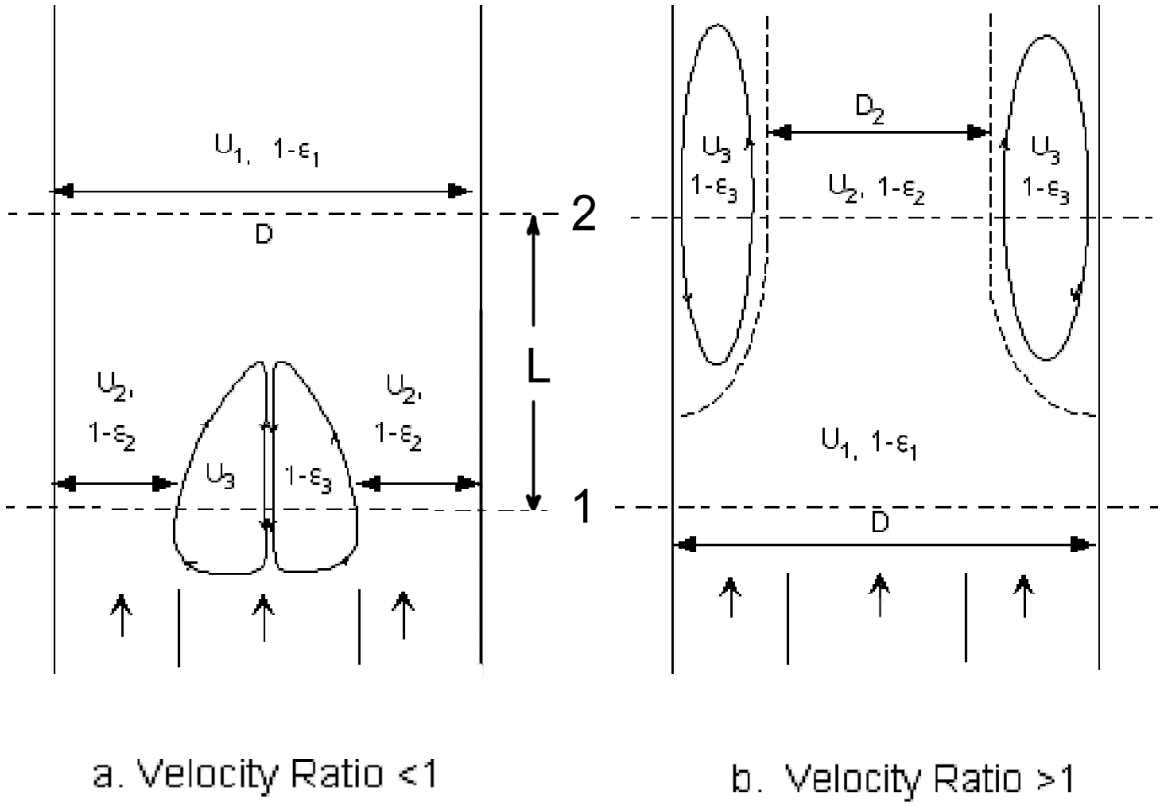

Figure 5.2.6 One-dimensional Model for Riser Flow with Recirculation Region

For both cases, the total one-dimensional solid continuity equation gives

$$\rho_s(1-\varepsilon_1)U_1A_1 = \rho_s(1-\varepsilon_2)U_2A_2 + \rho_s(1-\varepsilon_3)U_3A_3 \qquad (5.2.11)$$

Where $U_3 = 0$, $A_1 = \pi D^2/4$, $A_2 = \pi(D^2 - D_3^2)/4$ when $\lambda<1$ and $A_2 = \pi D_2^2/4$ when $\lambda>1$.

When $\alpha_1 = 1-\varepsilon_1$, $\alpha_2 = 1-\varepsilon_2$, $\xi = A_2/A_1$, equation (5.2.11) can written as

$$\alpha_1 U_1 = \alpha_2 U_2 \xi \qquad (5.2.12)$$

For the case with a velocity ratio of less than 1, as shown in Figure 5.2.6a, the solid acceleration term in the right-hand side of equation (5.2.6) becomes

$$\frac{\Delta\left[\rho_s\overline{(1-\varepsilon_{true})U_s^2)}\right]}{L} = \frac{\rho_s\alpha_1U_1^2 - \rho_s\alpha_2U_2^2\xi}{L} = \frac{\rho_s\alpha_1U_1^2}{L}(1-\frac{\alpha_1}{\alpha_2\xi}) \qquad (5.2.13)$$

If $\alpha_2\xi + (1-\xi)\alpha_3 > \alpha_1 > \alpha_2\xi$, solid deceleration can take place, with the cross-sectional average solid fraction decreasing. This can explain the results of the λ=0.7 case.

For the case with a velocity ratio greater than 1, shown in Figure 5.2.6b, the solid acceleration term in the right-hand side of equation (5.2.6) becomes

$$\frac{\Delta\left[\rho_s\overline{(1-\varepsilon_{true})U_s^2)}\right]}{L}=\frac{\rho_s\alpha_2U_2^2\xi-\rho_s\alpha_1U_1^2}{L}=\frac{\rho_s\alpha_2U_2^2\xi}{L}(1-\frac{\alpha_2\xi}{\alpha_1}) \quad (5.2.14)$$

If $\alpha_2\xi+(1-\xi)\alpha_3>\alpha_1>\alpha_2\xi$, solid acceleration can take place, with the cross-sectional average solid fraction increasing. This is an explanation of the results of the λ=3 case.

If the bulk gas and solid flow direction in Figure 5.2.6b is reversed, the flow structure is similar to that of the transition region of a typical riser. When $\alpha_1=\alpha_2\xi$, the apparent solid fraction equals the true solid fraction while solid holdup is decreasing with height, explaining what happens in the transition region of a typical riser, as show in Figure 5.2.1.

5.3 Pressure Profiles at the Centerline and the Wall of the Riser

A pressure probe, as shown in Figure 5.3.1, was designed to measure the axial pressure profiles just above the top of the inner tube. The probe consists of four stainless steel tubes with I.D. of 3mm and O.D. of 5mm, that simultaneously give four pressure readings at different elevations all relative

to a reference probe placed at the wall. Figure 5.3.2 to 5.3.4 shows the reference pressures measured at the centerline and wall using this pressure probe. The dotted lines in these figures are drawn using the pressure gradient calculated from the axial pressure profiles in Figure 5.1.1 and fixed to the wall pressure reading at the 0m elevation.

In Figure 5.3.2 for λ=0.7, the centerline pressure increases somewhat downstream, reaches a peak, then decreases. At 0.076m, the centerline pressure is even higher than the wall pressure. This is in keeping with a backflow vortex existing near the top of inner tube with its axial stagnation points. The pressure rise at 0.025m may be associated with the front stagnation point of the vortex. The wall pressure also increases downstream right after the merge of the two streams. It reaches a peak at about 0.05m elevation, then decreases approaching the axial pressure profile or dotted line. The pressure increase is due to the slowing down of solid phase near the wall right after merge, as is pictured in Figure 5.2.5a.

In Figure 5.3.3, the centerline pressure for λ=1 also increases downstream, but it always is considerably lower than the wall pressure and maintaining a difference in value typical of riser flow at this solid fraction. This pressure

profile suggests that there may be also some slowing of the outer and inner flows just above the inner tube because of momentum transfer to solids coming off the influence of the inner tube wall. These deviations from the dotted line are not as significant as they are for the λ=0.7 case. The wall pressure also increases for the same reason as in λ=0.7 case.

For the case of λ=3, both the centerline and the wall pressure continuously decrease downstream from 0 to 0.076m. These pressure profiles indicate that there is no recirculation in this region. Both pressures go down about as fast as the dotted line. This is in keeping with acceleration prior to a necking down insider a recirculation vortex pressed to the outside wall above 0.076m.

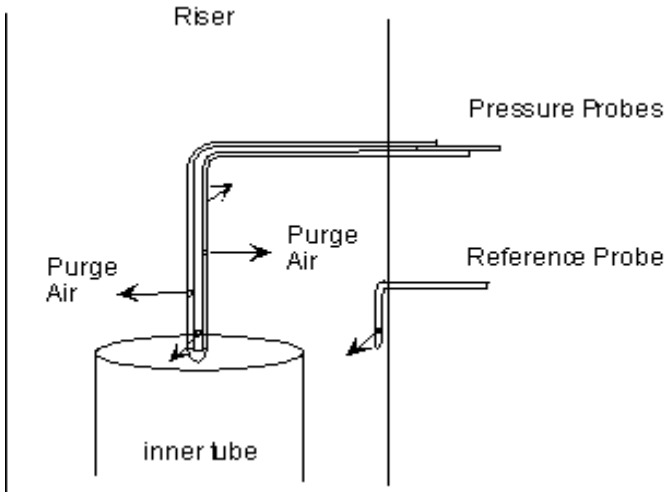

Figure 5.3.1 Pressure Measurement Setup

Figure 5.3.2 Axial Pressure Profile Above Merge

Run 1. Ug=5.2m/s, U_i =4.3m/s, U_o= 6.1m/s, Gs=147kg/m^2s

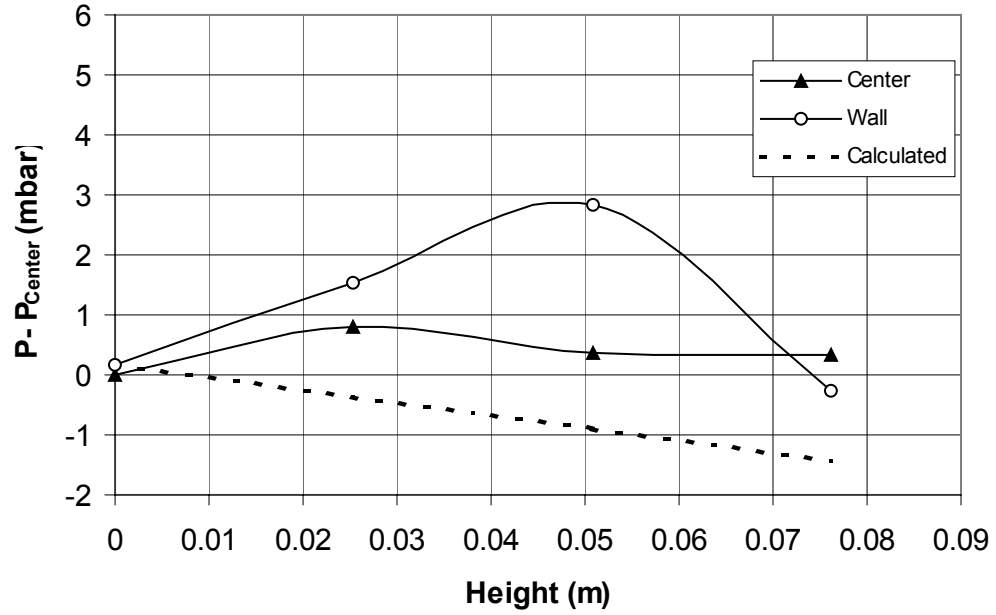

Figure 5.3.3 Axial Pressure Profile Above Merge

Run 2. Ug=5.2m/s, U_i =5.4m/s, U_o=5.4m/s, Gs=142kg/m^2s

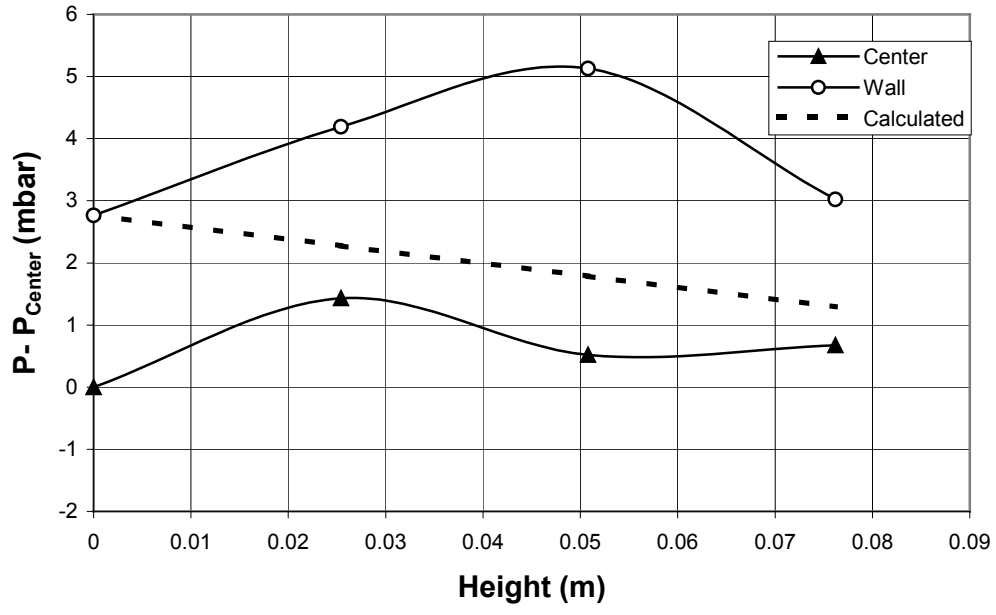

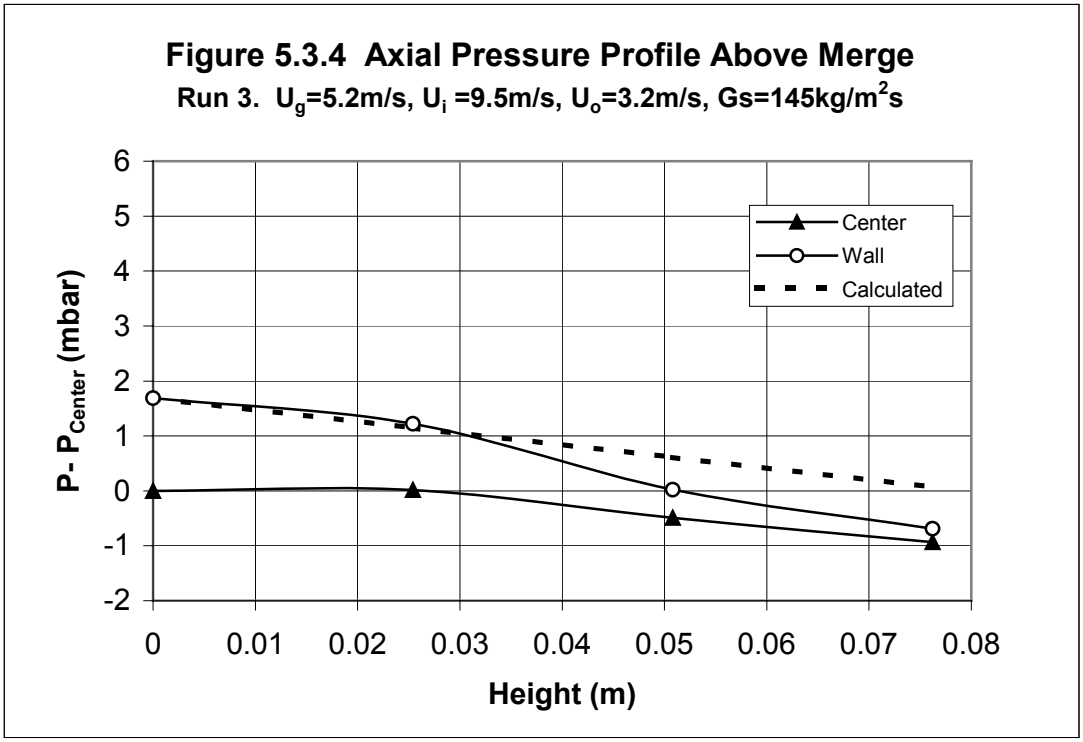

5.4 Radial Pressure Profiles

In most descriptions of riser flow, the radial pressure variation is usually ignored and the pressure measured at the wall is used to represent the axial pressure over the entire cross-section of riser. However, measurements of the radial pressure gradient have shown that in typical riser flow, a wall to centerline pressure gradient exists and it is of the same order of magnitude as the axial pressure gradient (Weinstein et al. 1995). In this study of coaxial flow, deviations in the radial pressure profile from a typical riser profile gives insight into the flow structure and characteristics. Radial pressure

profiles at two elevations above the merge are measured in this investigation for the cases of λ=0.7, 1 and 3, respectively.

In the typical riser flow, there are upward and downward solid fluxes in the axial direction, and inward and outward solid fluxes in the radial direction. The radial pressure gradient supports the core-annular flow structure. The magnitude of the mean radial pressure gradient from wall to axis is about the same order as the axial pressure gradient at the same elevation. Weinstein et al. (1995) examined the radial pressure difference in a typical riser of the same diameter as the riser used in this study. They used two different probe designs to demonstrate that the probe design did not cause the pressure difference. Typical results are presented in Figure 5.4.1. The wall to centerline pressure difference is about 2 mbar H_2O at a solid fraction of 0.20. They also showed that the pressure difference is directly proportional to the solid fraction.

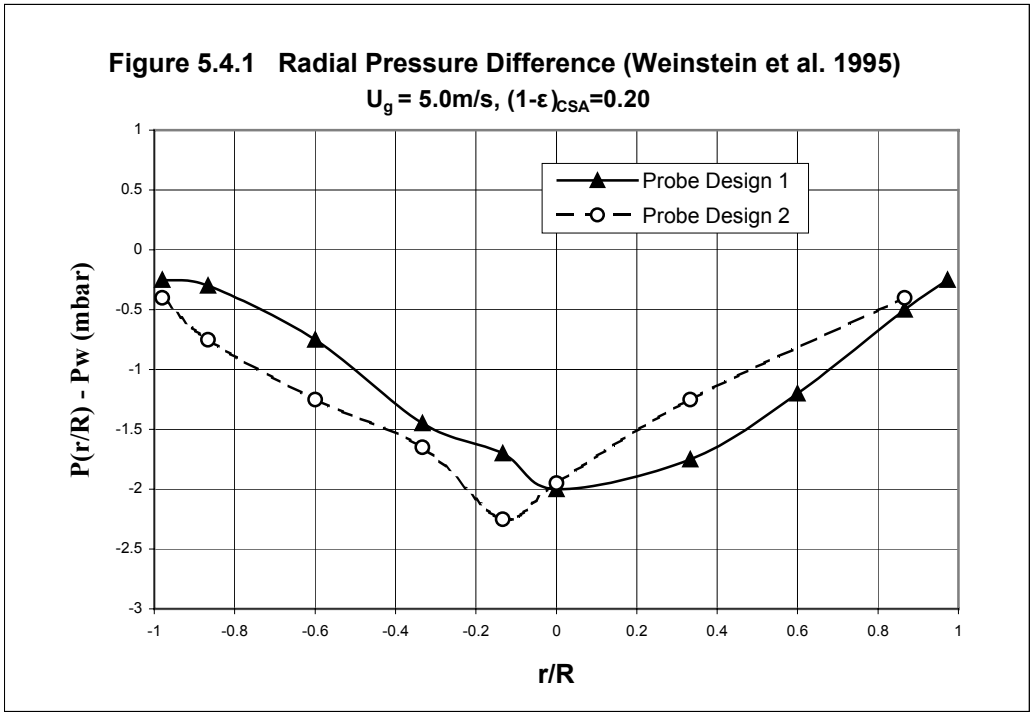

The radial pressure profile for the case of λ=0.7 is shown in Figure 5.4.2. A peak of static pressure at about r/R=0.6 can be observed compared to the radial pressure profile of a typical riser presented in Figure 5.4.1. This is probably due to the wake-type mixing of two streams. The curvature outward of the streamlines in the near wake leads to a peaking of local static pressure. This profile also verifies the flow structure mentioned earlier for this case.

Figure 5.4.3 shows that the radial pressure profile for λ=1 case has a near parabolic shape, closer to the typical riser profile as shown in Figure 5.4.1.

In the core region (r/R<0.3), the pressure goes down faster towards the center, corresponding to the dilute core where solid concentration is very low as shown in the radial solid fraction profiles. It appears to be due to the result of acceleration of the wake right after the merge.

For the case of λ=3, in Figure 5.4.4, there is also a peak (at r/R=0.7~0.8) resulted from the curvature effect of the streamlines but much lower and flatter than λ=0.7 case. The radial pressure difference for λ=3 case is smaller than that of the other two cases, consistent with the data from the axial pressure probe plotted in Figure 5.3.4. This is in keeping with the high centerline velocity and the outward bending streamlines from the center tube.

It can be seen that the radial pressure profiles become flatter and smoother at higher elevation for all three test cases. This reflects the readjustment of the coaxial flow towards typical riser flow. This is also seen in the solid fraction profiles. For the case of λ=3, the radial pressure profile at 0.38m is still flatter and far from that of typical riser flow. This is also consistent with the solid radial fraction profiles.

Figure 5.4.2 Radial Pressure Distribution Above Merge

Run 1. U_g=5.2m/s, U_i=4.3m/s, U_o=6.1m/s, Gs=147kg/m^{2}s

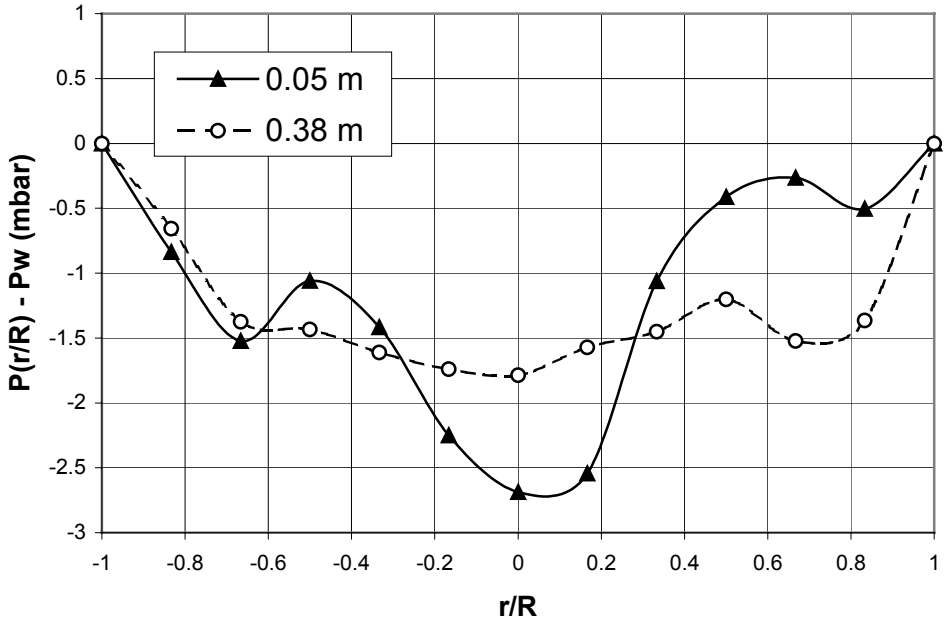

Figure 5.4.3 Radial Pressure Distribution Above Merge

Run 2. U_g=5.2m/s, U_i=5.4m/s, U_o=5.4m/s, Gs=142kg/m^{2}s

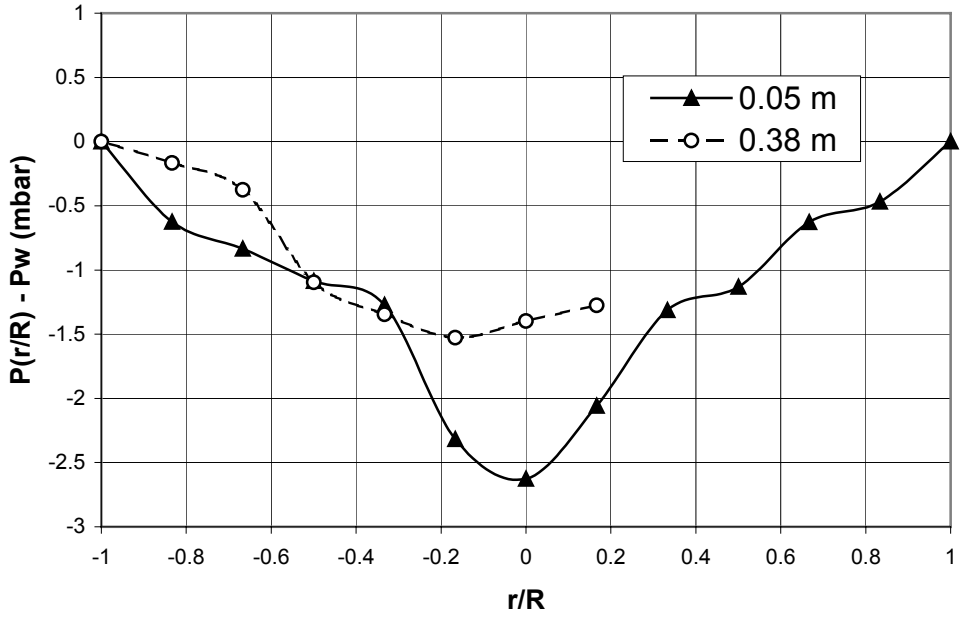

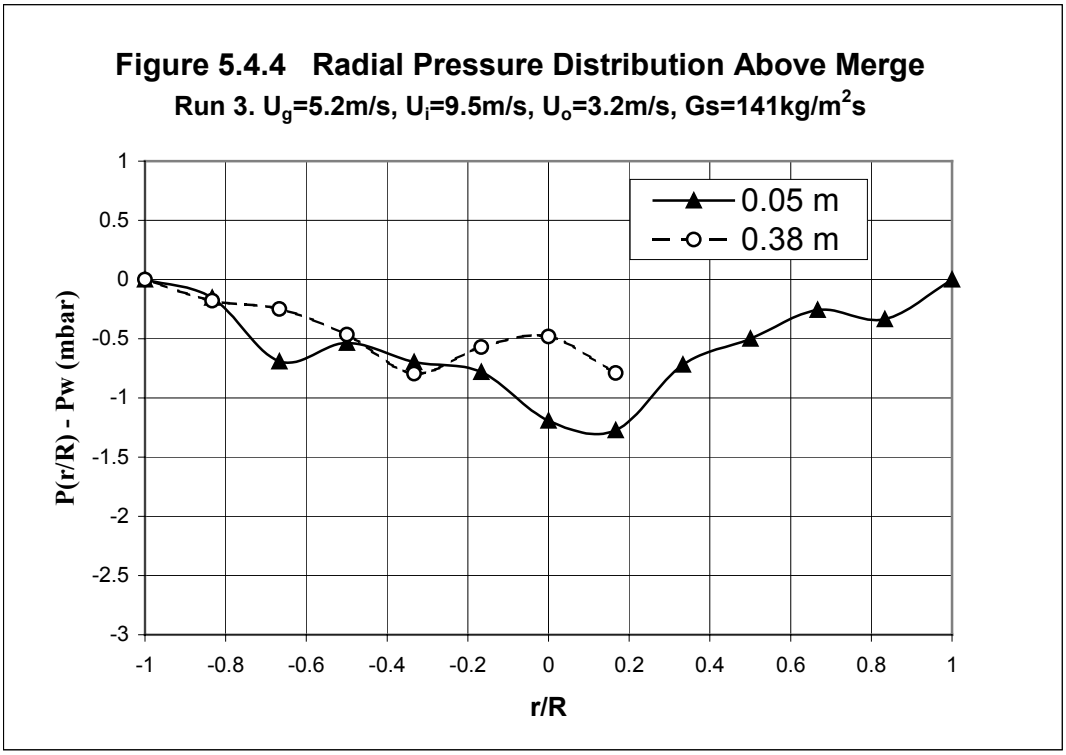

5.5. Radial Solid Distribution

The radial solid catalyst distribution has a large effect on the product distribution in a riser chemical reaction. In this investigation, the radial distributions of solid volume fraction across both the separated and the merged flows were measured by the X-ray technique as described in section 4.4.

The radial solid fraction profiles in the center tube and the annulus before the merge are shown in Figures 5.5.1 and 5.5.2 for λ=0.7 and 3, respectively. The solid distribution in the center tube is a typical core-annulus distribution with high solid fraction in the wall region and low solid fraction in the center. As expected, the radial solid profile decreases in magnitude without significant change in shape as the gas superficial velocity increases. Especially near the wall, the solid fraction is higher for the low inner tube gas velocity λ=0.7 case than that for the λ=3 case. The solid distribution across the annulus exhibits high values at both the inner and outer walls where the gas velocity goes to zero and a low value in between the walls where the gas velocity is high. This is the expected annular flow distribution although it has not, apparently, been previously reported in the literature. It is also worth noting that the solid holdup inside and outside the inner tube tends to be about the same due to the total effect of pressure balance.

The flow field of coaxial flowing streams is usually considered to be comprised of three regions: an initial mixing region and the main downstream fully-merged (or fully-developed in homogeneous flows) region with a transition region in between. Our focus is on the initial mixing and

Figure 5.5.1. Radial Catalyst Fraction Profile Below Merge

Run 1. U_g=5.2m/s, U_i=4.3m/s, U_o=6.1m/s, G_s= 148kg/m^{2}s, at -0.3m

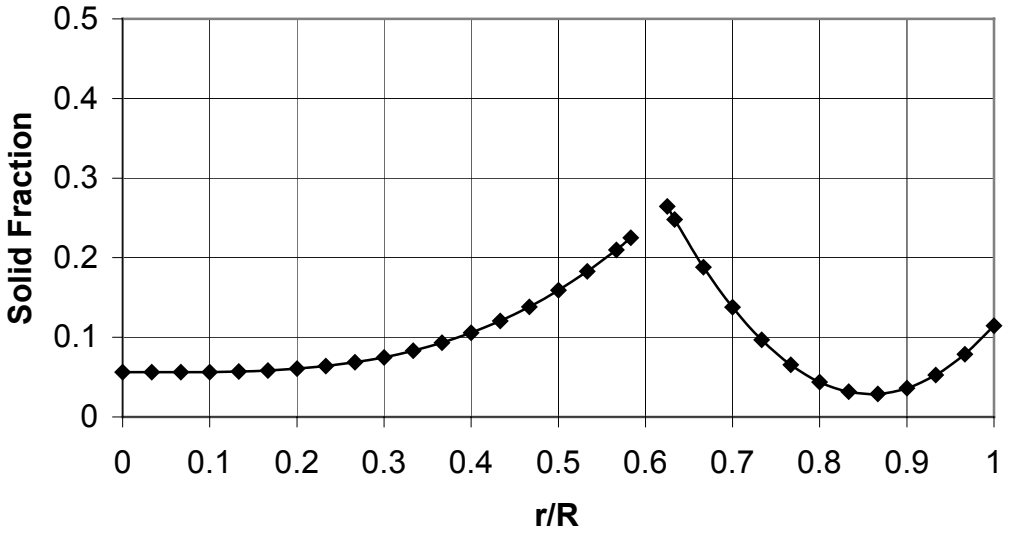

Figure 5.5.2 Radial Solid Fraction Profile Below Merge

Run 3. U_g=5.2m/s, U_i=9.5m/s, U_o=3.2m/s, G_s= 148kg/m^{2}s, at -0.3m

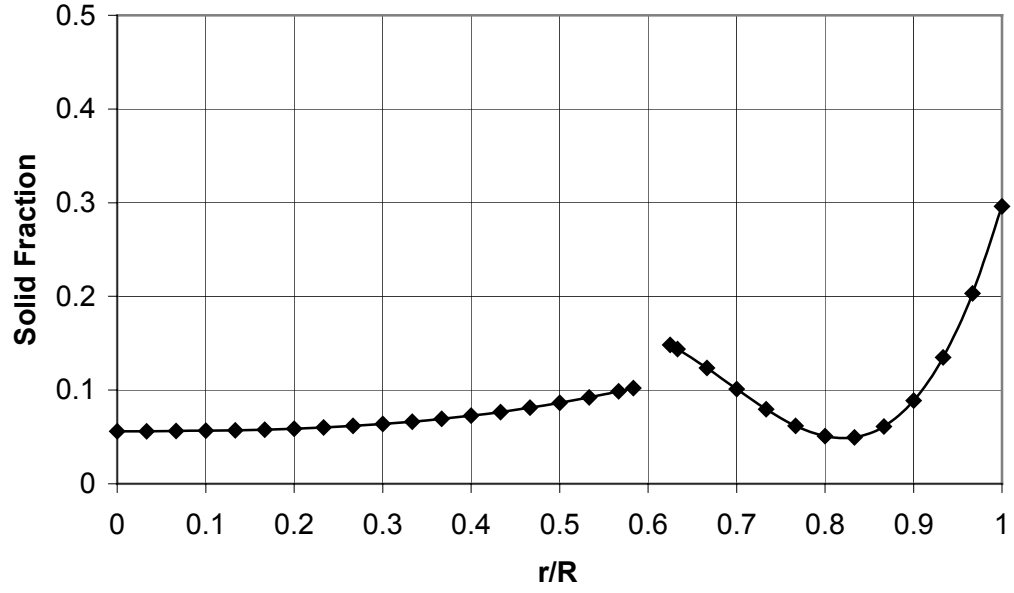

transition regions where the center and the annular streams begin to merge and interact with each other, and therefore develop very complex flow patterns. Several X-ray measurements were taken at different elevations, from 0m to 0.61m (0 to 4 L/D_{outter} or 7 L/D_{inner}) above the merge.

Figures 5.5.3 to 5.5.5 are three-dimensional pictures of the radial solid fraction profiles for three values of inner to outer gas superficial velocity ratios, λ=0.7, 1 and 3, respectively. The total circulation rate could not be held exactly the same for every run. It was controlled in a narrow range from 142 to 151kg/m^{2}s. The general core-annulus structure of riser flow with a dense annular region close to the wall and a dilute core region in the center is observed in all three cases. The solid concentration profile in the dilute core, however, is not as uniform as it is in regular riser flow. It can be seen that there is an even more dilute sub core ($r/R<0.3$) within the ordinary dilute core for all three cases. In the initial mixing region of the confined coaxial flowing gas-solid streams in riser, the flow structure can be described as a dense annular region with high solid fraction gradient, a dilute core with relatively uniform solid fraction and a sub core in the center with a lower solid fraction gradient. The mechanism of the formation of the sub

core is not very clear at this point. It could be the extension of the dilute core of the inner tube, the result of acceleration of the inner stream, or both.

When the outer stream velocity is the higher, i.e. the λ=0.7 case in Figure 5.5.3, the solid fraction in the annular region decreases slightly with height just above the merge and starts to fall off more rapidly at about 0.4m. This indicates that a flow transition is taking place in this region, in agreement with the results from pressure measurements as shown in Figure 5.4.2.

For the equal velocity case (λ=1), the solid fraction in the annular region continuously decreases with height as shown in Figure 5.5.4. This profile indicates a smooth merge of two streams, consistent with the axial pressure profile as shown in Figure 5.1.1.

For the λ=3 case, the solid fraction in the wall region increases with height. This is due to the recirculation pattern developed near the wall region, as previously pictured in Figure 5.2.5.

Figure 5.5.3 Solid Fraction Profile Above Merge

Run 1. U_g=5.2 m/s, U_i=4.3 m/s, U_o=6.1 m/s, Gs=148 kg/m^{2}s

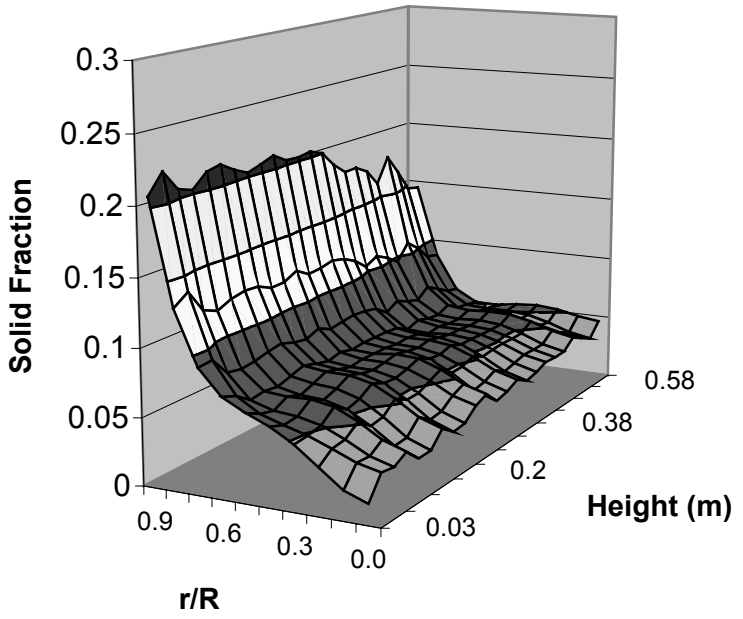

Figure 5.5.4 Solid Fraction Profile Above Merge

Run 2. U_g=5.2 m/s, U_i=5.4 m/s, U_o=5.4 m/s, Gs=142 kg/m^{2}s

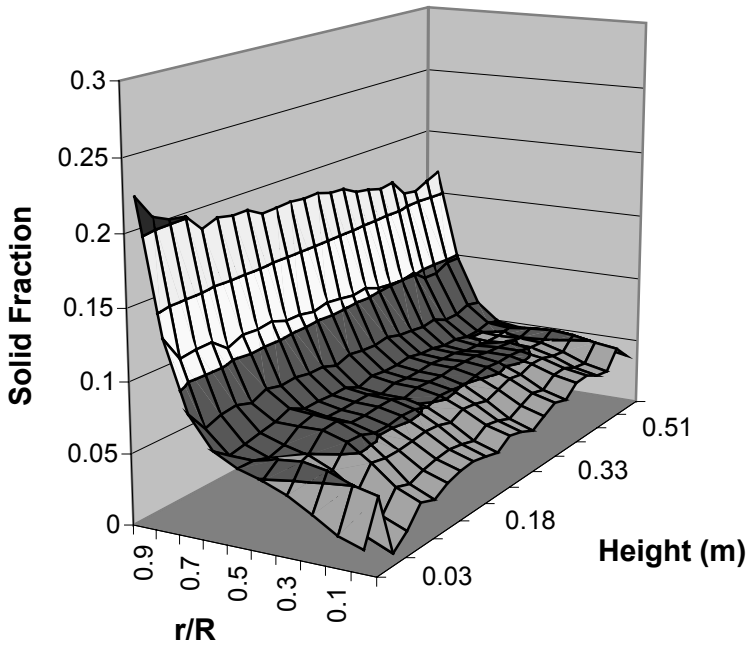

Figure 5.5.5 Solid Fraction Profile Above Merge

Run 3. U_g=5.2 m/s, U_i=9.5 m/s, U_o=3.2 m/s, Gs=151 kg/m^{2}s

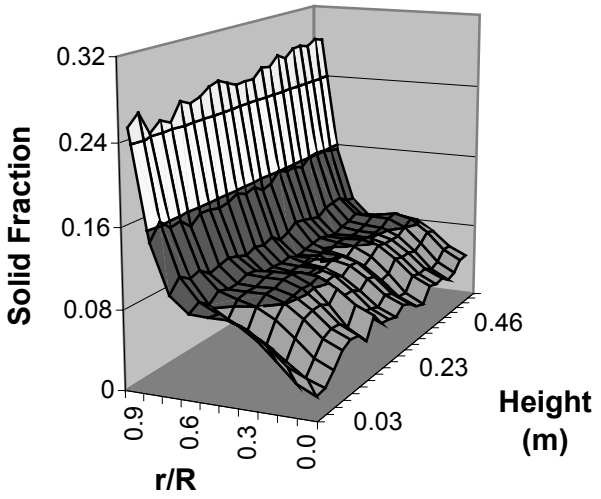

Figures 5.5.6 to 5.5.8 show the radial solid fraction profiles at three locations, H=0.1, 0.4 and 0.61m for the three runs, λ=0.7, 1 and 3, respectively. From these figures, it can be seen that for all three cases, the solid fraction is greater than 20% close to wall and falls quickly to the 6% to 8% range at about r/R=0.6~0.7. This is similar to the solid distribution of a typical riser (Kostazos, 1997). For all three cases, a dilute sub core (0≤ r/R <0.3) can be clearly distinguished inside the regular dilute core region. In this region, solid fraction decreases gradually towards the centerline. The radial solid fraction gradient increases with increasing the value of the velocity ratio, λ.

For the cases where $\lambda \leq 1$, i.e. for $\lambda=0.7$ and 1, in Figure 5.5.6 and 5.5.7, the solid fractions near the wall are about 21% at 0.1m and decrease with height from 0.1 to 0.61m. The solid fraction in the dilute core ($0.3<r/R<0.7$) also decreases but very slightly. The solid fraction in the dilute sub core, however, increases and flattens with height, and gradually approaches the solid fraction value in the dilute core. In both cases, the profile shape changes considerably in the initial mixing region as flow readjusts. Above 0.61m, the dilute sub core has completely merged into the ordinary dilute core and the solid fraction profile approaches closely to a typical riser profile shape with a uniform dilute core and a dense annular region close to the wall for both of these cases. These solid fraction profiles indicate a relatively smooth merge of the two streams, which is consistent with the smooth axial pressure profiles for these two runs in Figure 5.1.1.

For the case when $\lambda=3$, Figure 5.5.8, the solid fraction is about 26% near wall at 0.1m, much higher than that of other two cases. The solid fraction near the wall increases slightly with height instead of decreasing as was observed for the $\lambda \leq 1$cases. This is due to the recirculation pattern formed in this region near the wall, as shown in Figure 5.2.5. The solid fraction gradient in the dense annular region also increases with height. In the dilute

core region, the solid fraction magnitude also does not change significantly. The dilute core expands in diameter to the wall as moving higher. The solid fraction in the dilute sub core also increases with height, but much more slowly than in other two cases. The dilute sub core shrinks to $0 \leq r/R < 0.3$ from $0 \leq r/R < 0.4$ but still is evident at 0.61m elevation. Unlike the other cases, the flow for the $\lambda=3$ case is still far from a typical riser flow at this elevation. This behavior is also clear from the increase in the slope of the axial pressure profile for this case in Figure 5.1.1.

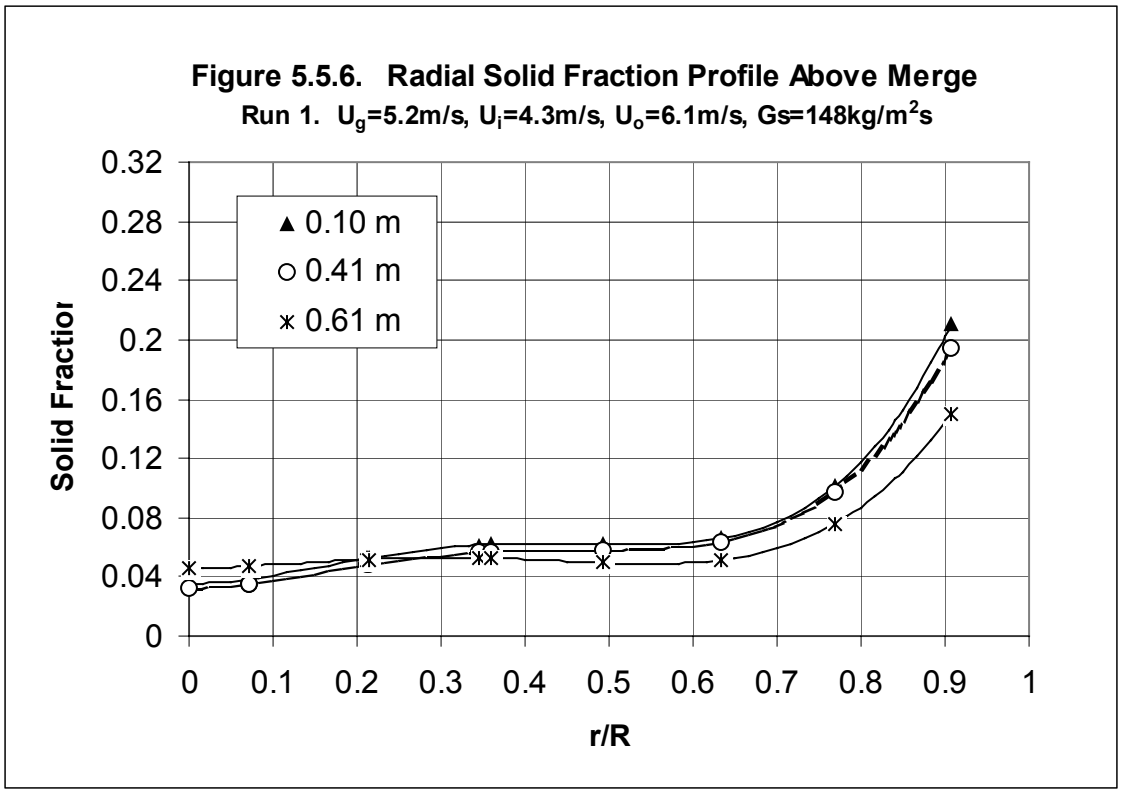

Figure 5.5.7 Radial Catalyst Fraction Profile Above Merge

Run 2. U_g=5.2m/s, U_i=5.4m/s, U_0=5.4m/s, Gs=142kg/m^{2}s

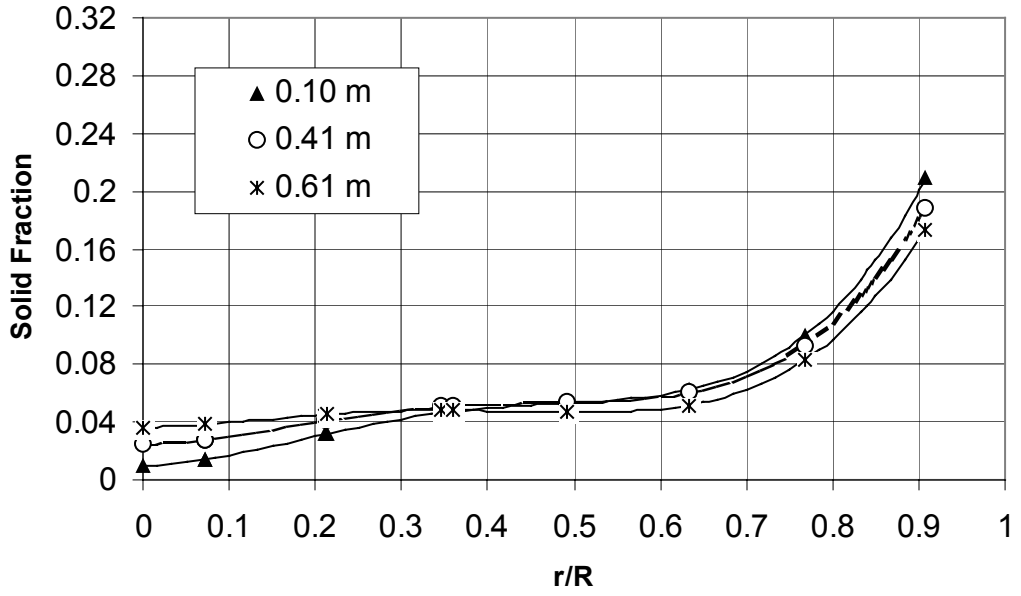

Figure 5.5.8 Radial Solid Fraction Profile Above Merge

Run 3. U_g=5.2m/s, U_i=9.5m/s, U_0=3.2m/s, Gs=151kg/m^{2}s

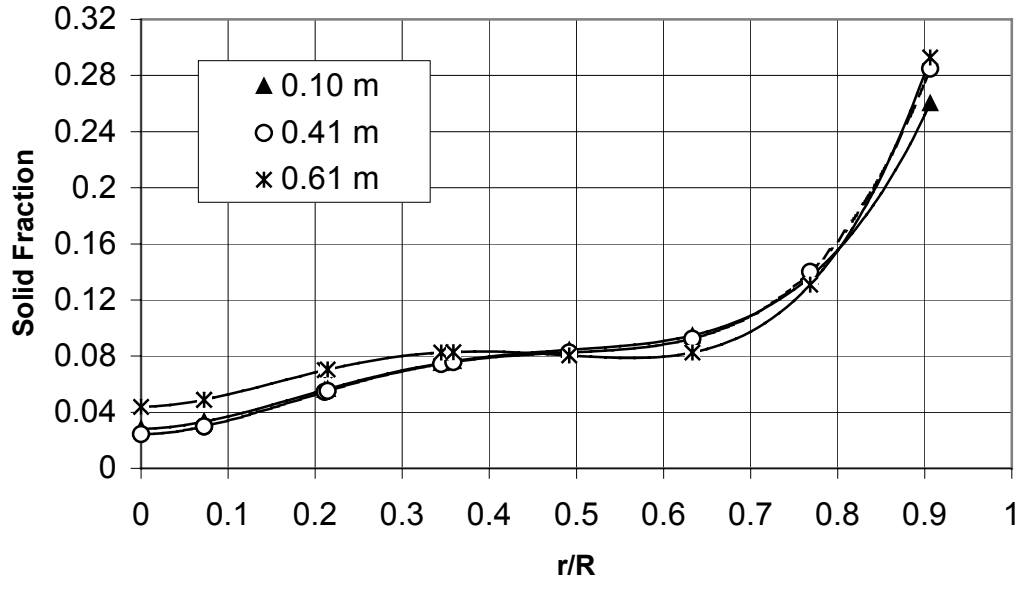

5.6. Axial Solid Flux Profile

The radial distribution of the axial solid flux also helps in describing the solid flow structure in riser. It, combined with the solid fraction data, can be used to estimate the axial solid velocity profiles. The axial solid flux at two elevations, one just above the merge and one at a higher elevation, are measured using the flux probe described in section 4.3.

To check the accuracy of flux probe measurements, the cross-section average solid flux calculated by integrating the local solid flux probe readings over the cross-sectional area is compared with the total solid circulation rate measured by the butterfly valve technique as described in section 4.3. It should be pointed out that the value of the independently measured solid circulation rate is slightly lower than the true value because it does not include the solids returned from the secondary cyclone. This comparison for all three cases is shown in Table 5.6.1.

The results for the case of $\lambda=1$ give the closest value to total solid circulation rate. In this case, the values at 0.1m and 0.41m are essentially the same, satisfying the continuity of solids flow. The difference between the two

cross-sectional average values and the butterfly valve reading is about same as the results of Kostazos (1997) for regular riser flow. The values for λ=0.7 and 3, however, are much higher than that of independently measured solid circulation rate and are not about the same value at the two elevations. When solid recirculation patterns develop, the probe measurement tends to give a higher flux value because it sucks in some solids that are just circulating slowly in the backflow region. The much higher solid flux values measured at 0.10m for λ=0.7 and at 0.41m for λ=3 indicate that recirculation pattern is close to the end of center tube for λ=0.7 and at a higher elevation for λ=3. This again confirms the flow structures represented in Figure 5.2.5.

Table 5.6.1. Comparison of Solid Circulation Rate Measurements

Velocity Ratio / Gs (kg/m²s) / Measurements		λ=0.7	λ=1	λ=3
Butterfly Valve		151	142	142
Flux Probe	At 0.10 m	223	167	194
	At 0.41 m	178	171	220

The radial distribution of axial solid flux is shown in Figures 5.6.1 to 5.6.3, for the cases of λ=0.7, 1 and 3, respectively. It should be mentioned that the flux measurements can only give an approximate picture of the flux distribution due to the measurement errors in the recirculation region as mentioned above.

In Figure 5.6.1, the profile for the λ=0.7 case shows clearly the flux is deflected outward at the 0.1m elevation above the end of the inner tube. The axial solid flux peaks in the middle of the outer stream and falls off at about r/R=0.5 and at the outside wall. The solid flux profile is relatively low and flat over the section, radius r/R=0 to 0.35 region. From about r/R=0.35 to r/R=0.50, the flux decreases. The flux probe measurement gives a very high flux value because it sucks in solids just circulating in the central backflow region. It is obvious that the inner and outer streams are merged but are not spread across the central core region at this elevation. At 0.40m, the unusual central core behavior has disappeared and the two streams are fully merged. The solid flux profile at this elevation is approaching parabolic with a high value at the centerline and a very low usually negative value at the wall, the typical profile of riser flow. From 0.1m to 0.41m elevation, the measured axial solid flux decreases significantly and the cross-sectional average value

is down to about 20% greater than the butterfly valve value, as noted by Kostazos (1997). In the 1>r/R>0.6 region the solid flux decreases and it increases in the 0<r/R<0.6 region, indicating that solids are moving from the outer wall region to the central region. This movement must occur with streamlines bending toward the axis in this section, as shown in the flow structure predicted for this case, Figure 5.2.5.

The profile for the λ=1 case, as shown in Figure 5.6.2, is similar to that of the case of λ=0.7. The flux in the outer stream is lower than the outer stream of the λ=0.7 case due to a lower outer stream velocity. From the shape of the 0.41m profile, a close approach to the downstream or fully developed riser profile would probably take only a few additional diameters of riser length. The axial solid flux profile does not change much in the center from 0.1m to 0.4m. In this case, solids are mainly moving into the mixing layer from both directions above the inner tube wall, and the streamlines are bending slightly toward the mixing layer.

In Figure 5.6.3, the profile for the case of λ=3 does not show clearly the core of inner stream at 0.1m elevation. The profile has a maximum flux at about r/R=0.5. In this case, the inner stream velocity is very high and the outer

stream velocity is very low. The outer stream merges into the mixing layer very quickly downstream, and the streamline of the outer stream bends inside due to the strong entrainment of the outer stream by the inner stream. It can be seen that the axial solid flux increases significantly in the $0<r/R<0.35$ core region from the 0.1m to the 0.41m elevation. This indicates that solids are moving into the core region to meet the entrainment "demands" of the inner stream. The streamlines of the outer stream are bending inside and necking down inside a recirculation vortex pressed to the outside wall, as shown in Figure 5.2.5. Unlike other two cases, the solid flux near the wall is higher at 0.4m than at 0.1m. This is due to the recirculation zone formed at higher elevation near the wall. The solid flux profile at 0.41m shows considerable transition toward the fully developed flux profile but is still far from fully developed. This behavior is consistent with the pressure profiles and solid fraction profiles for this run which show an increasing pressure gradient and indicate a backmixing zone at 0.4m elevation.

Figure 5.6.1 local Solid Flux Profile

Run 1. U_g=5.2m/s, U_l=4.3m/s, U_o=6.1m/s, G_s = 151kg/m^{2}s

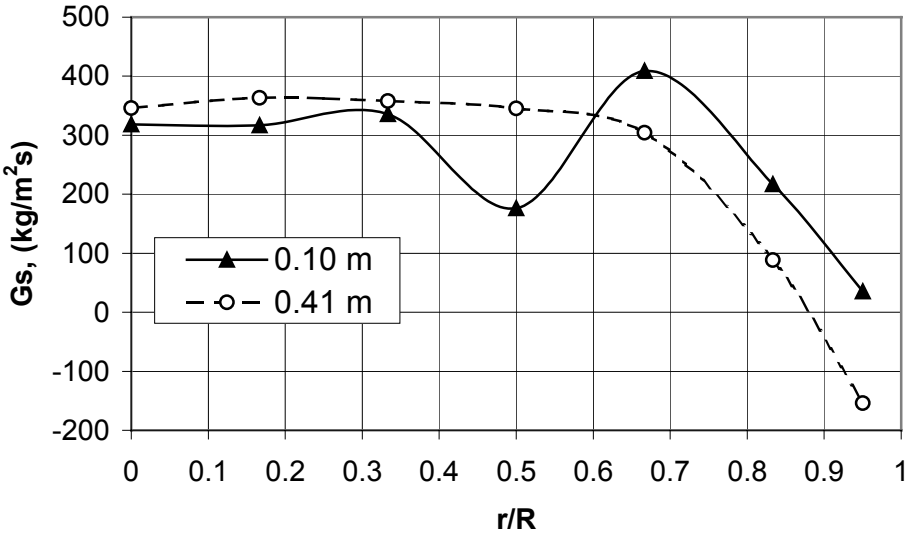

Figure 5.6.2 local Solid Flux Profile

Run 2. U_g=5.2 m/s, U_l=5.4 m/s, U_o=5.4 m/s, G_s = 142 kg/m^{2}s

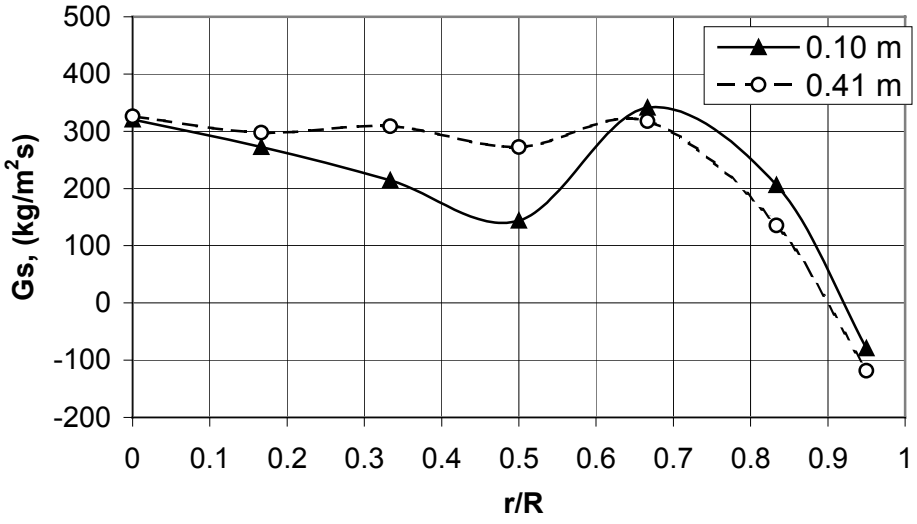

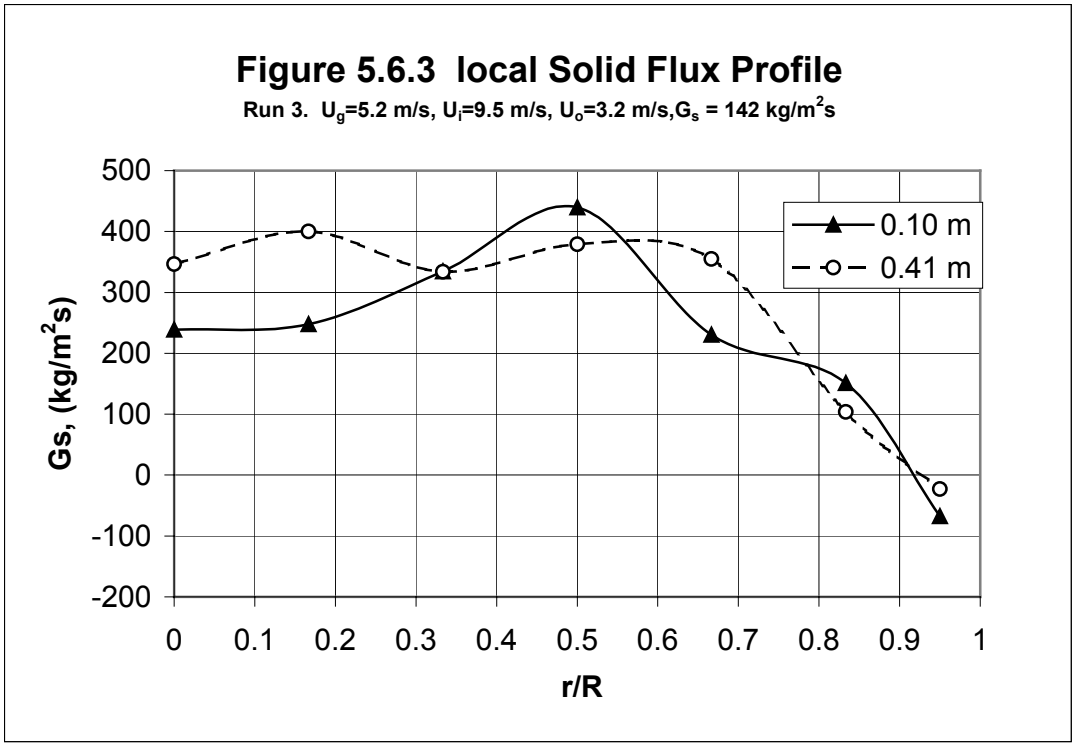

5.7 Gas Mixing

The mixing of gas between the two coaxial streams is studied with a tracer technique as described in section 4.5. The radial profiles of helium concentration at two locations are shown in Figure 5.7.1 to 5.7.3 for the λ=0.7, 1and 3 cases, respectively. The gas mixing rate may be estimated by comparing the location of the point, $y_{0.5}$, at which the helium concentration is half way between the centerline and the wall value. The further this point is towards the riser wall, the greater is the rate of mixing.

In Figure 5.7.1, when the outer gas velocity is higher, there is very little helium detected in $0.6<r/R<1$ region at 0.1m elevation. In this run, the location of the point $C/C_i=0.50$ is at about $r/R=0.33$ in 0.1m and 0.4m elevations. The gas mixing rate is low because there is a radial component of gas velocity inward in this case while the radial gas diffusion is outward. Since the centerline helium concentration decreases much more slowly from h=0.1m to 0.41m compared with the other two cases, the radial inflow of gas must dominate the turbulent diffusion.

For the $\lambda=1$ case also, as shown in Figure 5.7.2, the helium concentration detected in $0.7<r/R<1$ region at the 0.1m elevation is very low, but a considerably greater amount of helium is detected there at 0.41m. As expected, the location of $C/C_i=0.50$ is at about $r/R=0.38$, closer to the wall than in the $\lambda=0.7$ case. The centerline value is also lower at 0.41m in this case than in the previous case. In this case, gas mixing is mainly the result of the turbulent gas diffusion.

In Figure 5.7.3, for the case with the center gas velocity higher, there is a notable mount of helium detected in $0.6<r/R<1$ region even at the 0.1m

elevation. The location of C/C_i=0.50 point is at about r/R=0.43, closer to the wall than in the other two cases. The radial gas mixing rate is higher because both the turbulent gas diffusion and the radial velocity component are outward in this case. At 0.4m, the helium concentration profile actually turns upward at the wall. This is consistent with a recirculation formed in this region as shown in Figure 5.2.5.

Figure 5.7.1 Helium Concentration Profile

Run 1. U_g=5.2m/s, U_i=4.3m/s, U_o=6.1m/s, G_s = 151kg/m^{2}s

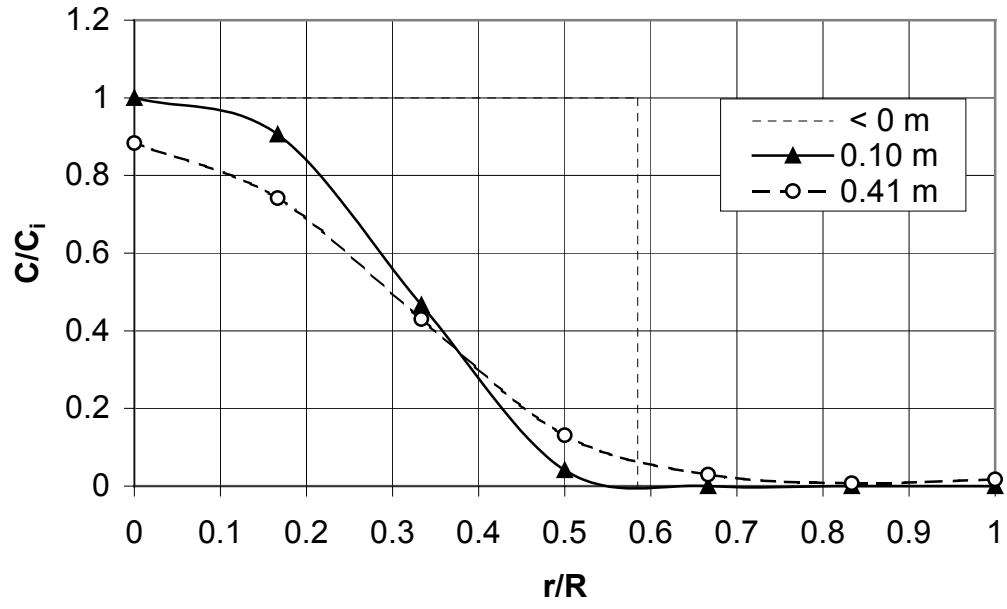

Figure 5.7.2 Helium Concentration Profile

Run 2. U_g=5. 2m/s, U_i=5.4 m/s, U_o=5.4 m/s, G_s=145 kg/m^{2}s

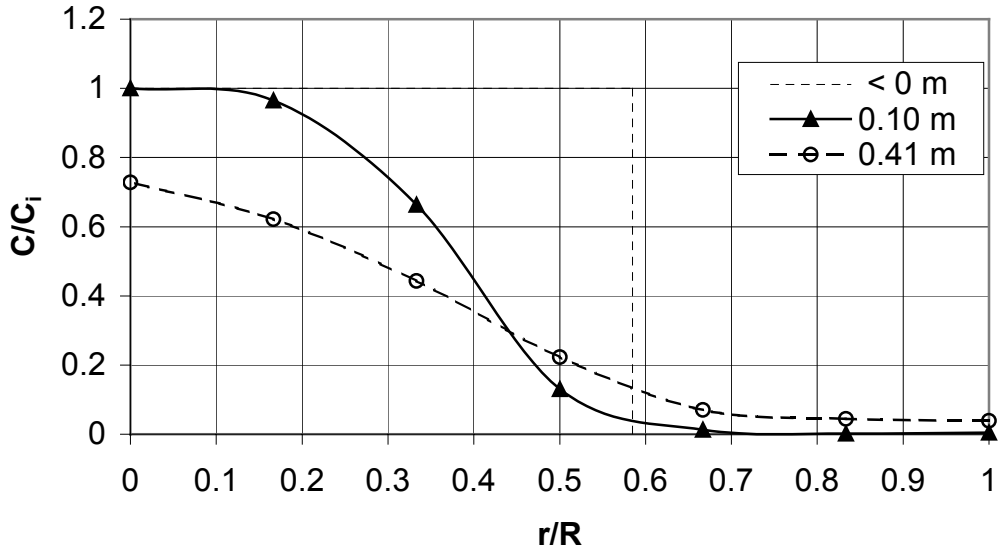

Figure 5.7.3 Helium Concentration Profile

Run 2. U_g = 5.2m/s, U_i = 9.5m/s, U_o = 3.2m/s, G_s = 145kg/m^{2}s

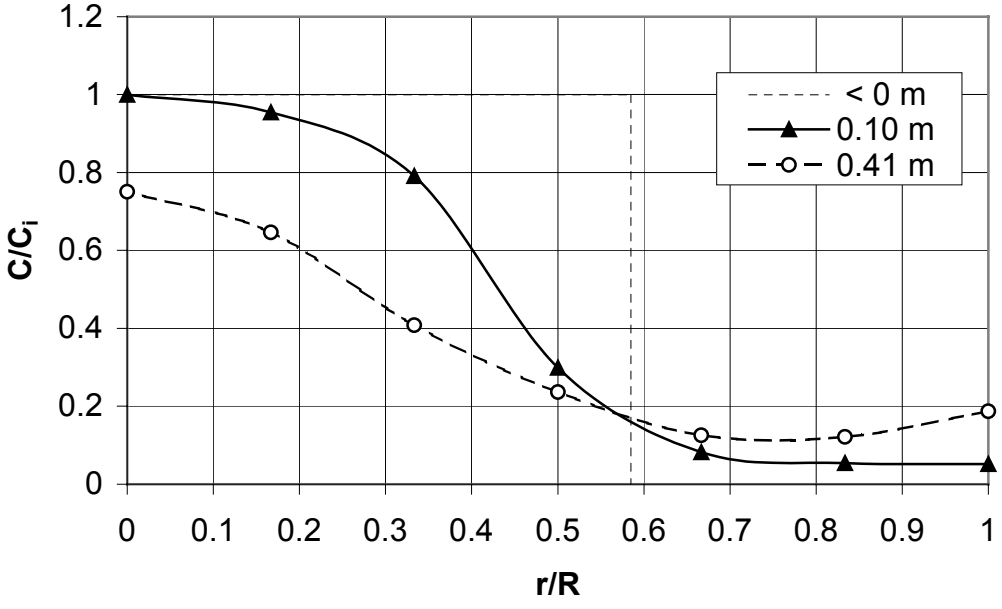

5.8 Radial Temperature Distribution

The radial distribution of the temperature with a heated inner stream is measured just above the separation and at one higher elevation to provide an indicator of the solid radial mass transport. The radial distribution of the temperature for λ=0.7, 1 and 3 are shown in Figures 5.8.1 and 5.8.3, respectively. The lateral transport of heat is mainly the result of lateral solid intermixing since the volumetric heat capacity of the particles is of the order of a thousandfold that of the gas.

Because the diameter of FCC particles are very small (~50μm), the solid and gas easily reach equilibrium in the inner tube before the merge. The mixed gas-solid temperature right above the merge provides an estimate of the relative solid flow rates in the inner tube since the temperature to which the air was heated in all the runs was the same. Comparing the λ=3 case with the λ=0.7 case, the inner tube velocity ratio is about 2.2, the riser circulation rate ratio is about 0.95 and the temperature rise ratio is about 2.4. Dividing 2.2 by 0.95 is about 2.4 which indicates that the flow rate of solid in the inner tube was about the same relative to the riser circulation rate for the two runs

even though the inner tube velocity was much greater in the λ=3 case. A comparison for the λ=1 case gives the same results.

Considerable solid mixing can be observed at h=0.1m for the λ=0.7 and the λ=1 cases although there is almost no gas intermixing detected at this elevation. This indicates that the solid intermixing between two streams starts earlier than gas intermixing, and solid mixing must be dominated by turbulent diffusion at this elevation. One important reason for this phenomenon is the readjustment of radial solid fraction profiles right after the merge, as observed in Figure 5.51 to Figure 5.5.8. The solids at both the inner and outer walls of the inner tube intermix and accelerate after the merge.

The location of the point, $T_{0.5}$, at which the temperature is half way between the peak value and the wall value can be used to estimate the rate of solid mixing. At 0.1m elevation, this point is about the same for the λ=0.7 and λ=3 cases and is closer to the wall than in the λ=1 case. This is due to the fact that the solid flow rate of the inner and the outer streams are about the same for all three cases, but the turbulent mixing of the solids is higher when the velocities of the two streams are different.

For the λ=0.7 case, in Figure 5.8.1, temperature decreases in the center core region but does not change much in the near wall region from 0.1m to 0.41m elevation. The location of the point, $T_{0.5}$, moved inward from 0.1m to 0.4m elevation. This indicates that solids are moving from the annular region into to the core region in this section. The radial inflow must dominate the turbulent diffusion of solids in this case. It is again consistent with the flow structure predicted in Figure 5.2.5.

In Figure 5.8.2, for the case of λ=1, temperature decreases in the core region and increases in the annular region from the 0.1m to the 0.41m elevation. In this case, the solid mixing is dominated by turbulent diffusion. The location of the point, $T_{0.5}$, is about the same at 0.1m and 0.4m elevations.

In Figure 5.8.3, the temperature as well as the diameter of the center core region decreases from the 0.1m to the 0.4m elevation, even though the inner stream velocity is much higher in this case. The location of the point, $T_{0.5}$, moved slightly inward from the 0.1m to the 0.4m elevation. The streamlines are actually bending inward slightly from 0.1m to 0.4m elevation due to the recirculation formed near the wall region at the 0.4m elevation. The effect of the recirculation pattern, however, cannot be observed as well as in the gas

mixing test Figure 5.7.3, where the helium concentration profile actually turns upward at the wall.

Figure 5.8.1 Temperature Distribution Above Merge

Run 1. U_g=5.2 m/s, U_i =4.3 m/s, U_o= 6.1 m/s, Gs=147 kg/m^{2}s

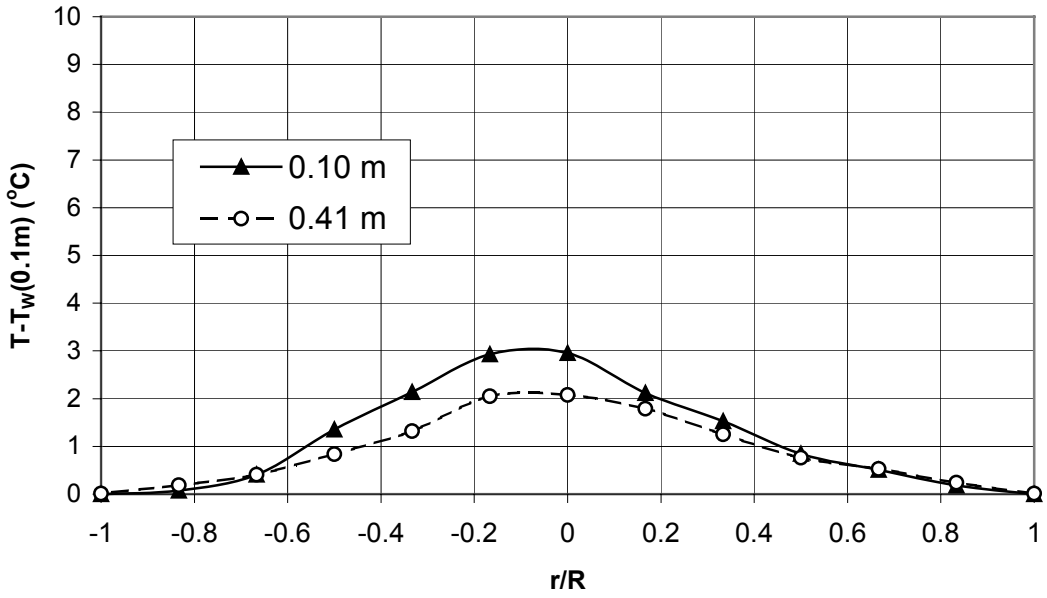

Figure 5.8.2 Temperature Distribution Above Merge

Run 2. U_g=5.2 m/s, U_i =5.4 m/s, U_o=5.4 m/s, Gs=147 kg/m^{2}s

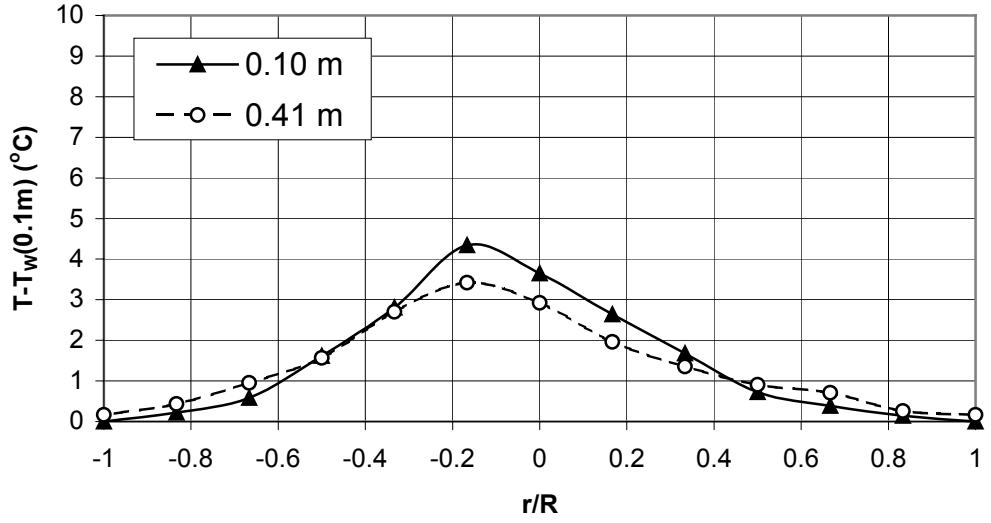

Figure 5.8.3 Temperature Distribution Above Merge

Run 3. U_g=5.2 m/s, U_i =9.5 m/s, U_o=3.2 m/s, Gs=142 kg/m^{2}s

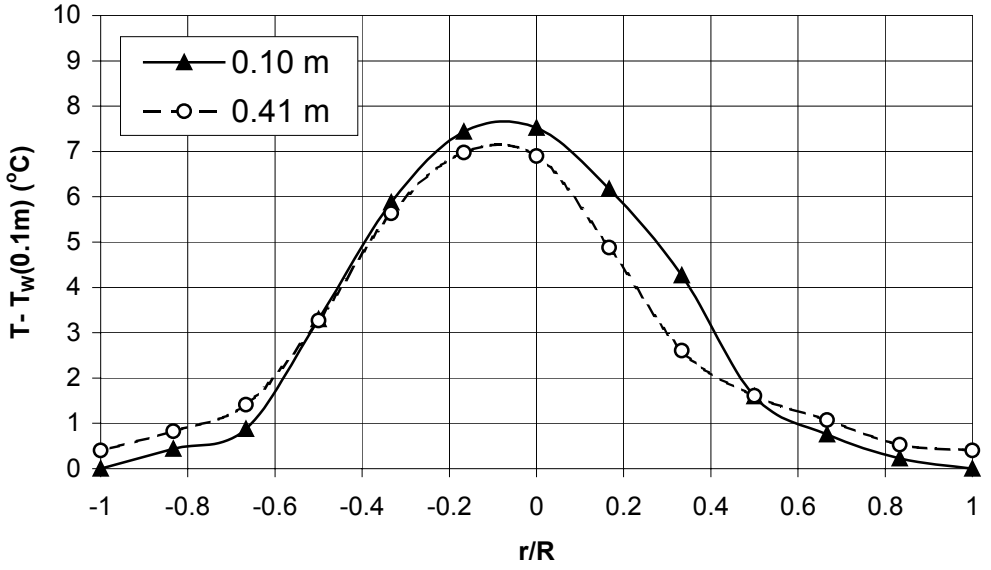

VI. CONCLUSIONS

In this investigation, three cases of the inner-to-outer velocity ratios of 0.7, 1 and 3 were studied using the modified City College fast fluidization unit. The experimental results show that two gas-solid streams from a single standpipe can be separated and treated independently before merging them into a single riser flow. Each of the separated streams can be controlled independently to some extent by the gas supplied to each stream. The flow rate of solid in the inner tube and in the annulus is, however, about the same relative to the riser circulation rate for all runs, independent of velocity ratio.

The solid distribution in the inner tube is a typical core-annulus distribution with high solid fraction at the wall and low solid faction in the center. The solid distribution across the annulus has high values at both the inner and outer walls. The solid holdups inside and outside the inner tube tend to be about the same due to the total effect of the pressure balance.

Experimental results show consistently that recirculation patterns similar to those of single-phase coaxial flows exist for very large and very small velocity ratio cases. The recirculation is above the mouth of the inner tube

when the inner-to-outer velocity ratio is 0.7 and is against the wall at higher elevation when the inner-to-outer velocity ratio is 3.

One-dimensional model is invalid representation in these cases because of the reciculation developed in the initial mixing region. In the mixing region above the merge, the cross-sectional average solid fraction decreases with cross-sectional average deceleration in the low velocity ratio case of λ=0.7, and the cross-sectional average solid fraction increases with cross-sectional average acceleration in the high velocity ratio case of λ=3.

NOMENCLATURE

A = cross section area, m^2

C = concentration of tracer, $kg \cdot m^{-3}$

Ct = the Craya-Curtet number

D = diameter of the raiser, m

G_s = solid circulation rate, $kg \cdot m^{-2} \cdot s^{-1}$

L = tap spacing, m

P = pressure, mbar

P_0 = pressure at the bottom of the U-tube, mbar

ΔP_L = pressure drop between two pressure taps, mbar

r = radius, m

R = bed radius, m

T = temperature, K

U_g = superficial gas velocity above the merge, $m \cdot s^{-1}$

U_i = superficial gas velocity of the outer stream, $m \cdot s^{-1}$

U_o = superficial gas velocity of the inner stream, $m \cdot s^{-1}$

U_s = solids velocity, $m \cdot s^{-1}$

U_1, U_2, U_3 = solid velocities in region 1,2 and 3 as defined in the simplified one-dimensional model, respectively, $m \cdot s^{-1}$

x = height relative to the merge, m

Greek symbols

α = solid fraction, 1-ε

λ = inner to outer stream gas superficial velocity ratio, U_i/U_o

ε = voidage

$\varepsilon_{apparent}$ = apparent voidage

ε_{true} = true voidage

$\overline{\overline{\varepsilon_{true}}}$ = the cross-sectional average true holdup averaged over L

ρ_s = solid density, $kg \cdot m^{-3}$

ξ = dimensionless section area ratio

$\overline{\Phi}$ = the cross-section average of any interesting hydrodynamic property, $\overline{\Phi} = \frac{1}{\pi R^2}\int_0^R \Phi(r) 2\pi r dr$

Subscripts

1, 2, 3 = represent the three regions defined in the simplified one-dimensional model, respectively.

1 for the riser flow without recirculation, 2 for the fast moving region and 3 for the recirculation region

0.5 = represents the value that is half way between the peak value and the wall value

down = represents the downflow

f = friction term

g = gas

up = represents the upflow

REFERENCES:

Bai D., Issangya A.S., and Grace J.R., Ind. Eng. Chem. Res. 38(1999) 803-811

Barchilon, M. and Curtet, R., "*Some Details of the Structure of an Axisymmetric Confined Jet with Backflow*", ASME Trans., Journal of Basic Engineering, Vol. 86, No.4, 1964, pp. 777-787

Becker, H.A., Hottel, H.C., and Williams, G.C., *"Mixing and Flow in Ducted Turbulent Streams*", Proceedings of the Symposium (International) on Combustion, The Combustion Institute, Pittsburgh, PA, 1962, pp. 7-20

Berkelmann, K.G. and Renz, U., Powder Technology, 68(1991), pp271-280

Brereton C.M. and Grace J.R., Chem. Eng. Sci. 48(1993) 2565

Cankurt, N.T. and Yerushalmi, J., in Davidson, J.F. and Keairns, D.L. (eds.), Fluidization, Cambridge University Press, London, 1978, pp.387

Choi, D.W., Gessner, F.B. and Oates, G.C., *"Measurements of Confined, Coaxial Jet Mixing With Pressure Gradient*", Journal of Fluids Engineering, Vol.108, March 1986, pp. 39-46

Craya, A. and Curtet, R., "*On the spreading of a confined jet*", (in French) Comptes-rendus Academie des Sciences, Paris, Vol.241, 1995, pp. 621-622

Feindt, H.J., "*Radial and axial density fluctuations in a high-velocity fluidized bed*", Ph.D. Dissertation, 1990, The City College of New York

Ghia, K.M. Torda, T.P., and Lavan, Z., "*Laminar Mixing of Heterogeneous Axisymmetric Coaxial Confined Jets*", AIAA Journal, Vol.7, No.11, Nov. 1969, pp. 2072-2078

Grace J.R., Cannadian Journal of Chemical Engineering, 64(1986) 353-363

Grace J.R., Issangya A.S., Bai D., Bi H.T., Zhu J., "*Situating the High-density Circulating Fluidized Bed*", AICHE Meeting, Miami, FL, Nov. 1998

Hedman, P.O. and Smoot, L.D., "*Particle-Gas Dispersion Effects in Confined Coaxial Jets*", AIChE Journal, Vol.21, No.2, March 1975, pp. 372-379

Helmrich, H. Schugerl, K. and Janssen, K., in P.Basu(eds.), Circulating Fluidized Beds Technology, Pergamon, Oxford, 1986, pp.161

Herb, B., Dou, S., Tuzla, K. and Chen, J.C., "*Solid mass fluxes in circulating fluidize beds*", Powder Technology, 70(1992), pp.197-205

Hill, P.G., "*Incompressible Jet Mixing in Converging-Diverging Axisymmetric Ducts*", ASME Journal of Basic Engineering, Vol.89, No.1, 1967, pp.210-220

Hinze, J.O. and Van der Hegge Zijnen, Applied Scientific Research, Series A, Vol.1, 1949, p 435

Johnson, B., "*Experimental study of multicomponent coaxial-flow jets in short chambers"*, NASA CR-1190, 1968

Kato K., Shibasaki H., Tamura K., Arita S., Wang C., Takarada T., J. Chem. Eng. Jp. 22(1989) 130-136

Khodadadi, J.M. and Vlachos, N.S., *"Experimental and Numerical Study of Confined Coaxial Turbulent Jets*", AIAA Journal, Vol.27, No.5, may 1989, pp. 532-541

Kostazos, A. "*An investigation of the entrance region of riser fluidized bed"*, Ph.D. Dissertation, 1997, The City College of New York

Kuethe, A., "*Investigation of the turbulent-mixing regions formed by jets",* Journal of Applied Mechanics, Vol.11, No.3, Transaction of the ASME, Vol.66, 1935, p A-87

Kwauk M., Li J., Powder Technology, 87 (1996) 193-202

Li Y., Kwauk M., J.R.G. Fluidization, J.M. Matsen (Eds.), "*The dynamics of fast fluidization*", Plenum, New York, 1980, 537-544

Mikhail, S., "*Mixing of Coaxial Streams inside a Closed Conduit*," Journal of Mechanical Engineering Science, Vol.2, No.1, 1960, pp.59-68

Monceaux, M.A., Molodtsof, Y. and Large, J.F. "*Overall and local characterization of flow regimes in a circulating fluidized bed*", in P.Basu(ed.), Circulating fluidized bed Technology, Pergamon, Oxford, 1986, p.185

Razinsky, E. and Brighton, J.A., "*Confined Jet Mixing for Nonseparating Conditions*", ASME Journal of Basic Engineering, Vol.93, No.2, 1971, pp.333-349

Razinsky, E. and Brighton, J.A., "*A theoretical Model for Nonseparated Mixing of a Confined Jet*", ASME Journal of Basic Engineering, Vol.94, No.3, 1972, pp.551-558

Rhodes M.J., Geldart D., Chem. Eng. Res., 67 (1989) 20-29

Rhodes M.J., Sollaart M., Wang X.S., Powder Technology, 99(1998) 194-200

Rozenman, T. and Weinstein, H., "*Recirculation patterns in the initial region of coaxial jets*", Journal of Applied Mechanics, Transaction of the ASME, December, 1972, pp891-896

Schnitzlein, Michael G. and Weinstein, H., "*Flow characterization in high-velocity fluidized beds using pressure fluctuations*", Chem. Eng. Sci., 43(1988), pp.2605-2614

Shavit, G. and Lavan Z., "*Analytical and Experimental Investigations of Laminar Mixing of Confined Heterogeneous Jets*", AIAA Journal, Vol.11, No.3, March 1973, pp. 352-358

Smolders K., Baeyens J., Powder Technology, 119 (2001) 269-291

Svensson A., Johnsson F. and Leckner B., Int. J. Multiphase flow, 22(1996) 1187

Weinstein, H. and Todd, C.A., "*A Numerical Solution of the Problem of Mixing of Laminar Coaxial Streams of Greatly Different Densities-Isothermal Case*", TND-1534, Feb. 1963, NASA

Weinstein, H., Shao, M., and Wasserzug, L, "*Radial solid density variations in a fast fluidized bed*", AIChE Symp. Ser. 80(241) (1984), pp117-121

Weinstein, H., Li, J., Bandlamudi, E. Feindt, H.J. and Graff, R.A., "*Gas backmixing of fluidized beds in different regimes and different regions*", Fluidization VI, Grace, J.R., Shemilt, L.W. and Bergougnou, M.A., Eds., Engineering Foundation, New York, 1989, pp.57-64

Wei Fei, Lu Fangbin, Jin Yong and Yu Zhiqing, "*Mass flux profiles in a high-density circulating fluidized bed*", Powder Technology, 91(1997) 189-195

Wei Fei, Wan Xiaotao, Hu Yongqi, Wang Zhiguo, Yang Yanhui, Jin Yong, Chemical Engineering Science, 56 (2001) 613-620

Yerushalmi J., Cankurt N.T., Powder Technology, 24(1979) 187-205

Zawacki, T.S. and Weinstein, H., "*Experimental investigation of mixing of dissmilar fluids*", NASA CR-957, 1968